Water Behavior on Olivine Surfaces

DISSERTATION

Presented in Partial Fulfillment of the Requirements for the Degree Doctor of Philosophy
in the Graduate School of The Ohio State University

By

Tingting Liu

Graduate Program in Geological Sciences

The Ohio State University

2017

Dissertation Committee:

Professor David R. Cole, Advisor

Professor Aravind R. Asthagiri

Professor David Tomasko

Professor Wendy Panero

Abstract

Water-rock interaction is one of the most active topics in geochemistry. Olivine group as one of the most important rock-forming minerals extensively occur in the Earth's crust and the upper mantle. The stability and reactivity of olivine minerals in ambient C-H-O fluids has drawn great attention. All the complex surface and bulk reactions occurring between the mineral and surrounding fluids starts with the water on the surface. But how water molecules interact with olivine minerals on the surface on an atomistic/molecular level is still less studied. This work examines the interaction between water and olivine mineral surface, in particular, from the energetics in static state to its structure and dynamics, and vibrational properties of the water molecules on the surface, thus providing a complete picture of molecular behavior of the surface water. This investigation use computational/simulation (first-principles calculations and classical molecular dynamics simulation) tools to calculate the energetics and the dynamic properties. Neutron scattering experimental data are also used to support the dynamic and vibrational property calculations.

Water molecule adsorption energy calculations via density functional theory (DFT) calculation is fulfilled by introducing different cation dopants on the forsterite(010) surface as they naturally occur in the crystal structure of olivine minerals as trace elements. It shows that Mg-H_2O has the strongest adsorption energy, and the

alkaline earth (AE) and transition metal (TM) cations form different types of bonding with H_2O, i.e., electrostatic force dominated bonding and covalent bonding, respectively. However, there is no simple trend relating the cation dopant charge or ionic radii to the adsorption energy of water molecule. Instead, it is found that several factors, including surface lattice distortion, ionic size, lattice size (different olivine end members) can together determine the adsorption energy sequence with different metal cations.

The structure and dynamics of water molecules on hydroxylated forsterite(010) surface is investigated at 270 K using classical molecular dynamics (MD) simulation. The water structure on the hydroxylated surface is composed of a first weak layer that adsorbs within the trough made by hydroxyl ions and a continuous strong layer on top of the first layer. The dynamic properties pertaining to translation and rotation were investigated separately using intermediate scattering functions (ISF). The translational diffusive motions derived by simulations qualitatively match with the fast and slow motions observed in the experiment. The rotational motion of water molecules and motions of the flexible hydrogen atoms on the surface calculated by simulations is found to be out of the observational energy window of the instrument.

MD simulations and inelastic neutron scattering (INS) are used to study the vibrational behavior of water on forsterite surface. Both techniques derived a broad libration band feature by examining the first adsorbed water layer on the surface. MD simulations discover that Ow interacts with the surface Mg atom, and water molecules form an ordered Ih-like ice structure by the network of hydrogen bonding at 10 K. Simulated vibrational data at 150 K was used to compare with INS data at 10 K, avoiding

iii

the limitation of classical MD to account for quantum effects that might be significant at 10 K. Confining effect was observed by the simulations, as the molecules near to the surface exhibit smaller bending and stretching magnitude than the free molecule.

This works sets up the stage for further investigation on other key geochemical process and could aid in more for water-rock reaction mechanism understanding among C-O-H fluids.

To Feng Yu,

Dad and Mom

Acknowledgments

This work would not be possible without the help of many people. First of all, I would like to express my greatest gratitude to my academic advisor, Prof. David Cole, who opened a door for me and has been always inspiring me on this road. He is such a great professor who not only visions problems in a broad scientific context but also instills students with rich update-to-date information and endless patience. As a student, I began to understand his broadness and his far-reaching insights at the point of finishing this work. I appreciate that he tries his best to create an open environment for students to pick up their scientific pathways, and the way he encourages and cultivates me. He spends hours and hours with students to share all his experience and thoughts without any reservation, and he is so patient and delightful to see my step-by-step progress. He sets a role model for me to pursue on this road.

Second, it is so fortunate for me to have Prof. Aravind Asthagiri in Dept. of Chemical Engineering as my mentor in calculation field since 2012. I know I am in great debt to him. He treats me like his own student. From knowing nothing about DFT to who

I am today, he instills me with countless tutoring, and most importantly, how to probe science. He is such a model from whom I could almost learn everything how to be a good scientist. He fosters students with how to read and how to think critically. He is always so ready to help with our presentation communication and give all the useful tips, for which I can never forget his effort and precious input. He also impresses me with his passion for science and the strong will to solve problems, which always enlightens me like a star in there when I miss my road.

For the third, I must thank Dr. Siddharth Gautam for his long-term mentoring for the MD simulations and neutron scattering techniques. He is a great scientist with modest attitudes but admirable expertise. I am very grateful for all his effort and time spent with me. Starting from scratch for MD simulations, I could not go this far at all without his endless patience and guidance. The spirit I hold up for myself to finish two of the projects stems from his perseverance for science, which always motivates me.

My thanks also go to my committee members, Prof. David Tomasko in Dept. of Chemical Engineering and Prof. Wendy Panero in School of Earth Sciences. I much value the opportunity for allowing me to try out my pore-fluid interaction experiments in Prof. Tomasko's lab, and all the stimulating questions he has inspired me. Thank you Wendy for reading my thesis and raising up the inspiring questions. I also thank Prof. Ann Cook in School of Earth Sciences for serving as my committee member during my candidacy exam, while her insights and questions broadened my eyesight.

I will take this chance to thank the SEMCAL crew in School of Earth Sciences. Especially for Drs. Julie Sheets and Sue Welch, thank you for all the useful discussion

Vita

Publications

Gautam S., Liu T., Rother G., Jalarvo N., Mamontov E., Welch S., Sheets J., Droege M. and Cole D.R. (2015) Dynamics of Propane in Nanoporous Silica Aerogel: A Quasielastic Neutron Scattering Study. *The Journal of Physical Chemistry C* **119**, 18188-18195.

Gautam S., Liu T., Patankar S., Tomasko D. and Cole, D. (2016) Location dependent orientational structure and dynamics of ethane in ZSM5. *Chemical Physics Letters* **648**, 130-136.

Patankar S., Gautam S., Rother G., Podlesnyak A., Ehlers G., Liu T., Cole D.R. and Tomasko D.L. (2016) Role of Confinement on Adsorption and Dynamics of Ethane and

an Ethane-CO$_2$ Mixture in Mesoporous CPG Silica. *The Journal of Physical Chemistry C* **120**, 4843-4853.

Fields of Study

Major Field: Geological Sciences

Table of Contents

List of Tables

List of Figures

xvi

Chapter 1: Introduction

1.1 Background

As one of the most abundant mineral phases in the Earth's crust and upper mantle, olivine has received much attention with respect to its stability and reactivity with coexisting fluids, as observed in terrestrial weathering at the surface or near-surface and ocean crust environments where hydrothermal fluids flow through and react with Mg-Fe rich basalts and gabbros. The broader importance of olivine in recent years has been rising for two reasons. One involves utilization of basalt or peridotite as the reservoir for CO_2 sequestration through the formation of Mg-Fe carbonate minerals (Matter et al., 2007; Matter et al., 2009; Power et al., 2013), where

$$\text{olivine/serpentine} + CO_2 \rightarrow \text{magnesite} + \text{quartz} \pm H_2O \qquad \text{Eqn (1.1)}$$
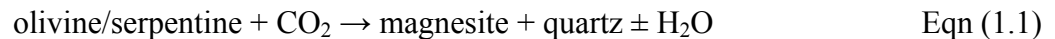
The well-known CarbFix pilot project was launched in an Icelandic geothermal system in 2007 involving direct injection of CO_2 into subsurface Fe-Mg rich rocks. Rapid formation of significant quantities of carbonate minerals in basaltic rocks have been observed by calculations and experiments (McGrail et al., 2006; Matter et al., 2007; Gysi and Stefánsson, 2008; Oelkers et al., 2008). The Columbia River Basalt Group lava flows in an interflow zone shows great potential for CO_2 sequestration due to its porosity and impermeability (McGrail et al., 2006). Another geologic storage potential is within the oceanic basalt formations (Goldberg et al., 2008).

The second aspect concerns abiotic hydrocarbon generation observed in the submarine environment due to carbon-bearing fluid interaction with ultramafic rocks via a Fischer-Tropsch type (FTT) catalytic process (McCollom and Seewald, 2001; Mccollom and Seewald, 2007; McCollom et al., 2010; McCollom and Seewald, 2013). The alteration of olivine is through a serpentinization process as follows (Proskurowski et al., 2008), where water is reduced to hydrogen at the presence of Fe(II).

$$6[(Mg_{1.5}Fe_{0.5})SiO_4] + 7H_2O \rightarrow 3[(Mg_3Si_2O_5(OH)_4] + Fe_3O_4 + H_2 \qquad \text{Eqn (1.2)}$$
olivine   serpentine   magnetite

$$2(Fe^{II}O)_{rock} + H_2O \rightarrow (Fe^{III}{}_2O_3)_{rock} + H_2 \qquad \text{Eqn (1.3)}$$
(McCollom and Seewald, 2013)
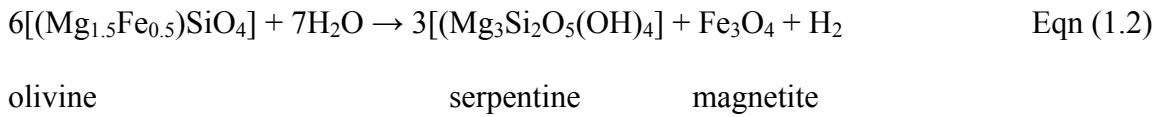
The FFT reaction is proceeded with the presence of H_2 through the following equation,

$$CO_2(aq) + [2 + (m/2n)]H_2 \rightarrow (1/n)C_nH_m + 2H_2O \qquad \text{Eqn (1.4)}$$
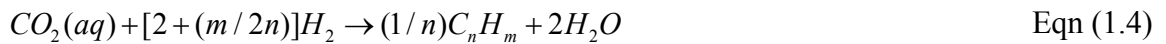
In addition to the catalytic role of Fe(II) in olivine minerals, experiments discovered that chromium component in ultramafic rocks (Foustoukos and Seyfried Jr., 2004) or Fe-Ni alloy in the ocean crust (Horita and Berndt, 1999) are also important catalysts for the formation of abiotic hydrocarbons. Minor phases of minerals and oxides in their submicron grain size in serpentinite are also potential catalysts for the FTT process, including S-poor sulfides, Ni-Fe alloy, Cr-spinel, and Fe-oxides (Dick and Gillete, 1976; Frost, 1985; Alt and Shanks III, 1998; Beard and Hopkinson, 2000; Klein and Bach, 2009).

Hydrocarbon sample collection at Lost City Hydrothermal Field located at 30°N on the Mid-Atlantic Ridge (MAR) indicate the carbon source is mantle-derived inorganic carbon leaching from host rocks (Proskurowski et al., 2008). The inorganic carbon occurs in many forms: inorganic carbon dissolved in mineral matrix, or graphite trapped in fluid inclusions, or in amorphous form that exists in grain boundaries (Proskurowski et al., 2008). The Rainbow hydrothermal field at 36°14'N (Holm and Charlou, 2001; Charlou et al., 2010), Logatchev I and II Active Vent Fields at 14°45'N (Charlou et al., 2010), Ashadza I and II Active Vent Fields at 12°58'N (Charlou et al., 2010) on the MAR are well studied areas that are enriched in abiotic hydrocarbon generation. A number of studies explored the CH_4 anomalies at the intersection of 12°~40°N and Mid-Atlantic Ridge (Charlou et al., 1988; Charlou et al., 1991; Charlou and Donval, 1993; Charlou et al., 1996; Charlou et al., 1998; Charlou et al., 2010) and revealed that serpentinization is ongoing along the whole Mid-Atlantic Ridge.

The interaction between water and olivine also has implications for the origin of water in solar system. It has been suggested that the source of planet water was delivered onto the rocky planets during planetary accretion favorably in simulation studies (Stimpfl et al., 2006; King et al., 2010) using forsterite to represent the primitive dust grains. A fundamental question applicable to these processes is the behavior of water on the mineral surface. This thesis covers the interfacial behavior of water on olivine surfaces, including its stability, structure, dynamic and vibrational properties, from static to the dynamic picture, thus providing a detailed understanding of the how water molecules have an interplay with olivine surfaces.

1.2 Methods

Simulation tools in this thesis include first-principles calculations and classical molecular dynamics (MD) simulations. Among first-principles calculations, density functional theory (DFT) method is employed. Calculations are within the frameworks of Vienna Ab initio simulation package (VASP) (Kresse and Hafner, 1993; Kresse and Hafner, 1994a; Kresse and Hafner, 1994b; Kresse and Furthmüller, 1996) and DL_POLY software package (Todorov et al., 2006), respectively. Neutron scattering experiment data were used to support the MD simulation results. The structure and dynamics of water on forsterite(010) surface at 270 K is complemented by quasi-elastic neutron scattering (QENS) data, while the vibrational property at low temperatures was investigated by both MD simulations and inelastic neutron scattering (INS), which is essentially a spectroscopic tool.

1.3 Results

Density functional theory (DFT) calculations that incorporate dispersion through the D3 formulation of Grimme and co-workers (Grimme et al., 2010; Grimme, Ehrlich, et al., 2011; Grimme, 2011) were performed to enhance our understanding of how olivine interacts with water on an atomistic level. Molecular water adsorption on doped forsterite(010) surfaces as well as on several end member olivine(010) surfaces at a low coverage was examined. Low coverage could allow us to exclude the effects from molecule-molecule interactions and identify the specific bonding formations between the molecule and the surface. Dopants included the alkaline earth metals (AE: Ca, Sr, and Ba) and transition metals (TM: Cr, Mn, Fe, Co, and Ni) that can occur as trace and minor elements in olivine minerals. While in general the AE dopants show stronger water

adsorption versus the TM dopants, a simple correlation to dopant charge or other dopant properties could not be identified. Instead through a detailed analysis of the molecular orbital picture, it is found that water adsorption strength on olivine(010) surface is a function of several, often competing, interactions between the surface and water.

MD simulations coupled with neutron scattering techniques unravel the intramolecular and intermolecular motions of water molecules on olivine surfaces. In the two simulations, total number of water molecules remained the same. However, due to the temperature effect (270 K vs 10 K), the states of water molecules at their equilibrium are different. The forsterite(010) surface was decorated with OH and H groups to mimic the mineral surface in ambient conditions, i.e., hydroxylated surface. MD simulations provide detailed structure information that cannot be detected by experiments. The translational diffusive motions derived by simulations qualitatively match with the fast and slow motions observed in the experiment. The rotational motion of water molecules and motions of the flexible hydrogen atoms on the surface calculated by simulations is are out of the observational energy window of the instrument. For the vibrational property, the one monolayer surface water show Ih-ice like structure at 10 K, which can be compared with the partial hydration/hydroxylation layer in INS experiment. Both techniques derived a broad libration band feature by examining the first adsorbed water layer on the surface. MD simulations improved the understanding of the interface structure on a molecular level, i.e., Ow interacts with the surface Mg atom, and water molecules form an ordered Ih-like ice structure by the network of hydrogen bonding at 10 K. MD simulations also identify the layering feature within the water layer and the preferred orientations of the molecules. In addition, the vibrational properties at 150 K by

simulation were compared with INS experiment to avoid the classical MD method limitation at 10 K. Confining effect can be observed by the simulations. It shows the molecules near to the surface exhibit smaller bending and stretching magnitudes than the free molecules.

1.4 Implications

The water behavior investigated in this study, including its energetics upon adsorption and its structure and dynamic properties provide the foundation for exploring other key geochemical behavior such as dissolution, mineral transformation (as in serpentinization) and catalytic reactions among C-O-H fluids. Future work will focus on the dissociative behavior of water molecules on olivine surfaces, and how the interface will evolve in aqueous environment that contains C-O-H fluids.

Chapter 2: Water Adsorption on Olivine (010) Surfaces: Effect of Alkali and Transition

Metal Cation Doping

2.1 Introduction

Olivine, $(Mg,Fe)_2SiO_4$, is one of the most prevalent silicate minerals in the solar system. It composes a major portion of the upper mantle of the Earth and is found on the Moon (Lucey, 2004; Isaacson et al., 2011), Mars (Hoefen et al., 2003; Hamilton and Christensen, 2005; Mustard et al., 2005; McSween et al., 2006; Morris et al., 2006; Koeppen and Hamilton, 2008), asteroids (e.g. Vesta) (Moroz et al., 2000; Krot et al., 2004; Sunshine et al., 2007), and a variety of other extraterrestrial bodies such as meteorites, comets, and interplanetary dust particles (IDPs) (Mason, 1967; Brownlee et al., 1976; Koeberl et al., 1989; Szurgot et al., 2008). There is a complete solid solution series between the olivine end-members forsterite (Mg_2SiO_4) and fayalite (Fe_2SiO_4), with nearly all naturally occurring olivine containing variable amounts of both iron and magnesium. Most terrestrial mantle-derived olivine has a Mg-rich (~$Mg_{1.8}Fe_{0.2}SiO_4$) composition due, in part, to the relatively higher oxygen fugacity (fO_2) in Earth's upper mantle as compared to crystallization environments on the Moon and Mars. In many natural crystals, and particularly the iron-rich olivines, there can be replacement of Mg and Fe(II) by Mn and Ca on the order of a few ppm to 100's ppm (Deer et al., 1982). Conversely, Ni and Cr are more prevalent in small quantities in the Mg-rich olivine. Trace element associations and concentrations are being used to distinguish types of

olivine such as mantle-derived (lower in Ca, Ti and Cr) versus volcanic olivine derived from recycled oceanic crust (greater amounts of Mn, Al, Sc, Co and Ni) (Foley et al., 2013).

The minerals of the olivine series are very susceptible to weathering, hydrothermal alteration and low-grade metamorphism. The reactions are generally complex and may involve hydration, silication, oxidation and carbonation. For example, weathering of exhumed peridotites or peridotites exposed in mine waste leads to carbonate formation – two similar pathways of carbonate mineralization potentially important to the sequestration of atmospheric CO_2 (Power et al., 2013). Direct injection of CO_2 into subsurface Fe-Mg rich rocks such as basalts in an Icelandic geothermal system has led to the rapid formation of significant quantities of carbonate minerals (Matter et al., 2009). Water, especially its concentration on mineral surfaces, plays a key role in the bulk reaction of olivine to carbonate minerals, as illustrated in work by Loring and co-workers (Loring et al., 2011).

Another important geochemical process involving olivine minerals is their potential to catalyze the formation of abiotic hydrocarbons in the deep Earth, through a Fischer-Tropsch Type (FTT) reaction. Serpentinization of transition metal-bearing olivine under hydrothermal conditions is observed to lower the oxidation state leading to the conversion of oxidized forms of carbon such as CO_2 or dissolved carbonate to reduced carbon compounds (McCollom and Seewald, 2007; McCollom et al., 2010; McCollom, 2013; McCollom and Seewald, 2013). Water in such catalyzed reactions is the source of hydrogen and likely also a key facilitator in the reaction; thus,

understanding the structure and reactivity of water on olivine surfaces is crucial for subsequent studies on carbon-involving surface and bulk reactions.

Several modeling studies have addressed the energetics of water adsorption on forsterite surfaces (de Leeuw et al., 2000; de Leeuw, 2001; Stimpfl et al., 2006; King et al., 2010; Kerisit et al., 2012; Asaduzzaman et al., 2013; Prigiobbe et al., 2013; Kerisit et al., 2013). Kerisit et al. (2012) examined the structure of the interface between forsterite(010) surface and supercritical (sc) CO_2/H_2O using molecular dynamics (MD) simulation to provide information for olivine carbonation during CO_2 sequestration. They found that $scCO_2$ does not interact with the surface directly when the surface is saturated with adsorbed water, thus the $H_xCO_3^{(2-x)-}$ (form depending on whether bare or hydroxylated surface) formation is within the water film. In the case of a water layer below two monolayers or a hydroxylated mineral surface, $scCO_2$ can penetrate onto the forsterite surface resulting in formation of $H_xCO_3^{(2-x)-}$ in direct contact with the surface. King et al. (2010) also conducted a simulation study of water adsorption on forsterite(100) surface using interatomic potential-based simulation methods to test the hypothesis that water was delivered to the rocky planets via interfacial processes during planetary accretion. They observed that dissociated water is stabilized on (100) but not on the perfect (010) surface. However, the introduction of defects on the (010) surface, such as steps and corners, dissociates water due to the presence of low-coordinated Mg. These results provide evidence that water could be retained and accumulate on the dust grains during accretion.

Quantum mechanical methods, in particular density functional theory (DFT), have been a useful tool to study the adsorption behavior of water on oxide surfaces since these methods provide more accurate energetics and can be used to study water adsorption more readily than interatomic potentials. The earliest work of water adsorption on the forsterite(010) surface using DFT by de Leeuw revealed that molecular water is favored over dissociated water, with dissociated water configurations recombining to molecular water (de Leeuw, 2001). However, more recently Asaduzzaman et al. (2013) found dissociated water was favored over molecular water on the forsterite(010) surface. In analyzing this study we discovered that they reversed the (010) and (100) surfaces in their figures and subsequent discussion. Furthermore, they used a dipolar termination of the (010) surface, which is less stable and correspondingly would interact more strongly with water. Prigiobbe et al. (2013) used DFT calculations and observed that water adsorption on the forsterite(100) surface occurs with co-adsorbed molecular and dissociated water forming a hydrogen bonding network at their higher water coverage. Their lower water coverage generated the highest adsorption energy with only dissociated H_2O on the (100) surface. Kerisit et al. (2013) used DFT with dispersion corrections to examine adsorption of water up to two monolayers on the (010) surfaces of five end members of olivine minerals ($[X]_2SiO_4$ where X = Mg, Ca, Mn, Fe, and Co). They found good agreement with the adsorption energy of water versus coverage in comparison to the experimental calorimetric measurements on powdered forsterite (Chen and Navrotsky, 2009). The alkaline-earth (AE) olivines lead to higher water adsorption energy than the transition-metal (TM) olivines, and the adsorption energy decreases with increasing water coverage independent of the end member species. They also examined the energetics of water

versus CO_2 on the surfaces, and found CO_2 can be replaced by water on all of the olivine surfaces. This result is consistent with their earlier MD study where water is preferentially adsorbed at the mineral surface over CO_2 (Kerisit et al., 2012). Finally, they attribute the increased water binding energy on AE olivines to the more ionic nature of the alkaline cations.

Water adsorption studies on end-member olivines discussed above provide an understanding of water on the geologically relevant forsterite and fayalite surfaces. However, common natural alkaline earth and transition elements, such as Ca, Sr, Ni, Co, Mn, are commonly observed in olivine crystal structures at a low concentration (~ hundreds of ppm) (Tafto and Spence, 1982; Hervig et al., 1986) and these dopants may affect the structure and reactivity of water on the olivine surfaces. As a first step to quantifying the effect of cation dopants, we have used DFT with dispersion to examine the adsorption of H_2O on the pure forsterite(010) surface, surfaces doped with Ca, Sr, Ba (AE) and those with Cr, Mn, Fe, Co, and Ni (TM). In addition, several representative end member olivine phases (Ca, Sr, Mn, Fe, and Co) have also been studied to better understand the difference between an isolated cation dopant versus the corresponding end member. The surface energies of various low-Miller index facets of forsterite have been calculated by previous studies (de Leeuw et al., 2000; Stimpfl et al., 2006), with both studies concluding that the non-dipolar (010) is the most stable surface, corresponding to its main mineralogical cleavage plane. Therefore, we have used (010) as a representative surface to explore the effect of AE and TM cation doping in olivine minerals on water adsorption. The dopants modify the interaction of H_2O on the olivine surface with

forsterite and Ca-doped forsterite exhibiting stronger adsorption energies than the TM dopants. For both type of dopants we have used analysis of the electronic density of states to understand the electronic structure for H_2O adsorption. Analysis of the electronic structure indicates the AE (TM) dopants show more ionic (covalent) bonding with H_2O for the cation-oxygen bond, but hydrogen bonding with adjacent surface oxygen atoms and the surface distortion upon H_2O adsorption also play a significant role in determining the strength of the overall H_2O-surface interaction.

2.2 Computational details

All the calculations in this study were performed using the Vienna *ab initio* simulation package (VASP) (Kresse and Hafner, 1993; Kresse and Hafner, 1994a; Kresse and Hafner, 1994b; Kresse and Furthmüller, 1996). Dispersion is incorporated through the empirical DFT-D3 model of Grimme and co-workers (Grimme et al., 2010; Grimme, Ehrlich, et al., 2011; Grimme, 2011). The DFT-D3 approach has negligible additional computational cost to the DFT calculations since the empirical dispersion term is added to the DFT energy and forces, but the approach has been shown to be relatively accurate for several systems (Bučko et al., 2010; Grimme, Huenerbein, et al., 2011; Lee et al., 2011; Grimme et al., 2012; Reckien et al., 2012; Hujo and Grimme, 2012), including water adsorption on olivine surfaces (Kerisit et al., 2013). Projector augmented wave (PAW) (Blöchl, 1994; Kresse and Joubert, 1999) pseudopotentials provided in the VASP database were used with the following states treated as valence states: Mg (2p, 3s), Ca (3s, 3p, 4s), Sr (4s, 4p, 5s), Ba (5s, 5p, 6s), Cr (3p, 3d, 4s), Mn (3p, 3d, 4s), Fe (3p, 3d, 4s), Co (3p, 3d, 4s), Ni (3p, 3d, 4s), Si (3s, 3p), and O (2s, 2p). Calculations were

performed with a plane wave cut-off energy of 800 (400) eV for bulk (surface) structure calculations using the Perdew-Burke-Ernzerhof (PBE) exchange correlation functional (Perdew et al., 1996). Self-consistent total-energy iterations were accelerated by Fermi-level smearing with a Gaussian width of 0.1 eV. Atom positions are relaxed using the limited memory Broyden-Fletcher-Goldfarb-Shanno (LBFGS) method (Sheppard et al., 2008) until the forces on all unconstrained atoms are less than 0.001 (0.03) eV/Å for bulk (surface) calculations. A $4 \times 2 \times 4$ Monkhorst-Pack mesh (Monkhorst and Pack, 1976) was used to sample the Brillouin zone for all bulk calculations. Spin polarization was included for any calculation with transition metals. In addition, several studies have shown that the band gaps of TM oxides are not captured by standard DFT (Rohrbach et al., 2004; Costa et al., 2009). We have applied the GGA+U method following the Liechtenstein approach (Liechtenstein et al., 1995) for the TM-containing olivine species with a U value of 5.0 eV applied to the d states of the TM dopants and $J = 1$ eV as a constant exchange parameter. The choice of U is based on studies on Cr_2O_3 (Rohrbach et al., 2004; Costa et al., 2009) and Fe_2O_3 (Rohrbach et al., 2004).

2.2.1 Bulk structure

Bulk olivine minerals belong to the *Pbnm* space group (shown in Fig. A1 of Appendix A), which can be described by three lattice parameters associated with the *a*, *b*, and *c* orthogonal lattice vectors. The magnetic properties of the transition metals in the three end members (Fe, Co, and Mn) followed what has been described in Kerisit et al. (2013), i.e., antiferromagnetic structure. Sr-olivine is in a monoclinic *β* phase at ambient condition (Catti, Gazzoni and Ivaldi, 1983), but transforms to an α' phase with *Pmnb*

space group at 358 K (Catti, Gazzoni, Ivaldi, et al., 1983). However, for the purpose of comparing Sr-doped forsterite to Sr-olivine we examined a *Pbnm* Sr-olivine structure.

Table 2.1 reports the experimental lattice constants, the recent PBE-D2 results by Kerisit et al. (2013), and our calculated PBE-D3 values for various bulk end-member olivine materials. The PBE-D3 lattice parameter values identified in this study are used to fix the lateral dimension in subsequent surface calculations. The $U = 0$ results comparable to Kerisit et al. (2013) are provided in the Table A1 in Appendix A.

Table 2.1. Calculated lattice constants of the six end member olivine structures in this study. The results from our PBE-D3 calculations are in bold and volume difference is relative to the experimental values.

	Experiment			Calculated, PBE-D3, $U=5$, $J=1$				Kerisit et al.*, Calculated, PBE-D2, $U=0$		
	a (Å)	b (Å)	c (Å)	a (Å)	b (Å)	c (Å)	Vol. diff(%)	a (Å)	b (Å)	c (Å)
Mg_2SiO_4	4.753	10.199	5.981†	**4.771**	**10.197**	**5.990**	0.50	4.756	10.096	5.938
Ca_2SiO_4	5.081	11.224	6.778‡	**5.093**	**11.208**	**6.756**	-0.24	5.173	11.425	6.881
Sr_2SiO_4				**5.274**	**11.799**	**7.247**				
Mn_2SiO_4	4.902	10.596	6.257‖	**4.922**	**10.631**	**6.286**	1.20	4.947	10.632	6.360
Fe_2SiO_4	4.818	10.471	6.086¤	**4.848**	**10.515**	**6.110**	1.45	4.745	10.489	6.151
Co_2SiO_4	4.780	10.298	5.999§	**4.827**	**10.296**	**6.008**	1.14	4.843	10.321	6.041

* (Kerisit et al., 2013), † (Lager et al., 1981), ‡ (Udagawa et al., 1980), ‖ (Fujino et al., 1981), ¤ (Smyth, 1975), § (Tamada, O., Fujino, K., Sasaki, 1983)

The results from the PBE-D3 method are in good agreement with the experiment data, as the volume difference compared with experimental values are relatively small. The differences between this study and Kerisit et al. (2013) on lattice constants, in particular, for Ca-olivine and fayalite, could be attributed mainly to differences in the pseudopotentials (our calculations include more valence electrons) and the use of D3 instead of D2 for dispersion effects.

2.2.2 Surface model

For the olivine(010) surface, the primitive surface lattice vectors correspond to the bulk *a* and *c* vectors, respectively. As noted above, the (010) surfaces are created from the relaxed bulk PBE-D3 structures. There are two possible terminations of the olivine(010) surface referred to as dipolar and non-dipolar (Noguera, 2000; de Leeuw et al., 2000), as shown in Fig. A2 of Appendix A. We selected the non-dipolar termination for our study, which is a reasonable choice as it retains the Si-O tetrahedron. Furthermore, de Leeuw et al. (2000) have studied both terminations of forsterite(010) using interatomic potentials and concluded that the non-dipolar (010) is more stable than the dipolar (010) surface, unless the dipolar termination is hydroxylated.

We selected a 2×2 surface unit cell shown in Fig. 2.1a for all of our calculations along with a corresponding $2 \times 2 \times 1$ Monkhorst-Pack mesh (Monkhorst and Pack, 1976) to sample the Brillouin zone. A dipole correction (Bengtsson, 1999) was included for all surface calculations. A vacuum space of 18 Å was used throughout all the surface calculations, which we have confirmed is sufficient to eliminate spurious periodic interactions in the direction normal to the surface. The surface normal direction corresponds to the bulk *b* axis and a unit thickness of the slab was set equal to the *b* lattice parameter. The appropriate slab thickness was examined by evaluating the surface energy using one and two unit cell thicknesses, with the upper half relaxed and lower half fixed for both slabs. As shown in Table A2 of the Appendix A, the surface energies differ by less than 0.01 eV/Å^2 for two slab thicknesses thus one unit cell slab thickness was used for all calculations and a side view of this slab is shown in Fig. 2.1b.

To study the effect of doping, we replaced one Mg atom out of four on the first layer of the 2 × 2 forsterite(010) surface with the dopant. While this approach does not include many possible scenarios such as subsurface dopants or clustering of dopants, it captures the local surface interaction between a dopant and adsorbed H_2O in a computationally tractable manner. We have examined larger unit cells (2 × 3) to interrogate the size effect (see Sec. AII in Appendix A) but found negligible changes to water behavior near a dopant atom due to system size.

In this work the adsorption energy, E_{ads}, is defined by

$$E_{ads} = (E_{sys} - E_{slab} - nE_{H_2O(g)})/n, \qquad \text{Eqn (2.1)}$$

where E_{sys} is the total energy of the system with adsorbed species, E_{slab} is the energy of bare surface, $E_{H_2O(g)}$ is the energy of an isolated water molecule, and n is the number of water molecules adsorbed within the unit. In the earlier studies of water molecules on oxide surfaces, one monolayer (ML) of water has been generally defined to be equivalent to one water molecule for every surface cation. However, for the olivine(010) surface, Kerisit et al. (2013) define such a scenario as 0.5 ML since one cation could accommodate two water molecules on almost the same monolayer level; thus we followed their definition throughout the work. Our focus in this work is the low H_2O coverage scenario, i.e., on a 2 × 2 surface unit cell where there are four surface cations in total, one single water molecule is equivalent to a coverage of 0.125 ML.
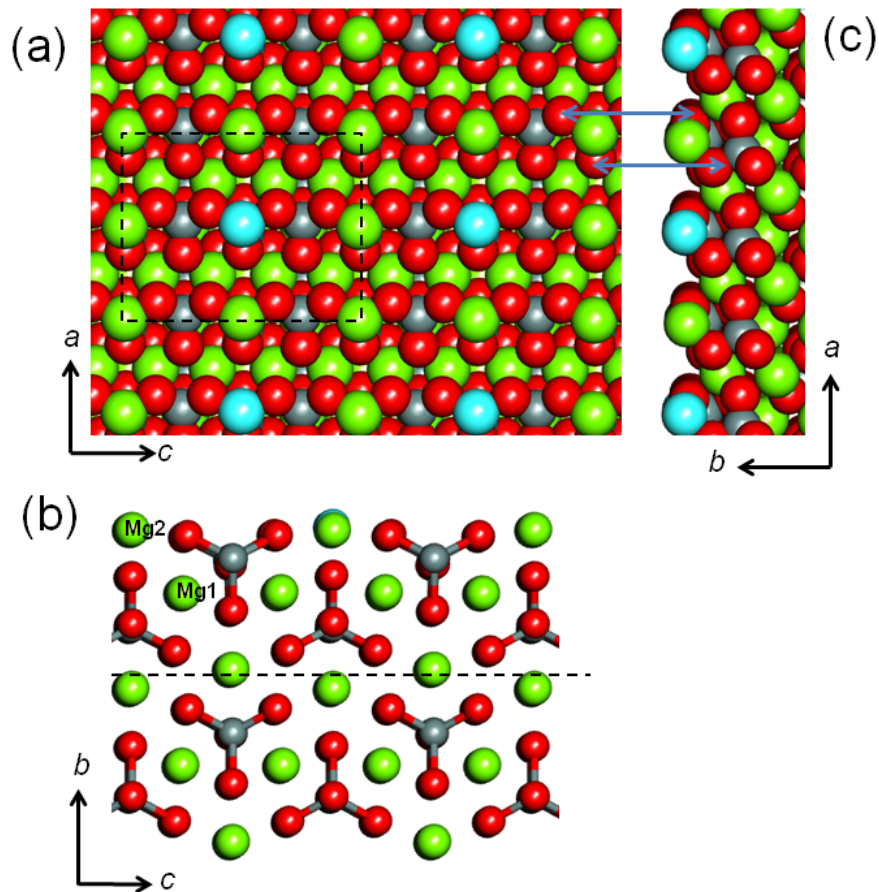
Fig. 2.1. Top (a) and side views (b, c) of doped forsterite(010) surface. Area in dashed box of the top view indicates the size of a 2 × 2 surface unit cell. Side view of a one-unit slab model with a thickness equal to the *b* axis lattice parameter of bulk forsterite. Two positions of Mg atom are labeled in the side view. Blue arrows between (a) and (c) connect the corresponding surface O atoms which are at lower positions than the surface cations. The atoms are free (fixed) in the relaxation above (below) the dashed line in (b). Mg=green spheres, Si=grey spheres, O=red spheres, dopant=light blue spheres.

2.3 Results and discussion

2.3.1 Energetics and structure of adsorbed H₂O

A systematic exploration of possible adsorption sites and configuration for water on forsterite(010) surface was performed and the two stable local minima of molecular water found are shown in Fig. 2.2. The two molecular water adsorption configurations

will be referred to as pointing-down (Fig. 2.2a, b) and flat-lying (Fig. 2.2c, d) in this study. Both configurations have a primary metal-oxygen bonding interaction (referred to as Me-Ow henceforth) combined with additional hydrogen bonding between water and the O atom from the adjoining $[SiO_4]^{4-}$ tetrahedron (referred to as Ox-Hw henceforth). For the pointing-down configuration there is only one such hydrogen bond while the other H atom is nearly normal to the surface and points upward. Kerisit et al. (2013) also reported similar molecular water configurations but at 0.5 ML coverage, i.e., every surface cation is associated with one adsorbed water molecule.
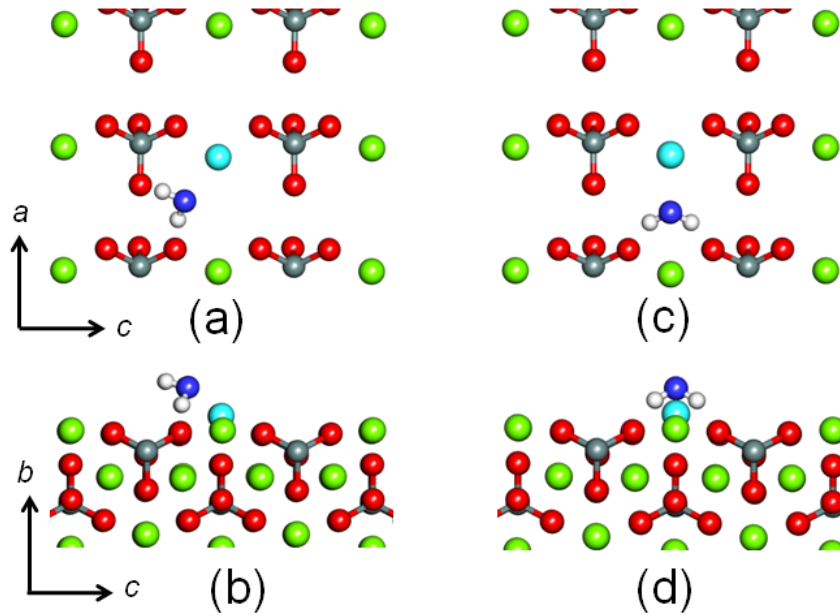
Fig. 2.2. Two local minima of one molecular water on a 2 × 2 supercell of doped forsterite(010) surface (0.125 ML). (a) and (c) are the top views, while (b) and (d) are the side views. Molecular water tilts on the surface in (a) and (b), with Hw interacting with Ox and Ow interacting with the metal atom. (c) and (d) show a flat-lying configuration with two Hw interacting with Ox. Ow=blue, Hw=white. The cation interacting with the H_2O molecule is light blue to distinguish from the other cations (green).

We further examined molecular water adsorption on both doped forsterite(010) surfaces and several olivine end member (010) surfaces. For all these surfaces, the two

favored configurations of H_2O found on the pure forsterite(010) surface were used as an initial guess. Table 2.2 summarizes the water molecule adsorption energies (E_{ads}) for all the olivine surfaces examined in this study. Structural data of the adsorbed H_2O configuration on each surface is presented in Table A4 of Appendix A. Molecular water shows similar local minima on each surface except for the pointing-down configuration on Sr-olivine(010) surface, where the water dissociates upon relaxation. From Table 2.2, it can be seen that the pointing-down configuration is more favorable than the flat-lying for majority of the surfaces. The exceptions are Mn-doped and pure forsterite(010) surfaces, but in both cases the difference is not substantial (less than 4 kJ/mol). Interaction between the Mg atom and molecular water yielded the strongest adsorption (the more negative, the stronger adsorption as defined), while water shows the weakest adsorption on the Ba-doped forsterite surface.

Table 2.2. Adsorption energy of molecular water on all olivine(010) surfaces in this study. Data in parenthesis are from Kerisit et al. (2013)*.

Surface	E_{ads} (kJ/mol)		Bader charge (e)	Surface	E_{ads} (kJ/mol)		Bader charge (e)
Doped forsterite	Pointing-down	Flat-lying	Central Me	End member	Pointing-down	Flat-lying	Central Me
Pure	-138.1	-142.3	+1.71	Mg_2SiO_4	-138.1(-137.0)	-142.3 (-142.5)	+1.71
Ca-doped	-125.3	-120.4	+1.55	Ca_2SiO_4	-129.1 (-148.4)	-114.3 (-122.3)	+1.55
Sr-doped	-113.1	-103.0	+1.59	Sr_2SiO_4	N.A.	-100.5	+1.59
Ba-doped	-96.3	-81.6	+1.58				
Cr-doped	-111.5	-83.6	+1.36				
Mn-doped	-124.0	-125.5	+1.42	Mn_2SiO_4	-111.3 (-99.6)	-106.7 (-96.1)	+1.42
Fe-doped	-100.8	-100.5	+1.29	Fe_2SiO_4	-100.2 (-101.6)	-95.1 (-100.0)	+1.31
Co-doped	-121.0	-120.0	+1.24	Co_2SiO_4	-123.8 (-113.1)	-119.3 (-111.3)	+1.25
Ni-doped	-112.9	-91.3	+1.19				

*: Cited data was based on U=0 for all the elements, whereas data in this study used method in Liechtenstein et al. (1995) to implement U parameters for the TMs.

The E_{ads} data reported by Kerisit et al. (2013) on the various olivine(010) surfaces are reported in parenthesis in Table 2.2. While forsterite and fayalite show relatively

similar values for the adsorption energy, our results for Ca-olivine, Mn-olivine, and Co-olivine do show larger differences (~10-20 kJ/mol) from those reported by Kerisit et al. (2013). While there are differences in the H_2O coverage in these two calculations (0.5 ML in the earlies study versus 0.125 ML in the present study) we have confirmed this is not the source of the observed differences in adsorption energy. We attribute these differences to a combination of effects coming from (1) the different dispersion methods (D2 versus D3), (2) inclusion of more electrons as valence electrons in our DFT calculations, and (3) the inclusion of the $+U$ method for the TM metals. We included U parameters to correct the strong electron correlation effect for transition metals while Kerisit et al. (2013) did not include the U parameters. It is important to note that these differences in the calculation details lead to differences in the relaxed bulk lattice structure (Table 2.1), which can also affect the adsorption energy of H_2O since the relaxed bulk lattice structure is used to generate the surface structure. Overall the two studies show similar trends for H_2O adsorption but Kerisit et al. (2013) predict a much stronger binding of the pointing-down configuration on Ca-olivine(010) surface. It is worth noting that Ca-olivine bulk structure from our study is significantly smaller (5.17% smaller volume) than that reported by Kerisit et al. (2013), which might contribute to our observed less negative E_{ads} (i.e. weaker binding) on Ca-olivine(010) surface (Table 2.2).

Kerisit et al. (2013) suggested the water adsorption energy on the end member olivine surfaces could be correlated to the charge of the surface metal cation. In particular, they found that the AE-olivines (Mg, Ca) had a larger cation charge than the TM-olivines (Mn, Fe, Co) and this matched the observed more negative E_{ads} on the AE-

olivines; however, a clear linear trend was not established. They attributed the stronger water bonding with AE-olivine surfaces to the larger ionicity of these surfaces.

Fig. 2.3 plots the E_{ads} of the pointing-down H_2O molecule versus the Bader charge (Bader, 1990; Henkelman et al., 2006; Sanville et al., 2007; Tang et al., 2009) associated with the metal cation of the bare surface, which locally interacts with H_2O (shown in Table 2.2). Similar results are obtained if one uses the flat-lying configuration. From Fig. 2.3 it is clear that there is no simple linear trend between E_{ads} and metal cation charge. We have attempted another charge partitioning method, Density Derived Electrostatic and Chemical (DDEC) (Manz and Sholl, 2010; Manz and Sholl, 2012), and obtained similar results (see Fig. A4 in Appendix A). Focusing on the AE dopants, which based on the Bader charge would be expected to generate a more negative E_{ads}, we find that Ca-doped forsterite and Ba-doped forsterite have similar Bader charges but have a difference of nearly 29 kJ/mol in adsorption energy, with Ba-doped forsterite(010) showing the weakest H_2O binding of all the surfaces we have examined. Similarly, for the TM dopants there is no linear trend with respect to the Bader charge.
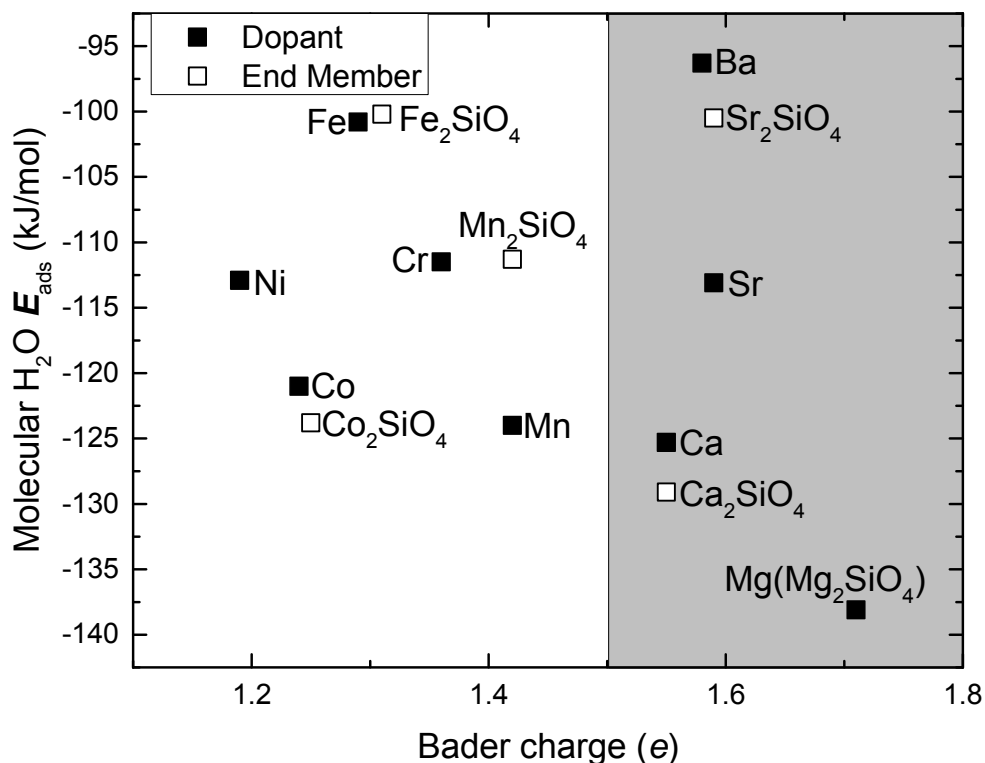
Fig. 2.3. Bader charge vs. molecular water E_{ads} on all olivine surfaces in this study. The H_2O configurations are all pointing-down on each surface, except for Sr_2SiO_4 where the configuration is flat-lying, and its pointing-down configuration does not stabilize but dissociates instead. The shaded area segregates AE and TM species.

2.3.2 Frontier orbital analysis

A better understanding of the variation in adsorption energy for water on these various olivine surfaces can be obtained by developing a frontier orbital analysis for adsorbed water. The adsorption energy will depend on both the metal cation-water (Me-Ow) bonding and hydrogen bonding through the adjacent surface oxygen atom (Ox-Hw). These two bonds, i.e. Me-Ow and Ox-Hw, depend on the interaction of the molecular orbitals (MOs) of H_2O with the surface states of the metal cation and surface oxygen atom, respectively. Water adsorption on a range of metal and metal oxide surfaces has

been reported in the literature (Henderson, 2002; Michaelides et al., 2003; Meng et al., 2004; Hodgson and Haq, 2009). The $1b_2$, $3a_1$, and $1b_1$ (HOMO) MOs of water are the highest energy occupied states of water and potentially participate in bonding on the surface. Michaelides et al. (2003) have characterized the bonding interactions of water on Pt(111), and other close-packed 4d metal surfaces within a frontier orbital framework (Carrasco et al., 2009). Our reproduced work for single water molecule on Pt(111) surface can be found in Sec. AIV of Appendix A. On the metal surfaces, a single water molecule (i.e. a water monomer) interacts only through the Me-Ow bond with no hydrogen bonding present due to the lack of any oxygen atoms. In the favored configuration the water molecule is in a nearly flat orientation parallel to the surface and the Ow atom is positioned directly on the top of the surface metal atom. Based on analysis of the density of states (DOS) and Mulliken charge analysis, Michaelides et al. (2003) find that the water molecule donates electrons primarily from the $1b_1$ lone pair HOMO orbital to d states of the metal. The $3a_1$ orbitals show some hybridization but it is weaker than the $1b_1$ orbital and also consists of some filled antibonding states, which weaken the water-metal surface interaction. The primary interaction through the $1b_1$ orbital favors the in plane H_2O orientation on the metal surface.

To our knowledge there have been less detailed DFT-based bonding analysis of water on oxide surfaces. Commonly the focus of water/oxide theoretical studies has been the resolution of the structure of water at the water-oxide interface (Allegretti et al., 2005; Hammer et al., 2010; Hinojosa et al., 2010; Riplinger and Carter, 2015; Szabova et al., 2015; Mu et al., 2017). Oxide surfaces have more complex bonding interactions since

even for a single water molecule hydrogen bonding through the surface O atoms will lead to a more complex frontier orbital picture with multiple centers of interaction. Furthermore, oxides can vary in electronic (ionic, covalent, degree of reducibility) and lattice structures (e.g. cation-surface oxygen distance) making it more difficult to develop a simple universal bonding picture. Henderson has analyzed several experimental valence photoemission and x-ray photoelectron spectroscopy (XPS) studies of water on both metal and metal oxides (Henderson, 2002). In metals the primary water orbitals affected are the $1b_1$ and $3a_1$ with the $1b_1$ lone pair orbital showing the most stabilization but this is not universal and the photoemission data can be difficult to interpret unambiguously. On metal oxides, the general picture that has been proposed is that the lone pair on Ow ($1b_1$ lone pair orbital) donates electrons to the cation of the metal oxide with some additional hydrogen bonding (Henderson, 2002). Water adsorption on MgO(001) and other AE rocksalt oxides have been proposed to occur through electrostatic interactions (Hu et al., 2011) but some degree of hybridization of surface states with the $1b_1$ and $3a_1$ is expected (Hu et al., 2011).

Below in Section 2.3.2.1 we discuss the frontier orbital bonding for water on the undoped forsterite(010) surface. This analysis allows us to establish the important features of both the Me-Ow and Ox-Hw bonds on the forsterite surface. We then examine variations in the Me-Ow bonding due to AE and TM cation dopants (Section 2.3.2.2), followed by a similar analysis of the effect from hydrogen bonding (Ox-Hw bond) (Section 2.3.2.3).

2.3.2.1 Frontier orbital analysis for H₂O/forsterite(010)

To develop a frontier orbital analysis for water adsorption on forsterite(010) we use a combination of atom-projected partial density of states (DOS) and the projected crystal orbital Hamiltonian population (COHP). COHP measures the overlap between orbitals of pairs of atoms, which indicates bonding, antibonding, and nonbonding contributions between atoms (Dronskowski and Bloechl, 1993). The advantage of COHP over just visualization of hybridization of orbitals from the DOS is that it provides quantitative measure of the degree of bonding and can be helpful in de-convoluting contributions from the Me-Ow versus Ox-Hw bonds even if they overlap in the orbitals involved. All COHP curves in this study were generated using the LOBSTER program developed by the Dronskowski group (Dronskowski and Bloechl, 1993; Deringer et al., 2011; Maintz et al., 2013; Maintz et al., 2016) and we follow the standard practice of plotting the negative of the COHP such that positive (negative) values indicate bonding (antibonding). It should be noted that COHP should provide bonding information related to charge transfer, both covalent and ionic bonding (Deringer et al., 2011), but it would not capture the non-bonding electrostatic contributions that are also expected to contribute to the water adsorption energy in both the Me-Ow and Ox-Hw (hydrogen bond) interactions. An additional quantitative measure of net bonding contributions between two atoms can be obtained by integrating the COHP curve up to the Fermi level (referred to subsequently as iCOHP).

Fig. 2.4a, b show the MOs of water and the pDOS of the Mg cation and surface oxygen (Ox) before and after adsorption on the pure forsterite(010) surface, respectively,

in the pointing-down configuration. While this configuration is slightly less favored than the flat-lying on the pure forsterite surface, it is the favored configuration in the majority of the other olivine surfaces. A similar Fig. is shown for the flat-lying configuration in the Fig. A8 of Appendix A, and overall the nature of the bonding is similar in both configurations. At the end of this section we will discuss in more detail the primary differences between these two configurations but the initial analysis will focus on the pointing-down configuration. The DOS for water not interacting with the surface (i.e. before adsorption) is obtained by introducing a relaxed H_2O molecule in the middle of the vacuum region above the bare relaxed surface. This approach references the energy levels of the water molecular orbitals relative to the Fermi level of the surface and allows for a clearer picture of the effect of adsorption on both the water orbitals and the surface states. Because molecular water on metal surfaces has been studied in more detail from a frontier orbital analysis perspective, for comparison we have also included a similar figure of the effect of water adsorption on the DOS for H_2O molecule on Pt(111) in Fig. 2.4c, d. The water configuration is the same as reported by Michaelides et al. (2003) and consists of a flat water molecule orientation (details of the H_2O/Pt(111) calculation along with additional COHP/DOS plots can be found in Sec. AIV and Fig. A8 of Appendix A).
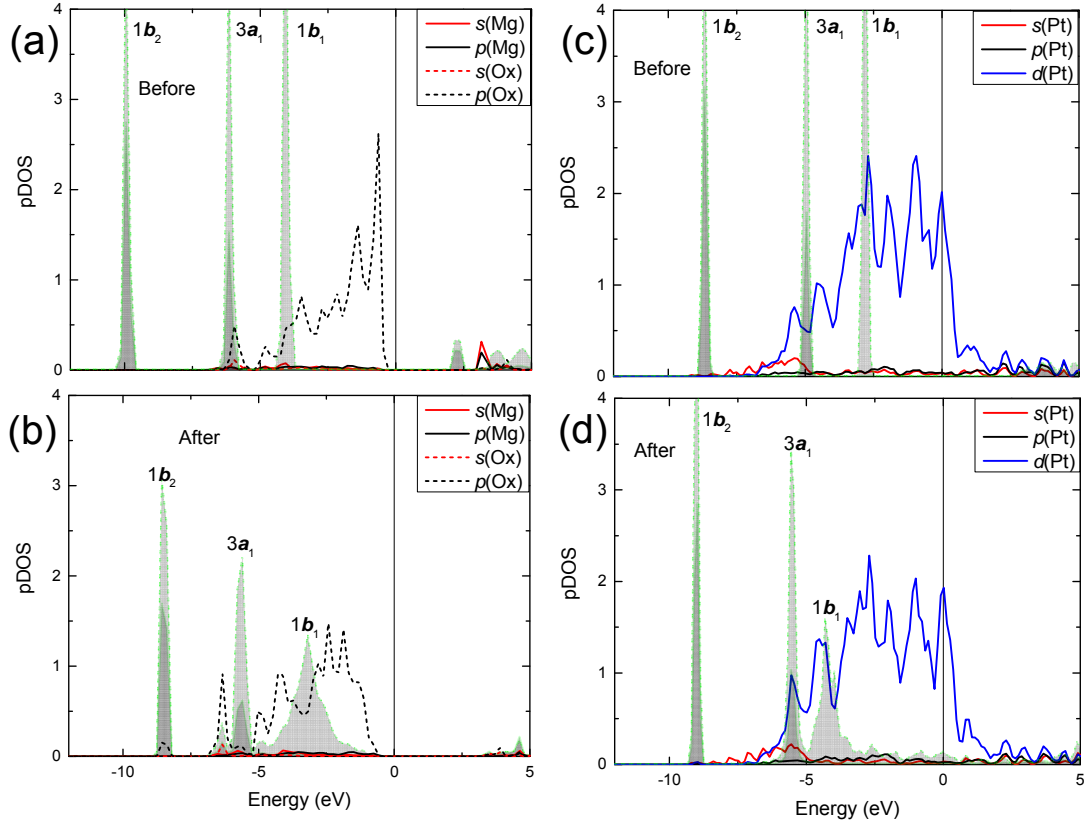
Fig. 2.4. Molecular orbitals of water molecule and the DOS of the interacting surface atoms before and after adsorption on the pure forstertie(010) surface (a, b) and the Pt(111) surface (c, d). Double shaded areas for H_2O indicate the MO involve both *s, p* orbital components.

Several broad conclusions can be made about H_2O bonding on the forsterite(010) surface based on Fig. 2.4. All three of the highest occupied MOs of water ($1b_2$, $3a_1$, and $1b_1$) are affected by adsorption. The shifts in these three orbitals can be connected to hybridization of H_2O and surface states. Furthermore, as shown below with COHP, these three orbitals can also be shown to be involved in the formation of the Me-Ow and Ox-Hw bonds. In contrast, on Pt(111) surface only the $3a_1$ and $1b_1$ exhibit shifts and more importantly these shifts correspond to hybridization of states between H_2O and Pt-*d* states. It has been observed (and we also find the same) that lower energy water molecular orbitals can also shift in energy but these shifts are not associated with any

hybridization, rather they indicate a resonance with broad surface states (Carrasco et al., 2009).

Comparing the MOs of H_2O before and after adsorption on forsterite(010) surface, we can see the energy levels for the MOs of H_2O molecule are all right shifted compared to the water molecule in its gas phase. The right shifting of the energy level indicates the MOs of H_2O are filled with more electrons. This observation matches with the charge transfer obtained from the Bader charge analysis before and after adsorption, which indicates that the water molecule gains 0.05 electrons. In contrast, Michaelides et al. (2003) report that a water molecule transfers around 0.1 electrons to the Pt(111) surface based on a Mulliken population analysis and correspondingly the water molecular orbitals shift downward in energy. Our own Bader analysis indicates a similar charge transfer from H_2O to the Pt(111) surface of around 0.06 electrons. We also observe a much larger polarization of charge on the water molecule upon adsorption on forsterite(010) versus Pt(111) surface. On the forsterite(010) surface upon water adsorption the Ow atom gains 0.15 electrons while the H atoms loose 0.10 electrons. By comparison the Ow (Hw) atom of H_2O on Pt(111) looses 0.01 (0.025) electrons. The larger charge transfer into the Ow atom is reflected in the much larger broadening of the $1b_1$ orbital of H_2O on forsterite(010) (Fig. 2.4b) versus the more narrow broadening on Pt(111) (Fig. 2.4d). This effect of charge transfer into the lone pair orbital of the water molecule is reflected in the lengthening of the O-H bond, which for the pointing-down configuration lengthens from 0.97 to 1.02 Å. The COHP curves of Ow-Hw of the adsorbed water molecule (see Fig. A9 in Appendix A) confirm that the additional charge to the Ow atom induces antibonding contribution from the $1b_1$ orbital from -5 eV to the

Fermi level, with the iCOHP value for the Ow-Hw bond going from +8.04 to +7.13 indicating the weakening of this bond.

The COHP curves for the Mg-Ow and Ox-Hw bonds are shown in Fig. 2.5a, b, respectively, along with relevant partial DOS of the states involved in that bond. We have generated COHP curves where the interaction between the surface atoms with the entire water molecule is summed (e.g. a COHP of H_2O-Mg and H_2O-Ox) and the plots are essentially the same, thus none of the conclusions given below are modified. Overall, the COHP reflects the hybridization that can be observed from the partial DOS - where there is no hybridization the COHP will show no bonding interaction and where there is overlap the COHP curve indicates both the nature (bonding versus antibonding) and strength of that interaction. For both bonds the COHP curves indicate that while there is some hybridization from -5 eV to $\mathcal{E}_f$ (from Fig. 2.4 this is associated with the broadening of the $1b_1$ lone pair orbital), these interactions do not make large contributions to the bonding. Therefore, the majority of the changes seen in the $1b_1$ lone pair orbital upon adsorption are mainly due to charge transfer from the H atoms to O atom within the water molecule. As noted above this is also reflected in the COHP curves of the Hw-Ow bond of the water molecule shown in Appendix A (Fig. A10). The primary contribution to the Mg-Ow bond is through the hybridization of the $3a_1$ water orbital with Mg-s and -p states around -7 to -6 eV below the $\mathcal{E}_f$. As shown in Fig. 2.5a, the $1b_2$ orbital makes no contribution to the Mg-Ow bond and hybridization of this orbital is entirely due to the hydrogen bonding and charge transfer between Ox and the H_2O molecule (Ox-Hw bond). The hydrogen bond with the surface oxygen also has a bonding contribution from the $3a_1$

orbital at the same energy level as observed for Mg-Ow but these contributions are somewhat smaller (see Fig. 2.5b).
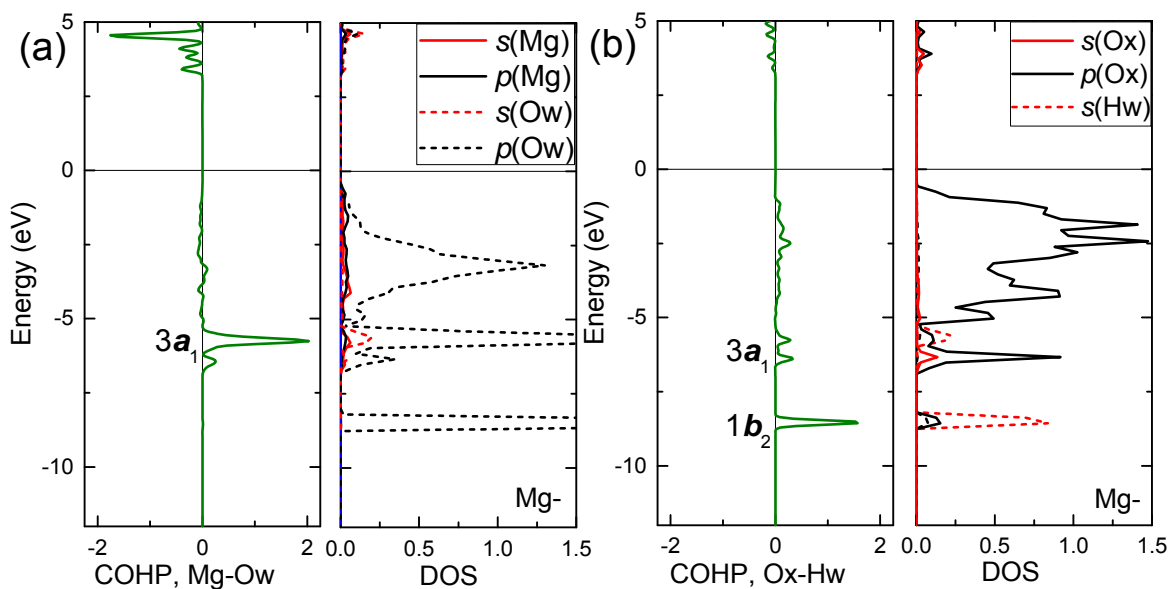
Fig. 2.5. The COHP and DOS for the (a) Mg-Ow and (b) Ox-Hw bond of H_2O on the pure forsterite(010) surface. Positive (negative) values on the COHP curve indicate bonding (antibonding).

In summary, the COHP shows that the hydrogen bonding involves both the $1b_2$ and $3a_1$ orbital, while the Mg-Ow bonding is dominated by the hybridization of the $3a_1$ orbital. While large changes in the $1b_1$ lone pair orbital occur, these are due primarily to large charge transfer into the Ow atom from the H atoms of water and do not have large contributions to the bonding of H_2O with the surface. These conclusions conflict with some of the general expectations in the literature. The common expectation is that the lone pair of the H_2O molecule transfers electrons to the surface cation but on forsterite(010) we observe an increase in the electron density of the lone pair. In addition, the review article by Henderson (Henderson, 2002) suggests no large contribution from any orbitals except $3a_1$ and $1b_1$ while we find that the $1b_2$ orbital is strongly involved in

the hydrogen bond. It is difficult to evaluate this discrepancy since the review article depends on experimental valence photoemission and XPS data of water on oxide surfaces. These experiments would not involve isolated water molecule bonding with the surface and water adsorption can be expected to be very sensitive to the surface oxide structure. Future work examining the changes in water bonding with coverage of water may provide insight into the role of neighboring hydrogen bonding on the frontier orbital picture for water adsorption on these surfaces, since presumably the presence of additional water molecules may dampen hydrogen bonding with the surface oxygen.

While we have focused on the pointing-down configuration of H_2O on forsterite(010) surface, the bonding picture is not dramatically different for the flat-lying configuration. Fig. A8 in Appendix A shows the effects of adsorption on the DOS and the COHP curves for water in the flat-lying configuration on forsterite(010) surface. The fundamental observations remain the same with large charge transfer from the H atoms to the Ow atom and the same orbitals involved in the Mg-Ow and Ox-Hw bonds. The primary difference is that the hydrogen bond strength is weakened in the flat-lying configuration. This is reflected by a drop in iCOHP value for the Ox-Hw bond from +1.13 to +0.58 going from pointing-down to flat-lying, while the iCOHP for the Mg-Ow bond is within 0.01. This drop in bonding is almost entirely due to the longer Ox-Hw bond that the water molecule is constrained to have in the flat-lying configuration. The Ox-Hw bond distance increases from 1.71 to 1.99 Å for flat-lying versus pointing-down, while the Mg-Ow bond distance can be maintained essentially the same in both configurations (~ 2.10 Å). In subsequent sections where we discuss the impact on these

two bonds due to changes in the cation type, we will focus only on the pointing-down configuration.

2.3.2.2 Effect of doping on Me-Ow bonding

To understand the effect of cation doping on Me-Ow bonding due to the type of dopant, we examine Ca and Fe as representatives of the AE and TM cation dopants, respectively. The Me-Ow COHP along with the corresponding DOS for pure forsterite, Ca-doped forsterite, and Fe-doped forsterite are plotted in Fig. 2.6. As discussed earlier for forsterite all the bonding is represented above -12 eV for both AE- and TM-doped forsterite. Similar COHP and DOS plots for the rest of the AE and TM dopants, can be found in Sec. AIV (Fig. A6) of Appendix A.

In Fig. 2.6, we can see from the COHP plots that the major feature associated with Me-Ow bonding is the $3a_1$ orbital of water molecule. The main contribution to this MO is the Ow-$2p$ orbital, reflected in the DOS plot. However, the mechanisms for Me-Ow bonding in Fig. 2.6 for the three metal cations are not the same. For the Mg-Ow and Ca-Ow bonds, both of which are AE metals, we can see the s and p orbitals of the metal cations contribute to the bonding as seen in Fig. 2.6b, d. However, as seen in Fig. 2.6a versus Fig. 2.6c, the corresponding COHP magnitude for Ca-Ow is much weaker than that of Mg-Ow. This decrease in Me-Ow interactions for Ca-doped forsterite is also reflected by the Me-Ow iCOHP parameter which decreases from +0.90 for forsterite to +0.49 for Ca-doped forsterite. The adsorption energy for forsterite (-138.1 kJ/mol) versus Ca-doped forsterite (-125.3 kJ/mol) does show a decrease but not to the extent one would expect from such a large loss of Me-Ow bonding. As discussed in Sec. 2.3.2.3 the Ox-Hw bond is slightly stronger for Ca-doped forsterite but as we discuss in more detail at the

end of this section we also expect a major contribution to water-Me interactions due to electrostatic interactions. These are not captured by the COHP analysis of Me-Ow atom pair since it does not involve direct charge transfer between metal and Ow atoms.

Another question that arises from the COHP results for Ca-doped forsterite is the source behind the large drop in Me-Ow bonding. We attribute this to the presence of more electrons in Ca, including the appearance of some filled d-states as seen in Fig. 2.6d. We note the d-states appear due to some electron transfer from the O lattice atoms and similar observations have been reported for Ca-adsorbed graphene (Ataca et al., 2009). The higher density of states in the range of -5 to 0 eV for Ca-doped forsterite leads to filled antibonding states in the Ca-Ow bond due to Pauling repulsion. To confirm our hypothesis, we have replaced Mg by Ca on the pure forsterite(010) surface, and performed a single point calculation to observe the COHP changes for Ca-H_2O restricted to the bonding geometry found on forsterite. The resulting COHP and the DOS plots can be seen in Fig. A12 in Appendix A. As expected, stronger antibonding feature is seen in the COHP around -3 eV below the Fermi level caused by the Ca-3d electrons. The repulsion forces the water molecule to move away from Ca resulting in a longer and weaker Ca-Ow bond. Similar observations about the Me-Ow bond hold for Sr-H_2O and Ba-H_2O interactions (Fig. A6 in Appendix A).

In contrast to Ca, doping of the Mg with a TM like Fe results in considerably different type of bonding. As seen in Fig. 2.6f, Fe-Ow bond exhibits a strong hybridization between the Fe-d and Ow-$2p$, which indicates typical covalent bonding. In addition to the bonding interactions there is also anti-bonding features near the $\mathcal{E}_f$ (Fig.

2.6e, f). Overall, the iCOHP value for Fe-Ow is larger (+1.15) than Mg-Ow (+0.90) and Ca-Ow (+0.49) reflecting the stronger covalent bond found for the TM-Ow interaction.
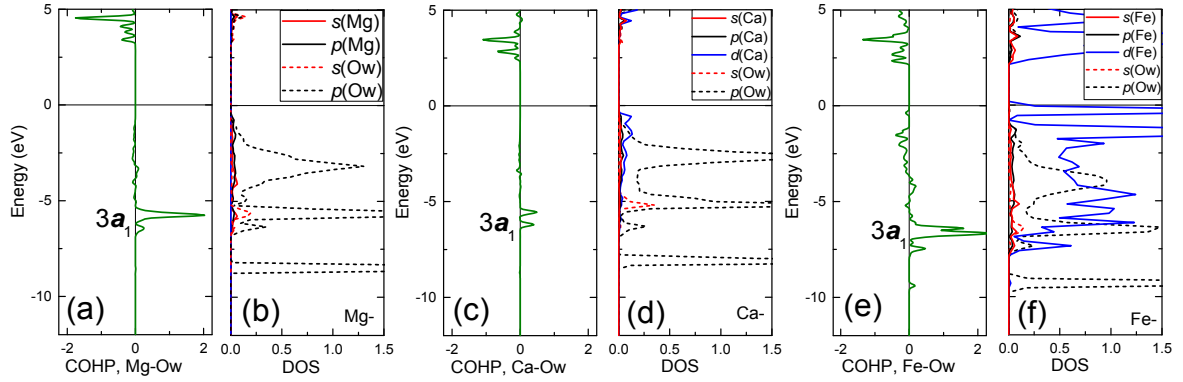
Fig. 2.6. COHP and DOS plots for Me-Ow bond on the pure Fo (a, b), Ca-doped (c, d), and Fe-doped (e, f) (010) surfaces.

Based on the above discussion we expect to see stronger covalent bonding for the TM cation and relatively weaker bonding for the AE cations. Fig. 2.7 plots the iCOHP for the Me-Ow bond versus its bond distance. The expectation is a stronger covalent bond should lead to a smaller Me-Ow bond distance. While Fig. 2.7 does show that TM cations have stronger covalent interaction reflected by larger iCOHP values, we find that the TM and AE cations display different linear trends.
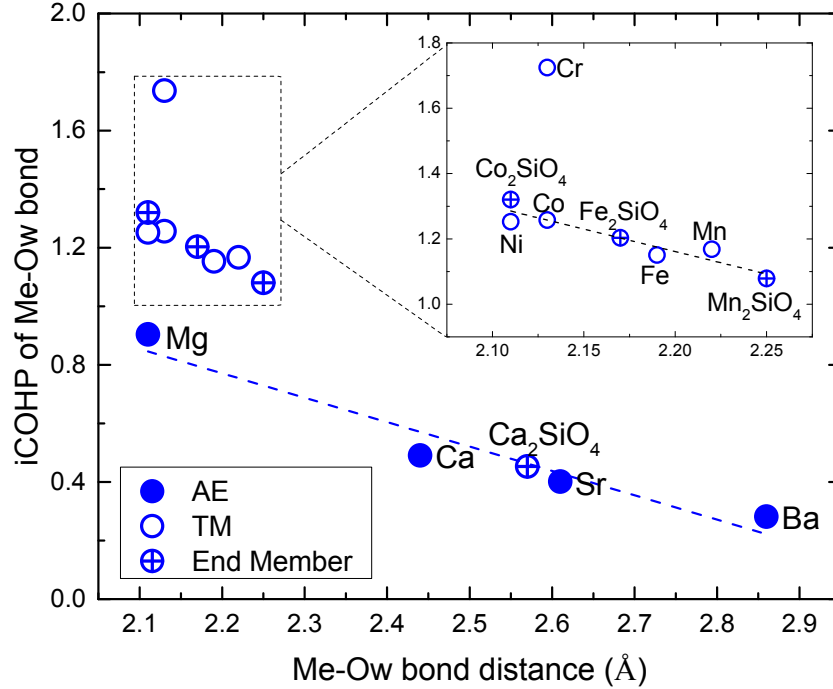
Fig. 2.7. The iCOHP of the Me-Ow bond versus the bond distance for water adsorbed on different doped forsterite surfaces and end member olivine surfaces. The inset shows the TM dopants and end-members and the fitted dashed lines illustrate the linear trends for the AE and TM cations (inset), respectively.

The AE-Ow bond distance shows a linear relationship with their corresponding iCOHP values including Ca-olivine. On the other hand, TM-Ow bonds form another linear trend with a shorter range of Me-Ow bond distances, with Cr being an outlier. Fig. 2.7 reinforces that AE-Ow and TM-Ow bonds are fundamentally different types of bonds as observed in the COHP and pDOS plots. Among the TM dopant cations, Cr-H_2O interaction generates the strongest Cr-Ow bond (iCOHP of 1.74); however, the E_{ads} for Cr-H_2O is not the highest (refer to Table 2.2). We have observed that the interaction of Cr-H_2O caused a large distortion on Cr from the surface. The Cr cation moves substantially out of the surface and forms a strong covalent bond with H_2O. The

distortion energy can be used to estimate how the displacement of the dopant cation affects the $\boldsymbol{E}_{\text{ads}}$. We define the surface distortion energy E_{surf}^{dist} as follows:

$$E_{surf}^{dist} = E_{surf}^{ads} - E_{surf}^{bare,relaxed} \qquad\qquad \text{Eqn (2.2)}$$

where E_{surf}^{ads} is the energy of the surface after adsorption without the adsorbate, and $E_{surf}^{bare,relaxed}$ is the energy of the relaxed surface before adsorption. The E_{surf}^{dist} contributed by Cr is 45.0 kJ/mol, whereas it is in the range of 16.5 to 24.0 kJ/mol for the rest of the TM cations. The large E_{surf}^{dist} for Cr reduces the overall $\boldsymbol{E}_{\text{ads}}$ for Cr-doped forsterite resulting in a lower adsorption energy than what would be expected from just the strength of the Me-Ow bond. From Table 2.2, the binding of water on the TM dopants follows the sequence Mn > Co > Ni ~ Cr > Fe. The prominent factor for the strong capacity of Mn with H_2O is its smaller distortion energy (16.5 kJ/mol) compared to the others (22.3, 24.0, and 23.4 kJ/mol for Co, Ni, and Fe), Interestingly, the three dopant cations (Mn, Fe, and Co) and their corresponding end members show very similar positions in the inset of Fig. 2.7, which suggests the single water molecule interacts locally with the dopant cations, and the bond nature/strength is dependent on the metal types.

Returning to Fig. 2.7, we observe that forsterite has a larger $\boldsymbol{E}_{\text{ads}}$ than any of the TM dopants despite having a smaller Me-Ow iCOHP value. Furthermore, the large drop in iCOHP from Mg to Ca is not reflected in a large drop in adsorption energy. Similarly, Ca, Sr, and Ba dopants do not show large differences in iCOHP values but do show larger differences in adsorption energy. As mentioned above, we hypothesized that the electrostatic interaction between AE-H_2O is not captured in the COHP analysis since it is not due to direct charge transfer between metal and Ow atoms. Instead, as in forsterite,

we observe large charge transfer from the Hw atoms to the Ow atoms in all the AE systems suggesting that there may be an enhanced electrostatic interaction between H_2O and the AE cations. To test this, we attempted to correlate the AE-Ow interaction with the ionic size of the AE metals. Fig. 2.8 plots E_{ads} versus the AE cation ionic radii for the AE-doped forsterite surfaces. Ionic radii data for a coordination number of six was used as the cations in olivine structure are the center of octahedron, where Mg = 0.72 Å, Ca = 1.00 Å, Sr = 1.18 Å, and Ba = 1.35 Å (Shannon and Prewitt, 1969; Shannon, 1976; Giacovazzo et al., 1992). In Fig. 2.8, we can see that for both H_2O configurations (pointing-down and flat-lying) the adsorption energy weakens with increasing ionic radii as expected in ionic bonding, which suggests the AE-Ow interaction has a large electrostatic component. We discuss a semi-quantitative approach to estimate the relative contributions to the electrostatic interaction energy between H_2O and metal cation in Section 2.3.3.
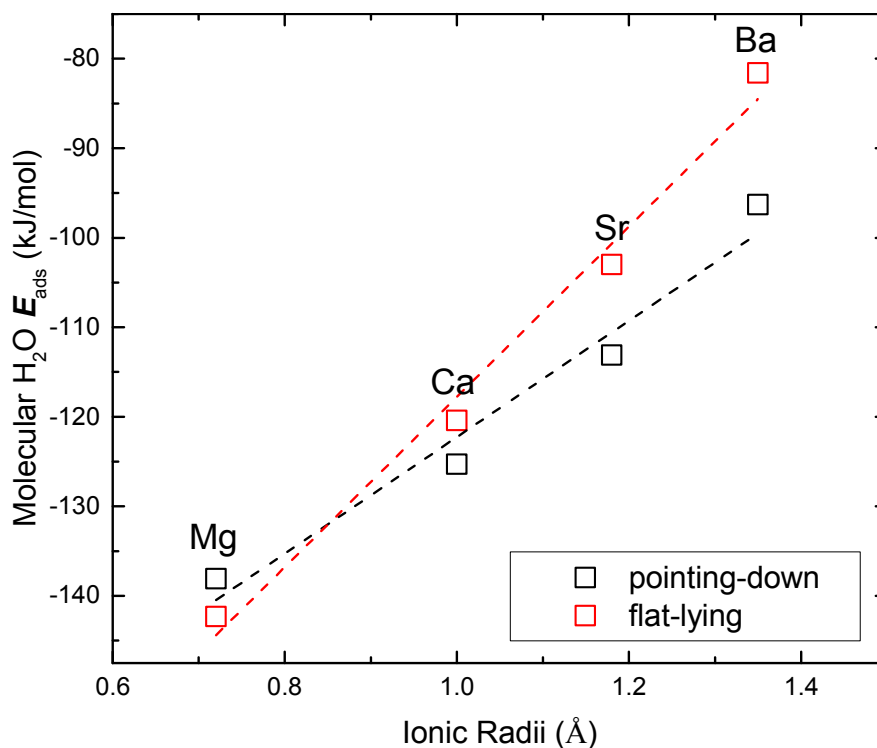
Fig. 2.8. Adsorption energy of molecular water versus ionic radii of the AE cation on the AE-doped forsterite(010) surfaces.

2.3.2.3 Effect of doping on Ox-Hw bonding

For the Ox-Hw hydrogen bonding, the COHP/DOS plots are similar for all surfaces in this study indicating the bonding nature does not change with dopants. The COHP/DOS information for hydrogen bonding on the various olivine surfaces is reported in Fig. A6 in Sec. AIV of Appendix A. Fig. 2.9 plots the observed Ox-Hw bond versus the Ox-Hw iCOHP value for all dopants and end-member olivine surfaces except for Ca-olivine. Ca-olivine results in a noticeably different H_2O down configuration with respect to the Ox-Hw bond and will be discussed further below. As shown in Fig. 2.9, a linear relationship is observed for Ox-Hw bond between its iCOHP value and bond distance indicating that the nature of the hydrogen bond is similar on all the surfaces unlike what

we found for the Me-Ow bond. For the doped forsterite surfaces, the strength of the hydrogen bond is inversely correlated to the strength of the Me-Ow bond through a structural constraint. A shorter Me-Ow bond (more covalent) brings the water molecule closer to the metal cation and away from the adjacent Ox atom and thus weakening the Ox-Hw bond. Therefore, as shown in Fig. 2.9, the hydrogen boding is generally stronger on AE-doped surfaces than on TM-doped surfaces, which exhibit higher Me-Ow iCOHP values and shorter Me-Ow bond distances. It should be noted, however, that Cr and Mn also have stronger hydrogen bonding than the other TM dopants. Mn-dopant shows the weakest Me-Ow bond (see Fig. 2.7) and this partially explains the observed stronger hydrogen bond for this dopant, but Cr is a unique case and is able to create relatively strong Me-Ow and Ox-Hw bonds. This exception for Cr is due to the large displacement of Cr away from the surface, and as discussed in Sec. 2.3.2.2 this large distortion allows Cr to have an exceptionally strong Cr-Ow bond. This distortion also allows the water molecule to move towards the Ox atom and maintain a relatively strong Ox-Hw bond. The AE dopants generally have stronger hydrogen bonds because they have weak covalent interactions with the metal cation and thus have large Me-Ow distances that allow for closer Ox-Hw distances. As would be expected from our observation that the forsterite surface is the only AE surface to also show some strong covalent contribution, the forsterite surface has the weakest hydrogen bond of all the AE forsterite surfaces.
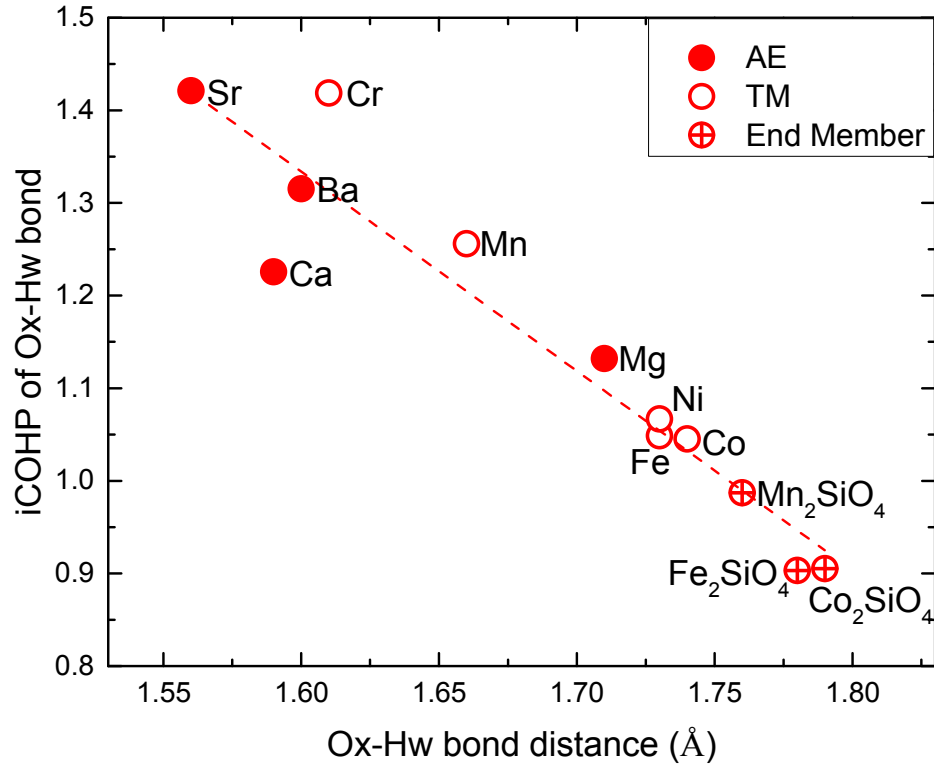
Fig. 2.9. Relationship between the iCOHP and bond distance for Ox-Hw bond on each surface. Note that the result for the Ca-olivine surface does not fit in this trend, as its exceptional lattice size contributes to an Ox-Hw bond distance - iCOHP relationship that falls outside the values presented here.

As discussed in Section 2.3.2.2 (see Fig. 2.7), the Me-Ow bond strength overlaps closely between dopants and their corresponding end members. As seen in Fig. 2.9, this observation does not hold for the hydrogen bond where most end members show weaker hydrogen bonds. This difference for the hydrogen bond between dopants and end members can be explained due to the structural constraints placed on the water molecule. The end members have larger lattice sizes than forsterite, which make it more difficult to maintain a close distance to the adjacent Ox atom and results in generally weaker H-bonding for water on the end member in comparison to the doped-forsterite analog. This constraint is most important for Ca-olivine, which has the largest lattice size (see Table

2.1). Unlike the other end members, the Ox-Hw bond on Ca-olivine is exceptionally short, with a distance of 1.41 Å. To understand this contradiction for Ca-olivine, the pointing-down H_2O configurations on Ca-doped and Ca-olivine(010) surfaces are shown in Fig. 2.10. The Ca-Ow and Ox-Hw bond distances are labeled in Fig. 2.10, along with the Ca-Ox distances, which is 4.42 Å on Ca-olivine versus 3.99 Å on the Ca-doped forsterite surface. The larger lattice space for Ca-olivine enables water molecule to reorient on the surface, where we can see that in Fig. 2.10a the molecule is almost perpendicular to the surface with Ow locating in the middle of two Ca atoms. This reorientation leads to a much shorter Ox-Hw bond distance (1.41 Å) on Ca-olivine while allowing the water molecule to retain the Ca-Ow bond similar to that observed for Ca-doped forsterite. Regarding the water molecule, we can see the H-O-H angles are 104.3° on Ca-olivine vs 102.8° on doped surface. One of the Ox-Hw bond distances is 1.10 Å on Ca-olivine surface vs 1.03 Å on doped surface. Such different bond features indicate the H_2O on Ca-olivine is stretched and likely more prone to water dissociation. For Sr-olivine, which has a larger lattice constant than Ca-olivine, we could not stabilize a water molecule in the pointing-down configuration because it dissociates due to the larger distance between Sr and Ox on the surface (5.18 Å).
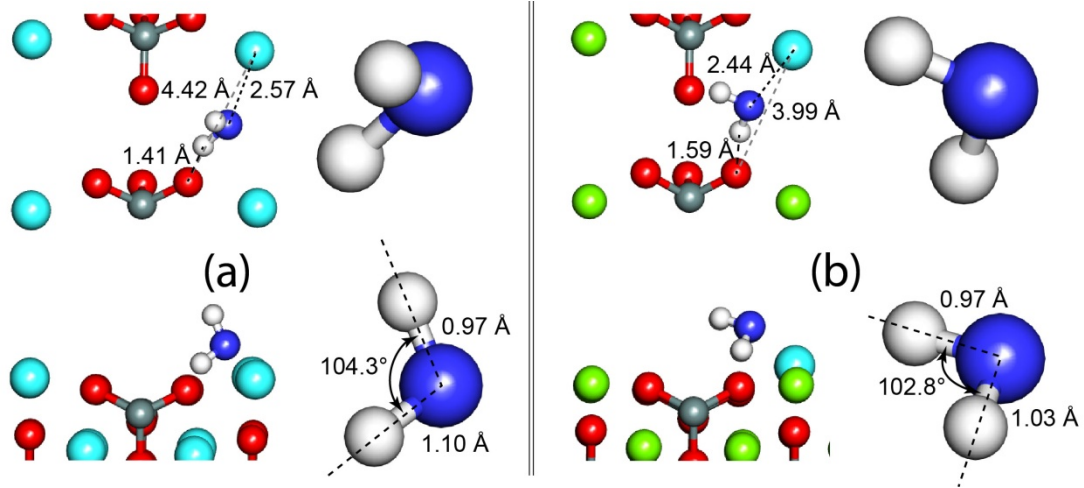
Fig. 2.10. The top and side views of the pointing-down H_2O configuration on the (a) Ca-olivine(010) surface, and (b) Ca-doped forsterite(010) surface. A magnified image of the adsorbed H_2O is also shown to clearly observe differences in the water orientation and bonding geometry on the two surfaces.

2.3.3 Combined contributions to H_2O bonding on olivine(010) surface

Based on the discussion in Section 2.3.2, we conclude that iCOHP is a good measure of the covalent Me-Ow bond and the hydrogen bond (Ox-Hw). Nevertheless, the iCOHP fails to captures the large water-cation electrostatic interactions, which are enhanced for the AE where strong H_2O polarization is observed along with larger positive Bader charges on the AE cations. To further support this conclusion, we have calculated the Coulombic electrostatic interaction energy (E_c) between H_2O and the metal cation using the following expression:

$$E_c = \sum \frac{q_{Me} q_i}{4\pi\epsilon_0 r_i}$$

Eqn (2.3)

where q_{Me} is the Bader charge on the metal cation, q_i the Bader charge on oxygen and hydrogen atoms of the water molecule, and r_i the distance between the metal cation and the oxygen and hydrogen atoms of the water molecule. A similar approach has been used

by others to get an estimate of the electrostatic interaction energy between adsorbate and the surface (Preuss et al., 2005; P. Wang et al., 2014). However, it must be stressed that this energy cannot be directly related to adsorption energy but instead is useful in showing the relative strength of the electrostatic interactions mediating the H_2O-metal interactions.

Furthermore, there are two other contributions to adsorption energy: surface distortion energy (defined by Eqn 2.2) and the dispersion energy. The van der Waals interactions are calculated by the D3 dispersion correction in this study. As the dispersion correction is an added term to the total energy, we can evaluate the contribution from dispersion to the adsorption energy, $E_{disp,ads}$, by the following:

$$E_{disp,ads} = E_{disp,sys} - E_{disp,slab} - E_{disp,H_2O(g)}$$

Eqn (2.4)

where the definition of each term is the same as E_{ads} calculation, but here only the dispersive portion of the energy is used. Table 2.3 summarizes all of these various interactions for each of the surface examined in this study.

Table 2.3. Parameters characterizing the strength of the various contributions to molecular water adsorption on all surfaces examined in this study*.

	E_{ads} (kJ/mol)	iCOHP, Me-Ow	Me-Ow (Å)	iCOHP, Ox-Hw	Ox-Hw (Å)	E_{dist} (kJ/mol)	Displacement of Me (Å)	$E_{disp,ads}$ (kJ/mol)	E_c (kJ/mol)
Mn-	-124.0	+1.17	2.22	+1.26	1.66	16.5	0.24	-19.4	-216.6
Co-	-121.0	+1.26	2.13	+1.05	1.74	22.3	0.28	-19.5	-188.0
Ni-	-112.9	+1.25	2.11	+1.07	1.73	24.0	0.27	-19.9	-174.8
Cr-	-111.5	+1.74	2.13	+1.42	1.61	45.0	0.41	-19.0	-252.4
Fe-	-100.8	+1.15	2.19	+1.05	1.73	23.4	0.27	-19.3	-200.7
Mg_2SiO_4	-138.1	+0.90	2.11	+1.13	1.71	18.9	0.24	-20.3	-337.5
Ca-	-125.3	+0.49	2.44	+1.23	1.59	6.5	0.05	-18.4	-227.3
Sr-	-113.1	+0.40	2.61	+1.42	1.56	6.7	0.08	-15.8	-238.6
Ba-	-96.3	+0.28	2.86	+1.32	1.60	6.7	0.09	-15.6	-170.1
Ca_2SiO_4	-129.1	+0.45	2.57	+1.45	1.41	23.2	0.30	-17.3	-398.4
Mn_2SiO_4	-111.3	+1.08	2.25	+0.99	1.76	21.1	0.34	-21.0	-223.1
Co_2SiO_4	-123.8	+1.32	2.11	+0.91	1.79	21.1	0.35	-17.0	-229.3
Fe_2SiO_4	-100.2	+1.20	2.17	+0.90	1.78	27.7	0.34	-19.9	-191.7

*: Sr_2SiO_4 is not included, as the pointing-down H_2O would not stabilize on its (010) surface, but dissociates instead.

From Table 2.3 it is clear that one type of contribution does not dominate the water-surface interactions. It is useful to examine several specific surfaces to illustrate how Table 2.3 can be used qualitatively to reconcile the observed E_{ads} values. Using Eqn 2.3 gives a E_c value of -337.5 kJ/mol for forstertite versus values in the range of ~200 kJ/mol for the TM dopants (with Cr as an exception at 252.4 kJ/mol due to shorter Ow-Cr bond distance). This result reflects the larger cation charge and polarization of the water molecule on forsterite versus the TM-doped forsterite surfaces. This electrostatic interaction energy difference is substantial (almost 75% larger on forsterite) and is the source of water binding the strongest on the forsterite surface despite the relatively weaker Me-Ow covalent bond. E_c drops when moving from forsterite to Ca-, Sr-, and Ba-doped forsterite following the inversely proportional relationship of E_c to distance but for one exception between Ca- and Sr-dopants. While the distance between Me-Ow is greater for the Sr-dopant, Bader charge on the Sr atom is higher than on the Ca-dopant and the

water molecule undergoes a slightly larger polarization on the Sr-doped forsterite surface. This behavior of the Bader charges might be a reflection of the differences in Me-Ow and Ox-Hw bonds between these two surfaces, but the overall effect is that the electrostatic interaction energy is similar on the Ca- and Sr-doped forsterite surfaces.

A comparison of forsterite to Ca-olivine shows that Ca-olivine has the stronger electrostatic interaction and a stronger hydrogen bond, but the covalent contribution to Me-Ow on Ca-olivine is 50% of what is found on forsterite. This difference in Me-Ow bond strength combined with more favorable distortion and dispersion energy allows for stronger adsorption of H_2O on the forsterite surface versus Ca-olivine.

As discussed in Section 2.3.2.2, the Cr-dopant shows a substantially stronger covalent Me-Ow bond and Ox-Hw bond than the other TM dopants such as Mn, Co, and Ni; in addition it shows a stronger contribution from the electrostatic interaction energy due to the shorter Me-Ow bond distance. However, due to the exceptionally large distortion of the Cr atom and corresponding large surface distortion cost (nearly ~ 20 kJ/mol more than the other TM dopants), the Cr-doped forsterite has an E_{ads} value nearly the same as for the Ni- and Fe-doped forsterite surfaces.

Table 2.3 also illustrates the effect of lattice size dimension of the end-members on the resulting E_{ads}. The H_2O adsorption configuration on Ca-olivine discussed above suggests that end-members with small differences in lattice constants from forsterite will show very similar H_2O adsorption energy to the doped-forsterite surface. For example, molecular water shows similar contributions from Me-Ow, Ox-Hw, surface distortion energy, and dispersion energy between dopant Fe and Fe_2SiO_4, as well as between dopant Co and Co_2SiO_4. Both these olivine structures have similar lattice constants to forsterite.

However, Mn$_2$SiO$_4$ has a larger lattice constant than forsterite (see in Table 2.1), and we find that the adsorption energy on Mn$_2$SiO$_4$(010) is lower than Mn-doped forsterite(010) by 12.7 kJ/mol. From Table 2.3 we can understand this difference in adsorption energy. The TMs have strong covalent Me-Ow bonds, which for both Mn-doped forsterite and Mn$_2$SiO$_4$ are similar. Therefore, the water configuration is controlled by the Me-Ow interaction, and for Mn$_2$SiO$_4$ with a larger lattice constant this prevents the water molecule from forming as strong a Ox-Hw bond as found on Mn-doped forsterite as reflected by the iCOHP value and bond distance shown in Table 2.3.

Although Ca-olivine has the largest lattice constant among all end members (excluding Sr-olivine), molecular water has a similar E_{ads} between dopant Ca and Ca-olivine. This occurs because of a trade-off between the various contributions as can be seen in Table 2.3. On Ca-olivine, the larger lattice constant combined with relatively weak Me-Ow covalent bond allows the water molecule to move toward the lattice Ox atom and form a strong Ox-Hw bond as reflected by the large iCOHP value and short Ox-Hw bond length. However, the Ca atom in Ca-olivine does have a larger electrostatic interaction with the water molecule and this leads to Ca atom displacement and corresponding larger surface distortion energy cost in comparison to Ca-doped olivine (23.2 versus 6.5 kJ/mol).

2.4 Conclusions

Changes to molecular water adsorption on forsterite(010) surface due to the presence of AE and TM cation doping was examined using DFT. Dopants were modeled by introducing a single dopant onto the pure forsterite(010) surface, which is sufficient to capture local H$_2$O-dopant interactions. Water adsorption on pure end member

olivine(010) surfaces (Ca$_2$SiO$_4$, Sr$_2$SiO$_4$, Mn$_2$SiO$_4$, Fe$_2$SiO$_4$, and Co$_2$SiO$_4$) consisting of the same cation as the dopants were also examined to better understand the impact of local dopant-water interactions versus bulk composition. Two stable water configurations are found on all surfaces considered except for Sr-olivine, with the predominantly more stable configuration involving a Me-Ow bond and an Ox-H hydrogen bond. While pure forsterite(010) shows stronger water adsorption than the TM dopants (as measured by E_{ads}), there is no simple relationship between E_{ads} and the cation charge.

For the two chemical bonds on the surface, i.e., Me-Ow and Ox-Hw, we utilized iCOHP as a parameter that accounts for the bond strength, and observed linear relationships exist between bond distance and iCOHP. For the Ox-Hw bond, the shorter Ox-Hw bond distance and larger iCOHP value, the stronger the hydrogen bonding. Conversely, the Me-Ow bond does not exhibit a single linear trend, but rather the TM-Ow and AE-Ow trends are separate and distinct. The TM atoms form covalent bonds with Ow atom due to the strong hybridization between TM-d and Ow-$2p$ orbitals. The AE-Ow bonding is primarily formed via electrostatic forces, confirmed by a weaker orbital hybridization (and smaller iCOHP for the AE-Ow bond), and the discovery that the ionic size of AE has a linear relationship with the adsorption energy. Nevertheless, the bonding information by itself is not enough to delineate the relationship between adsorption energy and different dopants, the contribution from the surface lattice distortion on adsorption must also be considered. For example, although Cr-H$_2$O exhibits a relatively strong interaction for both Cr-Ow and Ox-Hw bonds (shorter bond distances), the adsorption energy is not as large as that of Mn-H$_2$O because the surface distortion energy and displacement of Cr atom on the Cr-doped surface is significantly greater than

other TM dopants. The detailed bonding picture that emerges from this study shows the trade-offs that occur in water molecule adsorption on the olivine surfaces and how the AE and TM dopants contribute distinct Me-Ow interactions that triggers differences in hydrogen bonding. Future work will have to examine how these differences in water molecule-metal cation interactions are affected by surrounding water molecules, which will be important for understanding key geochemical behavior such as dissolution, mineral transformation (as in serpentinization) and catalytic reactions among C-O-H fluids.

Chapter 3: Structure and Dynamics of Water on Forsterite Surface

3.1 Introduction

Molecular dynamics (MD) simulation facilitates a molecular scale understanding of the structure and dynamics of water molecules in the interface region. Kerisit et al. (2012) have investigated water on forsterite surfaces using MD simulation, together with CO_2 under the condition of 50°C and 180 bar to simulate the scenario of CO_2 injection into basaltic rocks on a solvated interface. Their focus has been on the form and transport of the supercritical (sc) CO_2 on the interface, and they concluded that it depends on the water content on the interface.

We have applied a classical MD simulation using empirical force fields in this study to investigate the structural and dynamical properties of water on the forsterite(010) surface. In MD simulations, Newton's equations of motion for a system of atoms/molecules are solved to obtain atomic/molecular trajectories in time, from which various quantities of interest can be calculated.

In addition to MD simulations, neutron scattering is another useful technique often used to study surface water. In neutron scattering experiments, neutrons coming from a source are scattered from a material of interest and their detection is studied as a function of the energy they exchanged with the scattering material and the change in their direction after the scattering. The exceptionally large incoherent neutron scattering cross-section of hydrogen compared to that of other elements makes neutron scattering an ideal

technique to study the dynamics of surface water. We employed quasi-elastic neutron scattering (QENS) to obtain information on the dynamics of water on forsterite surface that was compared with the MD simulation results. In a QENS experiment, broadening of an elastic line (spectral line originating from elastic scattering, with no exchange of energy involved between the neutrons and scattering material) due to stochastic motions of atoms in the scattering material is studied. The extent of this broadening gives information on the time scales of stochastic motion while its variation in scattering direction provides important information on the mechanisms and geometry of the stochastic motion. Recent studies coupling MD simulation and QENS data have mainly addressed the interaction between water and some metal oxide and mineral surfaces (Mamontov et al., 2007; Mamontov et al., 2008; Stack et al., 2016). Defined as distinct layers (namely the innermost, the intermediate and the outermost layers), they have shown different dynamic features on the hydroxylated surfaces. We combined MD and scattering to investigate the dynamic behavior of water on the hydroxylated forsterite(010) surface (denoted as Fo(010) thereafter) which resembles the real mineral surface in ambient condition to the largest extent, and discovered the unique structure of the surface water.

3.2 MD simulations

Molecular dynamics (MD) simulations were performed using DL_POLY software package (Todorov et al., 2006). Among the common crystal planes of olivine minerals, (010) surface has been widely examined since it is relatively stable with a lower surface energy, evidenced by previous simulation studies (de Leeuw et al., 2000; Stimpfl et al., 2006).

The simulation box in this study is composed of a forsterite (*Pbnm* space group, *a* = 4.753 Å, *b* =10.199 Å, *c* =5.981 Å, experimental unit cell determined by Lager et al. (1981)) slab with a unit cell replicated 6 × 1.5 × 6 times and an additional free space (~ 85 Å) along the *b*-axis to allow water molecules to move. The slab consists of 1512 atoms. The two (010) surface sides are cleaved to be non-dipolar and Si-O tetrahedron is kept intact.

Kerisit et al. (2012) examined supercritical CO_2/H_2O on the bare and hydroxylated Fo(010) surfaces at the condition of 50˚C and 180 atm. We follow the same potential parameters as in Kerisit et al. (2012), including the modified CLAYFF model (Cygan et al., 2004) for forsterite and Lennard-Jones interactions. The interaction between Mg and water-oxygen (Ow) is described by Buckingham potentials, which have been used in a number of MgO/water and forsterite/water MD studies (de Leeuw and Parker, 1998; de Leeuw et al., 2000; King et al., 2010; Kerisit et al., 2012). The hydroxylated surface in this study is decorated by assigning OH groups to every Mg atom on the surface, and H group to the surface oxygen atom (Ox) next to the Mg atom. The charge in forsterite follows Kerisit et al. (2012) that is modified from CLAYFF model. In the forsterite slab, Mg=+2.0 e, Si=+2.1 e, O=-1.525 e; while for the Ox, the H binding with Ox, and the O and H atoms of the OH group, their charges are -0.950 e, +0.4248 e, -1.425 e, and +0.4250 e, respectively. The SPC/E model for water (Berendsen et al., 1987) was used in this study, where the bond length of O-H and bond angle of H-O-H were fixed at the values of 1 Å and 109.47˚. The charges for Ow and Hw atoms are -0.8476 e and +0.4238 e, respectively.

Based on definition in Kerisit et al. (2013), one Mg atom on Fo(010) surface can accommodate two water molecules as one monolayer (1ML). Accordingly, the total number of water molecules on the (010) surface is 144, which satisfies the coverage of 1ML on both sides of the slab. This coverage is equivalent to 7.1 H_2O/nm^2.

Simulations were conducted at 270 K with NVT ensemble (also called 'Canonical ensemble', constant number of particles, constant volume, and constant temperature) using Nosé-Hoover thermostat. The temperature was selected to remain the same as the QENS experiment. The simulation was performed in two steps. First, only the hydroxylated slab was equilibrated. The Mg, Si, and O atoms (including the O of the OH group) were kept immobile, but all the H atoms were set to move for 4 ns. Second, water molecules were added onto the surface, and the molecules and the H atoms on the hydroxylated surface were free to move for 2.5 ns for equilibrium. Attainment of equilibrium was ascertained by the variation in the total energy and temperature of the system being less than 7% of their constant value. After equilibration, a production run of 1.5 ns was carried out to calculate average quantities of interest. The Velocity Verlet (VV) algorithm was used to advance the atom positions. Time step was 1 fs for each step of movement, while the trajectories were recorded at an interval of 0.02 ps. Periodic boundary conditions were applied in all directions. The system thus consisted of infinitely large planes of forsterite surface stacking above each other with a spacing of 85 Å. This large spacing ensures that interfacial surface behavior dominates over the slit-like confinement effect. To ensure that there is no interaction between images of water molecules in adjacent cells, a cutoff distance of 13 Å, shorter than the forsterite slab thickness was used.

3.3 QENS experiment

3.3.1 Sample synthesis and hydration

Synthetic nanopowdered forsterite sample was used in the QENS experiment. The synthesis route can be referred to Anovitz et al. (2017). The purpose of producing nanopowdered sample is to provide enough surface area for water adsorption, thus the statistics from neutron scattering is meaningful. The crystal form and sample morphology can be referred to the following SEM pictures (Fig. 3.1). From Fig. 3.1, it is estimated that the particle size of the sample is 100 ~ 250 nm. The particles commonly show a flaky feature in morphology. The corresponding BET surface area of the sample is 66.0 m^2/g.
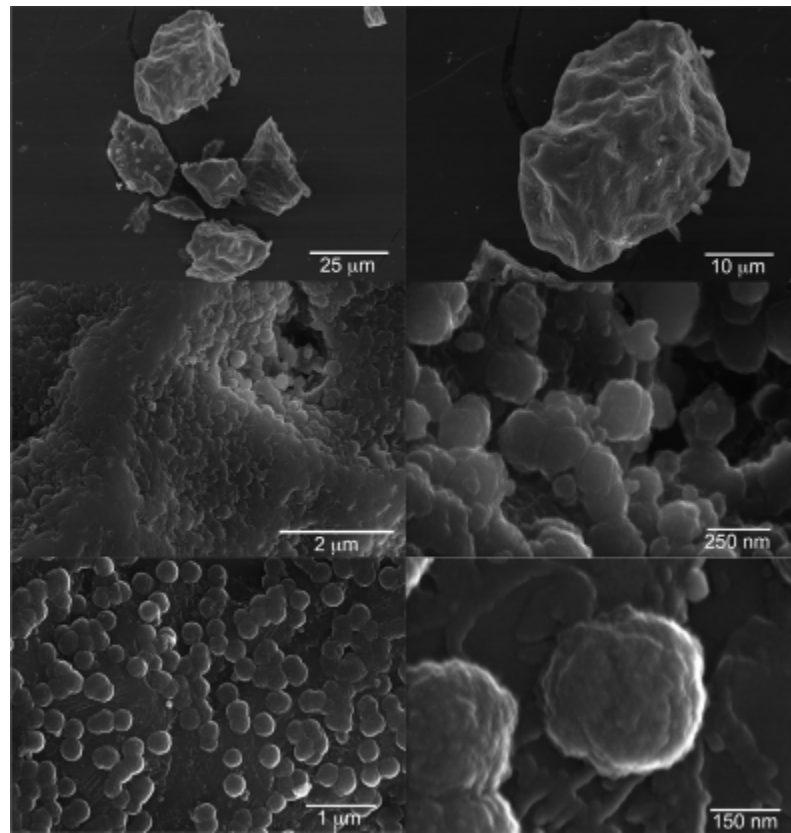

Fig. 3.1. SEM images of synthetic nanopowdered forsterite (cited from Anovitz et al., 2017).

The sample hydration was carried out by allowing nanopowders to equilibrate with pure H_2O vapor in a sealed chamber at 50 ºC for 20 hours (i.e., 0.123 bars H_2O vapor pressure). Then the sample was sealed and loaded in appropriate sample holders for neutron experiment right after the water equilibration step. The water content is measured to be 10.0% by weight using thermogravimetric analysis (TGA), which is assumed to be at full hydration level for the powdered samples.

3.3.2 Measurement

The QENS experiment was conducted at the disc-chopper spectrometer (DCS) (Copley and Cook, 2003) at NCNR at the NIST Center. DCS was operated at 12 Å incident wavelength in high flux mode with 10.9 μeV resolution (FWHM) at elastic line, and the allowed Q range was 0.046 Å^{-1} < Q < 0.98 Å^{-1}. The experimental spectra were fit using the equation shown below:

$$S(Q,\omega) = \left\{ A(Q)\delta(\omega) + [1 - A(Q)]\left[pL_1(\Gamma_1,\omega) + (1-p)L_2(\Gamma_2,\omega)\right] + \left[B_1 + B_2(Q,\omega)\right] \right\} \otimes R(Q,\omega)$$

Eqn (3.1)

The resolution function R(Q,ω) is convoluted with the elastic signal A(Q), two Lorentzian components $L_1(\Gamma_1,\omega)$ and $L_2(\Gamma_2,\omega)$ (p as the prefactor), and a linear background $B_1 + B_2(Q,\omega)$. The elastic signal derived from motions slower than the resolution of the instrument and weak scattering from the forsterite is modeled using a convoluted delta function ($\delta(\omega)$) centered on zero energy transfer. The quasi-elastic components, modeled by the convoluted Lorentzian functions, can be separated into a fast and slow component on the time scale of the instrument.

3.4 Results and discussion

The QENS spectra produced by DCS at four representative Q values are shown in Fig. 3.2. By fitting the experimental data (hollow circles) with functions shown in Eqn 3.1, parameters A, p, Γ_i (i = 1, 2) were obtained. Good quality fits were obtained in this manner as can be seen in Fig. 3.2. The red curves in Fig. 3.2 represent the overall fits.
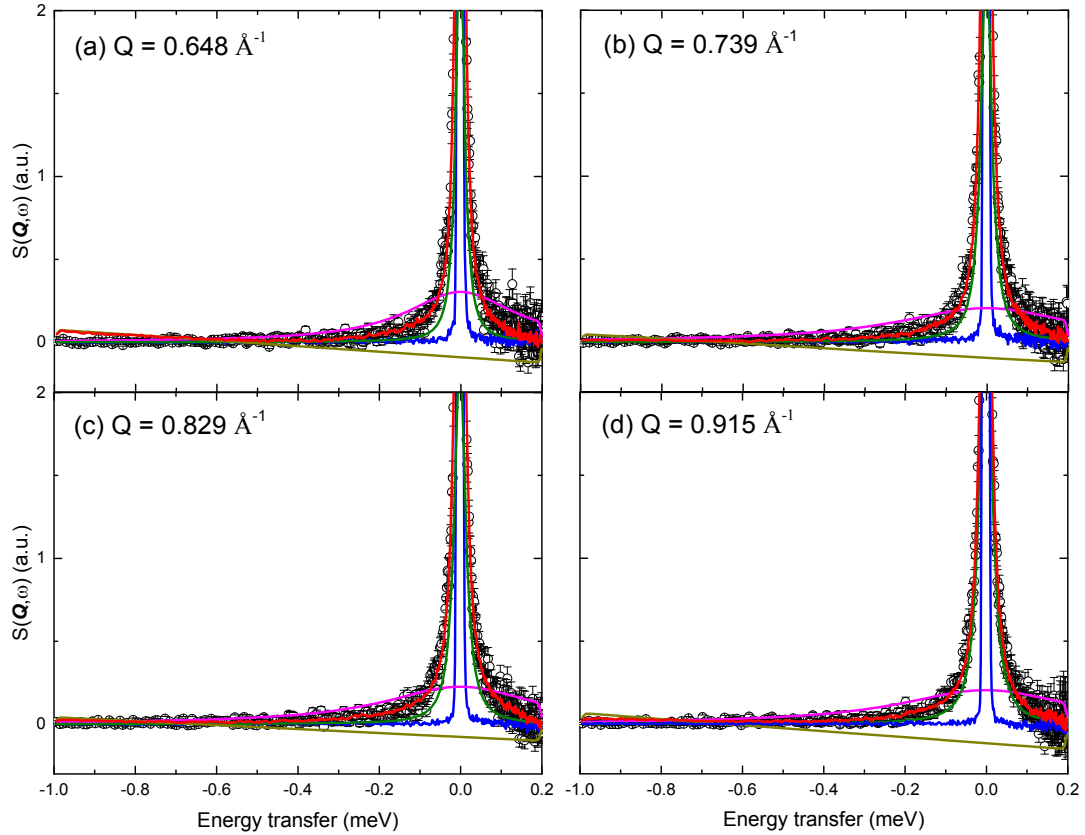
Fig. 3.2. QENS data (hollow circles) at four Q values (a ~ d) collected at DCS at 270 K. Fitting results are shown in different colored solid curves. Total fit function is shown in red; delta function in blue; two Lorentzian components, broad and narrow in magenta and green, respectively; and background in dark yellow.

QENS data in Fig. 3.2 show that different Q values result in different broadening, represented by Lorentzian components (in magenta and green), which corresponds to motions with different energies.

Fig. 3.3 is a snapshot of the 144 water molecules at equilibrium at 270 K, which was validated by the constant total energy and temperature of the system with time.
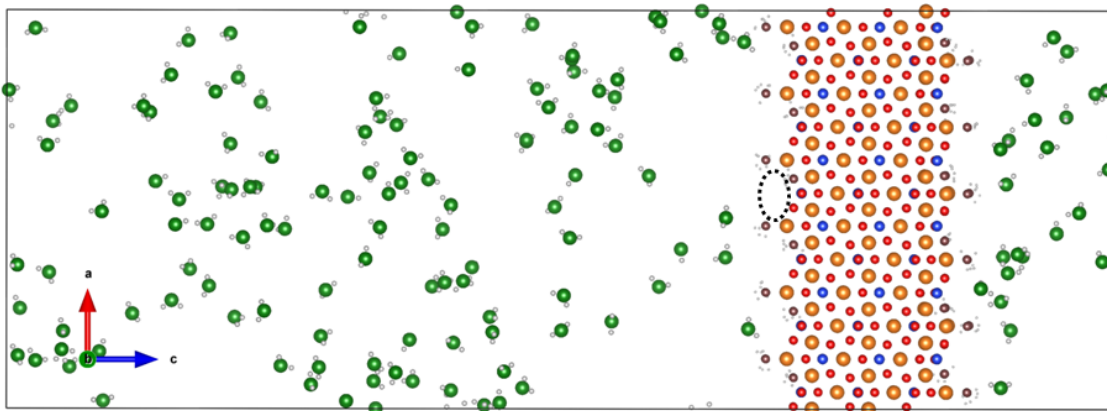
Fig. 3.3. A snapshot of water molecules on hydroxylated Fo(010) surface at 270 K. In forsterite slab, Mg=orange, Si=blue, O=red, O_{OH}=dark red, H_{OH}=grey. For water molecules, Ow=dark green, Hw=grey. The circled area with dashed line indicates a trough made by the hydroxyl ions on the surface where molecules may reside in. Only one such feature is highlighted for brevity.

The density profile of the molecules (center of mass) in a direction perpendicular to the Fo(010) surface is depicted in Fig. 3.4. X-axis starts from the center of the forsterite slab. There is a weak peak near the surface which can be due to the water molecules that become trapped into the surface hydroxyl troughs as shown in Fig. 3.3. Another major layer of water molecules is formed continuously above this layer. We designate the two layers as "adsorbed layer" and "first layer" henceforth, and the other water molecules as "free water".
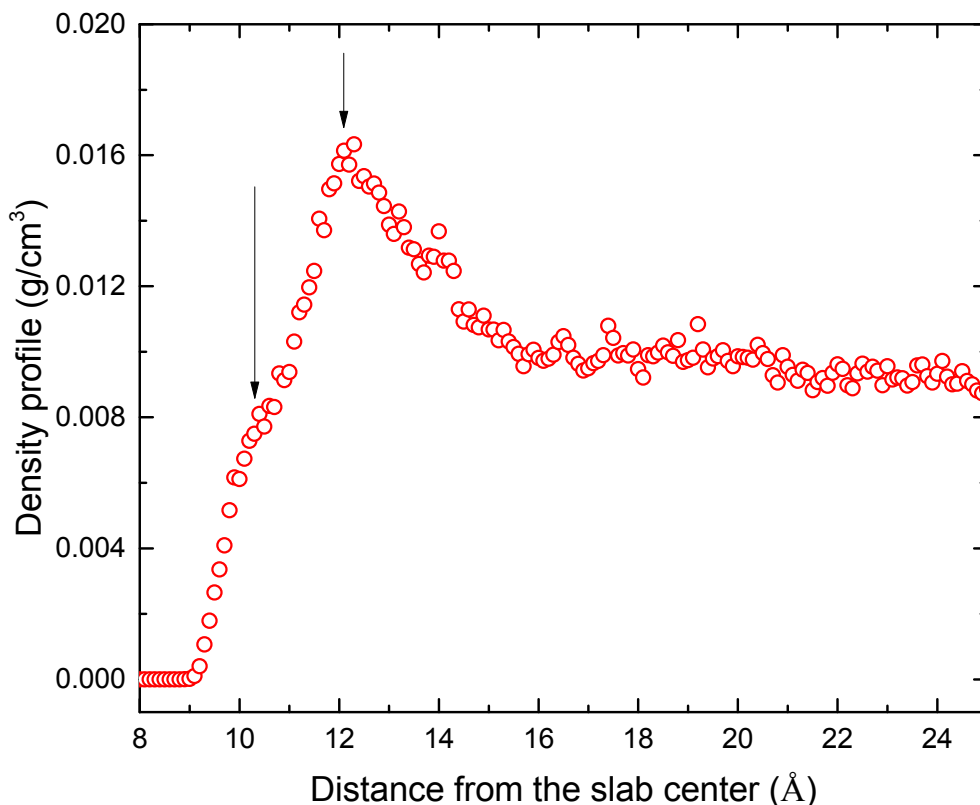
Fig. 3.4. Density profile (center of mass) of water molecules on the hydroxylated Fo(010) surface at 270 K. The arrows indicate the adsorbed layer centered at ~ 10.4 Å and first layer centered at ~ 12.1 Å.

We further examined the distribution of the water molecules on the surface throughout the 1.5 ns production time using a contour plot, as shown in Fig. 3.5. The results in Fig. 3.5 represent the total outcome of the two continuous layers that reside close to the surface. Fig. 3.5a represents the top view of the slab. The significant population region corresponds to the area surrounding the hydroxyl groups (Fig. 3.5b), whose binding energy is due to the hydrogen bonding between the OH group and a water molecule. In the trough regions created by the hydroxyl groups, the water molecule distribution is also apparent due to the existence of another OH group formed by an H atom and a surface oxygen atom.

57
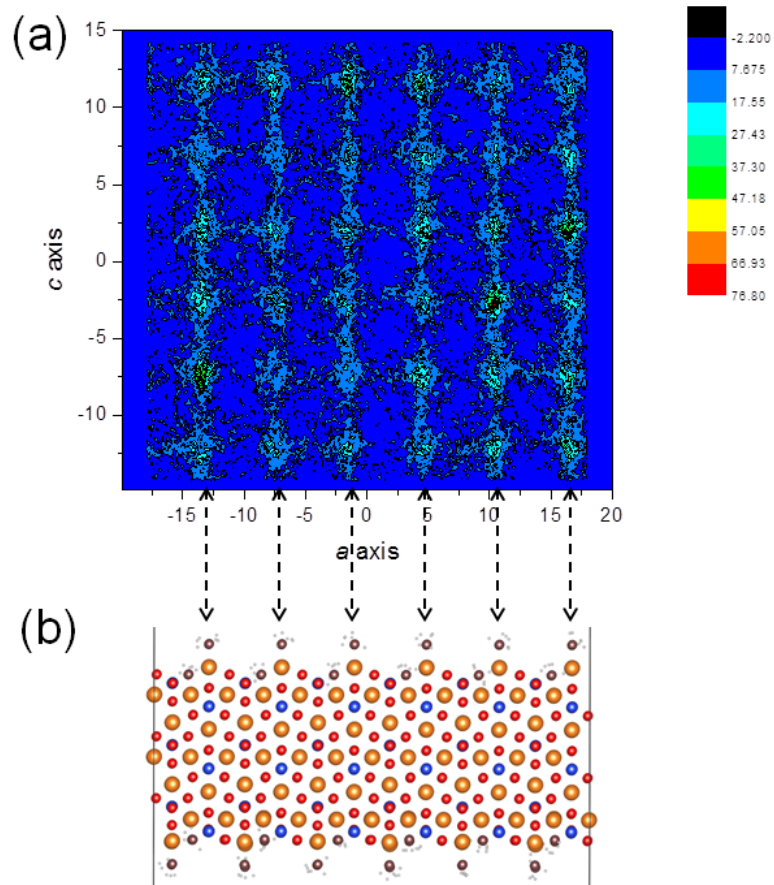
Fig. 3.5. Contour plot (a) of water molecule distribution on hydroxylated Fo(010) surface throughout 1.5 ns, top view. The slab (b) is used to identify the adsorption sites on the surface, side view.

3.4.2 Dynamics of the surface water

Dynamical properties can be divided into translation and rotation. The separation of the two types of motions can be facilitated by separating the coordinates in different frames of reference. For example, one can decompose the position vector of an interaction site in space fixed frame into the center of mass coordinates and the coordinates with respect to center of mass, such that:

$$r_0 = r_{CM} + d \qquad \qquad \text{Eqn (3.2)}$$

where r_0 represents the coordinates of an interaction site constituting the molecule in the space fixed frame of reference, r_{CM} represents the space fixed coordinates of the center of mass of the molecule, and d represents the coordinates of this interaction site in the center of mass frame. Their spatial relationship is described in Fig. 3.6 using water molecule as an example.

The translational motion can be obtained by analyzing the space fixed center of mass coordinates of the molecules (r_{CM}), and the rotational motion analysis uses the coordinates of the constituent sites in the center of mass frame (d).
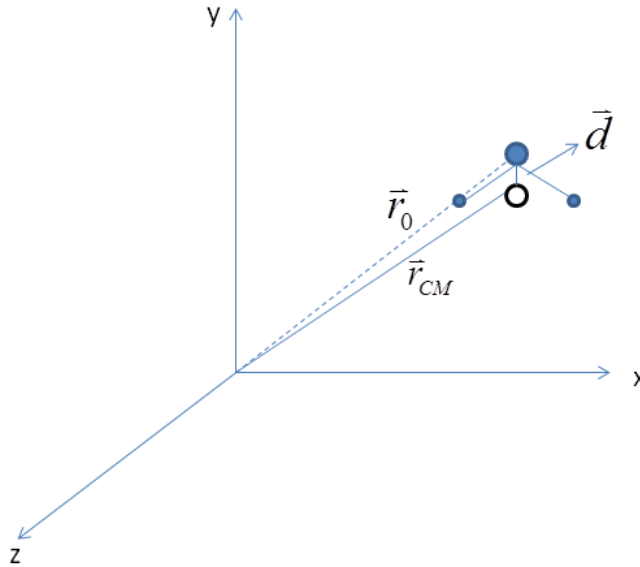
Fig. 3.6. The illustration of water molecule in fixed space, where r_0 represents the coordinates of Ow atom, and the black circle represents the center of mass of the molecule.

3.4.2.1 Translational intermediate scattering function (TISF)

Intermediate scattering function (ISF, $I(Q,t)$) is used to obtain the spatio-temporal information of the molecular motions. ISF is the spatial Fourier transforms of the Van-Hoove Self correlation function $G(r,t)$, which, in classical approximation, stands for the

probability of finding a molecule at position '**r**' and time 't' given that it was at origin at t = 0. The temporal Fourier transform of ISF is the dynamic structure factor S(**Q**,ω), which is the measured quantity in neutron scattering experiments. In an MD simulation, the ISF can be calculated as

$$I(Q,t) = \frac{1}{N}\sum_i \langle e^{iQ\cdot(r_i(t)-r_i(0))} \rangle \qquad \text{Eqn (3.3)}$$

where $\hbar Q$ is the momentum transfer, a quantity determined by the scattering angle in the experiment that has the dimension of inversed length, and *r* is the position vector of an interaction site in the simulation. The angular brackets denote an ensemble average and integrate the contribution from *Q*'s from all directions with the same magnitude. With the coordinates in the space fixed and center of mass frames of references, the molecular motion can be separated into translational and rotational components (see Eqn 3.2) (Gautam, 2017). The following translational intermediate scattering functions (TISF) were based on the trajectories of the space fixed coordinates of the center of mass of the molecules (i.e., r_{CM} shown in Eqn 3.2). Fig. 3.7 shows the calculated TISF functions from six *Q* values at 270 K. Here one should note that the DCS instrument, on which the QENS experiment was carried out was set to have an energy transfer window of -1 ~ +0.2 meV with a resolution of 10.9 μeV. This means that this instrument can detect motion in the time range of ~ 3 to 70 ps. We therefore studied the behavior of TISF up to 80 ps to ensure covering this range completely. The TISF curves exhibit several stages of decay with different rates: the decay is fast for up to ~ 1 ps, then the decay becomes slower after ~ 1 ps. The initial sub-picosecond fast decay is due to the ballistic motion of molecules before they encounter collisions with the neighboring molecules. The behavior

of TISF in this region is expected to have a Gaussian form (Egelstaff, 1967; Gautam et al., 2006). Within this time range, the behavior of the TISF can be expected to be similar to the inverse Fourier transform of the experimental spectra. As the spectral profiles were modeled with two Lorentzian functions, the TISF in this time range can be expected to exhibit exponential decay behavior.

Therefore, to model the TISF over the entire time range up to about 80 ps, a function composed of one Gaussian and two exponential functions is employed:

$$I(Q,t) = A_g e^{-(t/\tau_g)^2} + A_2 e^{-t/\tau_2} + A_3 e^{-t/\tau_3} \qquad \text{Eqn (3.4)}$$

where τ_g, τ_2, and τ_3 are the decay times that can represent different decay stages. Curves in Fig. 3.7 represent the fitting results of the calculated TISF data using Eqn 3.4. The exponential terms in Eqn 3.4 are the Fourier Transform of Lorentzian functions used to fit the spectral profiles obtained in QENS experiment, i.e.,

$$L_i(\Gamma, \omega) = \frac{1}{\pi} \frac{\Gamma_i}{\Gamma_i^2 + \omega^2} \ , (i = 1, 2) \qquad \text{Eqn (3.5)}$$
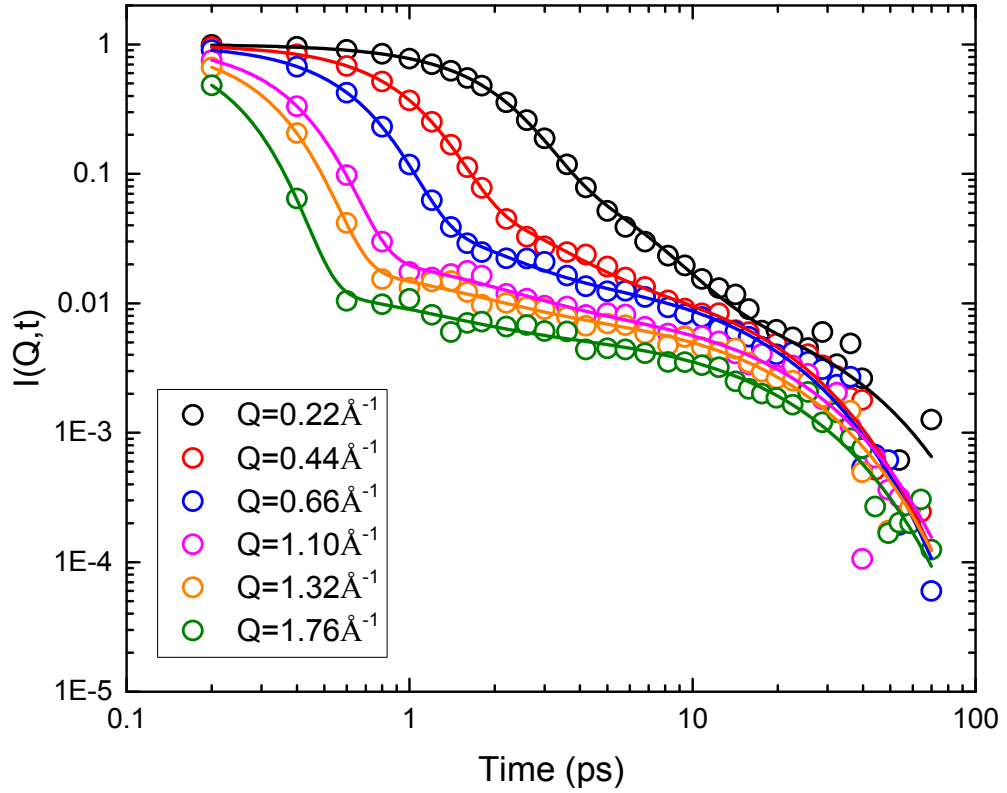
Fig. 3.7. Calculated TISF data using six Q values at 270 K. Circles are the calculated data selected by log time intervals. Lines are the fitting results using Eqn 3.4.

The decay constant τ determined by Eqn 3.4 can be converted to Γ in energy space to compare with QENS data. The energies (half width at half maximum, HWHM) corresponding to the decay time can be obtained by

$$\Gamma_i = \frac{\hbar}{\tau_i} \qquad \qquad \text{Eqn (3.6)}$$

Fig. 3.8 compares the Γ_i values obtained by fitting the experimental QENS spectra using Eqn 3.1 and those obtained from Eqn 3.6 by converting the decay constants of exponentials used to fit the TISF calculated from simulations (see Eqn 3.4). We can see the energies of the faster motion determined by simulation are higher than the QENS experimental data by a factor of two; while slow motion by a factor of two to five. This

overestimation is not uncommon, for example a shift of about a decade in time is found to be necessary to match the experimental and simulated data for polymeric systems (Capponi et al., 2009; Gautam et al., 2011). In addition, the discrepancy in using the ideal Fo(010) crystal planes in MD versus multiple crystal planes existing in nanopowdered forsterite in experiment, and the force field chosen could all contribute to the energy differences shown in Fig. 3.8. Due to the consistency of a factor of two variation between both components, we can claim that this comparison helps to qualitatively validate that the simulation work accessed to the real system and the further analysis based on the simulation can complement the QENS data.
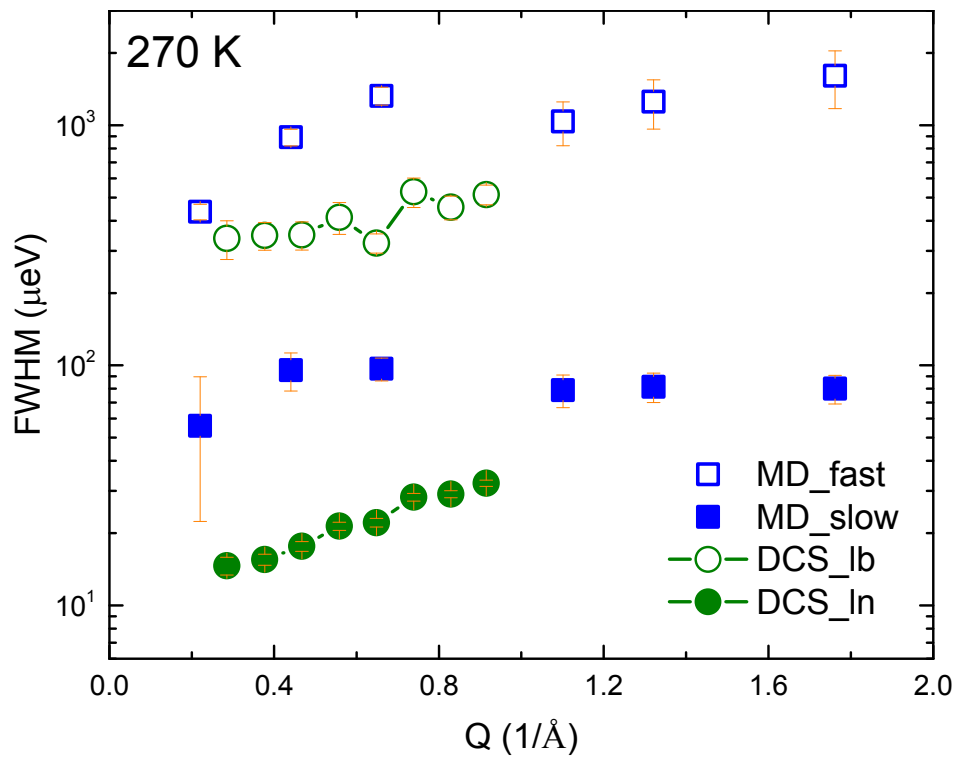
Fig. 3.8. Comparison of the QENS data with MD simulation data. The lb and ln stand for the broad and narrow components of Lorentzians used to fit the experimental data. The vertical lines are the error bars.

3.4.2.2 MSD

Mean square displacement (MSD) is used to describe the translational diffusive motion of molecules using their center of mass (COM) coordinates. A linear relationship with time indicates a diffusive motion; otherwise it means a non-diffusive motion. In Fig. 3.9, we employed planar MSD to assess the diffusion coefficient along the *a* and *c* lattice directions on the surface, which is more meaningful for examining the mobility on a flat surface. The planar MSD curves suggest a ballistic motion before 20 ps. After 20 ps, the molecules show diffusive motion.

The diffusion coefficient (*D*) determined from planar MSD is based on the Einstein relation:

$$D = \frac{MSD}{2n_d t} \qquad \text{Eqn (3.7)}$$

where n_d is the number of dimensions in space, which is equal to two for planar MSD. The *D* value is determined as 560.6×10^{-9} m^2/s.
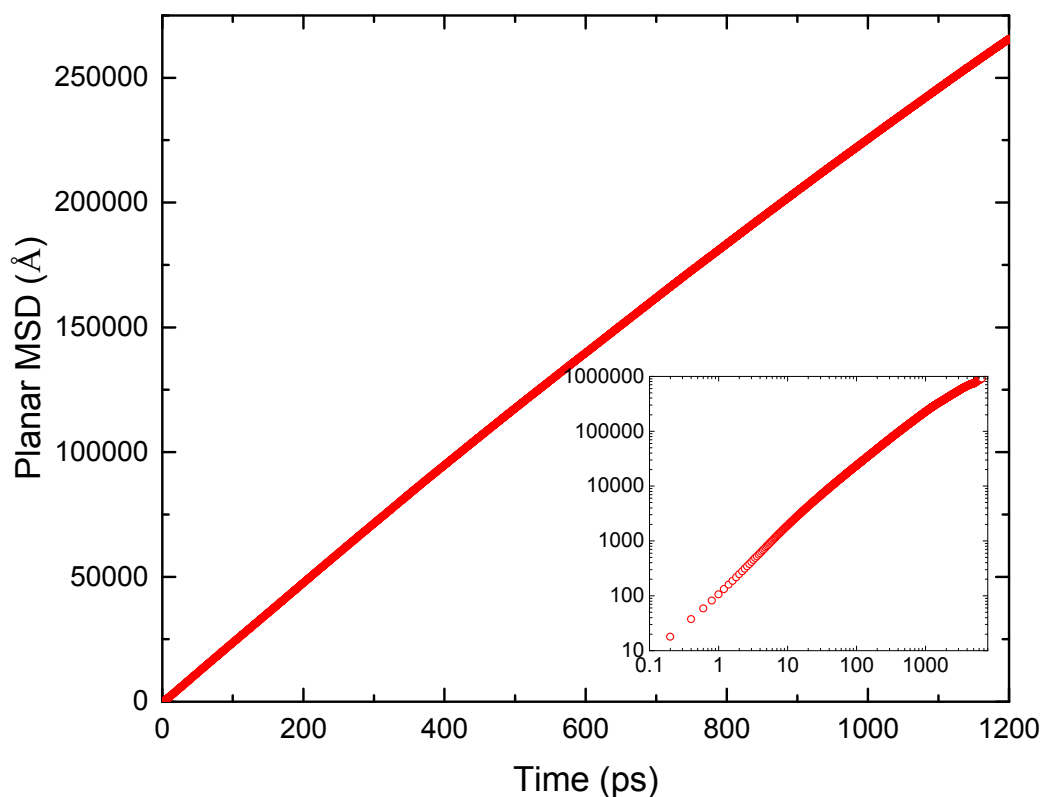
Fig. 3.9. Planar MSD of 144 water molecules. The inset shows the full picture, while the first 1200 ps is shown to visualize the translational diffusion behavior.

The interfacial effect caused by the solid surface for molecules/fluids can be much weaker than pore environments, such as in natural slit pores (clay minerals, zeolites), and in some other porous materials. According to MD simulations, Wang and co-workers (Wang et al., 2005; Wang et al., 2006) have calculated the planar diffusion coefficients of water in the interlayer space of different phyllosilicate structures (brucite, gibbsite, hydrotalcite, muscovite, and talc) at 300 K, which is $(3.0 \sim 4.0) \times 10^{-9}$ m^2/s, greater than the total diffusion coefficient from three directions. Greathouse and co-workers (Greathouse et al., 2015) also calculated the lateral diffusion coefficient of water in the interlayers of Na-hectorite and Na-montmorillonite at 298 K, obtaining the value of $(1.4 \sim 2.1) \times 10^{-9}$ m^2/s for water in either the first monolayer or second monolayer. The self-

diffusion coefficient of bulk water is determined to be 2.3×10^{-9} m^2/s (Krynicki et al., 1978). In sheeted graphite with the interlayer space of, for example, 7 Å, which is a hydrophobic material, the water diffusion coefficient is determined to be 7×10^{-13} m^2/s at 298 K (Hirunsit and Balbuena, 2007). Compared to the D value of water on mineral's surface in this study, we observe that the dynamics of the confined fluids in narrow space (a few angstrom) is subjected to a severe hinderance. However, it is noted that the dynamics of confined fluids are also associated with the concentration of the fluids, ambient conditions, and confining media. For example, Lee and Rossky (Lee and Rossky, 1994) placed water with the density of 0.9963 g/cm^3 at 25°C on three type of surfaces, i.e., a flat hydrophobic surface, a rough hydrophobic surface, and a hydrophilic silica surface, and obtained the water diffusion coefficients of $\sim 3.5 \times 10^{-9}$ m^2/s, $\sim 2.7 \times 10^{-9}$ m^2/s, $\sim 0.96 \times 10^{-9}$ m^2/s, respectively. The mobility is much lower than the water molecules in this study due to their higher water density.

To study the behavior of water molecules residing in different layers defined by Fig. 3.4, we selected representative molecules that resided in a given layer for at least 15 ps. The corresponding 15 ps trajectories were analyzed further to obtain dynamical behavior in different layers. These trajectories and corresponding MSD can be found in Figs. B2 and B3 in Appendix B.

3.4.2.3 Rotational properties

Rotational motion can be studied by using the coordinates of an interaction site in the center of mass frame (refer to Fig. 3.6). The evolution of the position vector of Ow site in the center of mass frame was used to obtain the rotational properties.

3.4.2.3.1 Orientational autocorrelation function (OACF)

We use a unit vector ($\boldsymbol{u}$) along the position vector of Ow site in the center of mass frame. Dipole correlation function is in the form of the first rank component (Eqn 3.8) of the general Legendre polynomials. We can calculate the dipole autocorrelation function $C_R(t)$ corresponding to the rotational motion using

$$C_R(t) = \left\langle \vec{u}(t) \cdot \vec{u}(0) \right\rangle \qquad \text{Eqn (3.8)}$$

which can also be measured in dielectric relaxation spectroscopy. The general Legendre polynomials can be expressed as

$$C_l(t) = \left\langle P_l[\vec{u}(t) \cdot \vec{u}(0)] \right\rangle \qquad \text{Eqn (3.9)}$$

where the $P_l(x)$ is the Legendre's polynomial of order l (0, 1, 2, ...). The second rank component can be measured in light scattering and NMR experiment. Fig. 3.10 below shows the first four rank components in total.
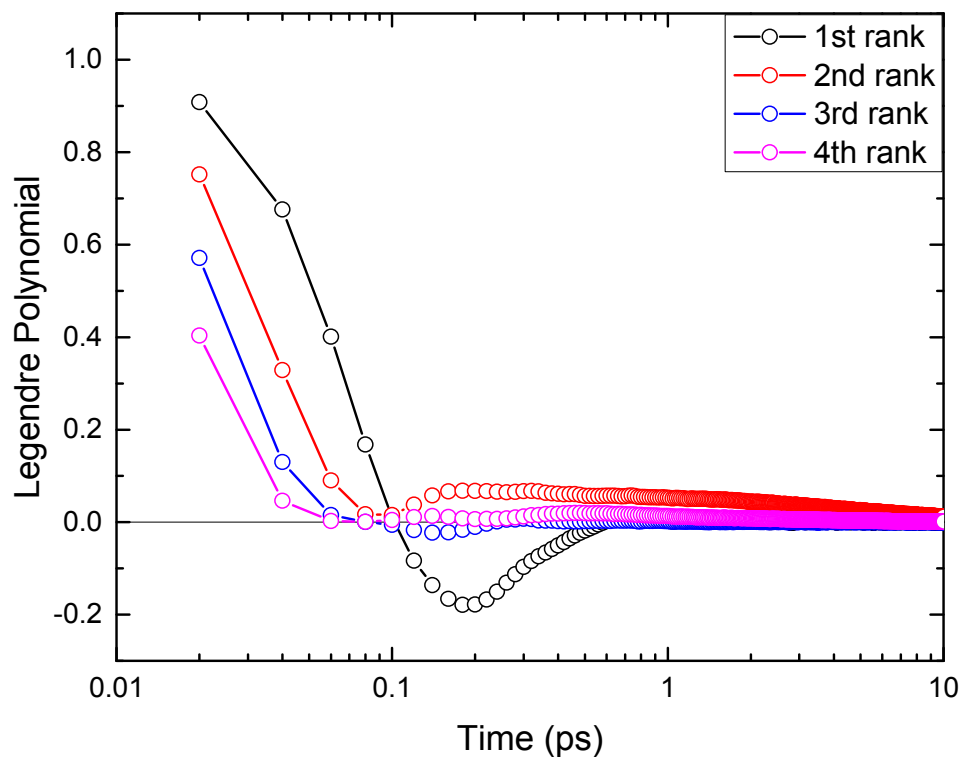
Fig. 3.10. First four ranks of Legendre polynomial series for 144 molecules at 270 K. Dipole autocorrelation function is shown in black.

The dipole correlation function is expected to show an exponential decay that describes the diffusive rotational motion. In the present case we see that the dipole correlation function (in black) shows a fast decay behavior within the first 0.1 ps. After that, we can see a significant negative region on the dipole autocorrelation curve, which suggests a large angular jump. According to the value at the lowest point, the average angle of rotation jump is 100.3˚. This large angle of rotation is expected as water molecule can rotate easily due to most of its mass being associated with Ow atom.

The time scale of the rotational motion can be derived by integrating the $C_l(t)$ function to obtain the rotational correlation time τ_l:

$$\tau_l = \int_0^\infty C_l(t)dt \qquad\qquad \text{Eqn (3.10)}$$

Using 100 ps as the upper limit as all the four curves approach to zero at the time, the rotational correlation time τ_l for the first rank (τ_1) is 0.03 ps, corresponding to an energy of 21.9 meV. Taking this approach further, we obtained the values of τ_2, τ_3, and τ_4 as 0.43 ps (1.5 meV), 0.03 ps (21.9 meV), and 0.07 ps (9.4 meV), respectively.

3.4.2.3.2 Rotational ISF

Rotational ISF (RISF) represents the temporal and spatial information of rotational motion. Fig. 3.11 shows the RISF curves for eight Q values at 270 K. The constant values at later time stage are equal to the elastic incoherent structure factor (EISF), a quantity that can be measured in a QENS experiment. Instead of coordinates of interaction site in the center of mass frame (d), a unit vector u is used here to produce the RISF curves. We note that the EISF obtained from the RISF represent rotational motion alone and thus is different from the EISF values obtained from the QENS experiment described here. The experimental EISF values described here arise from the elastic contribution from rotation as well as restricted translational motion of molecules, and any molecules that might be stationary on the time scales accessible to the instrument. Therefore, we denote the EISF obtained from RISF as rEISF when referring to simulation results.
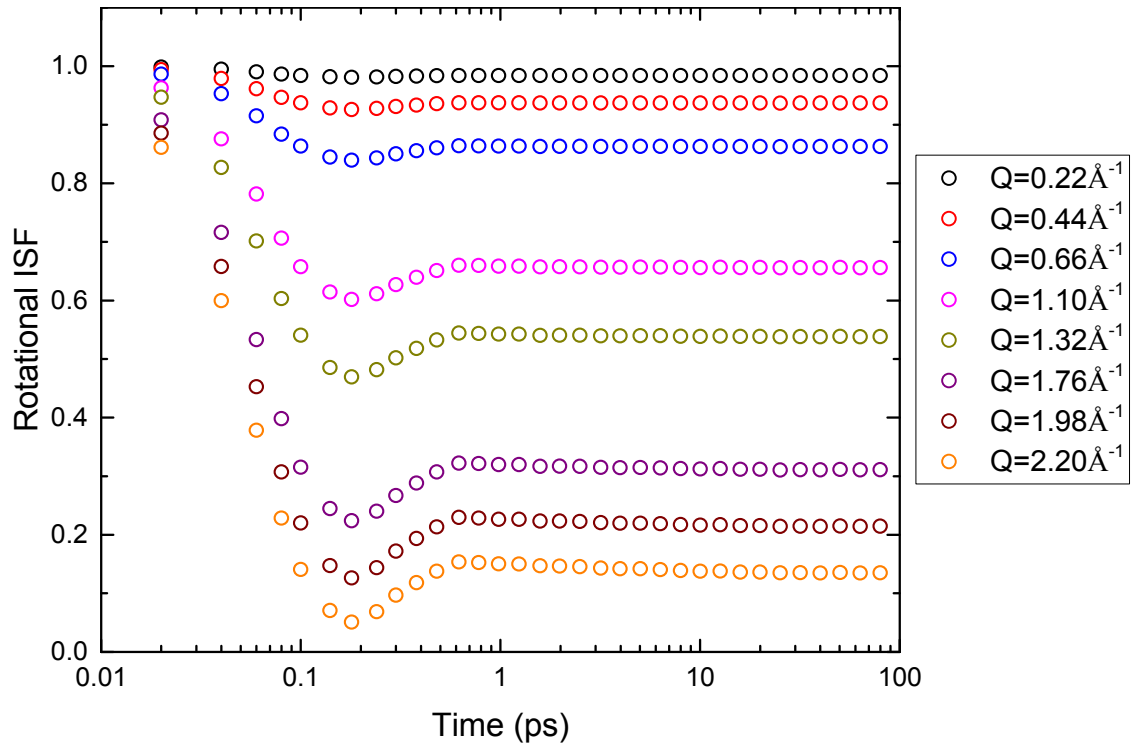
Fig. 3.11. Calculated rotational ISF data for eight Q values at 270 K.

As seen in Fig. 3.11, the RISF curves first undergo a fast decay to a minimum and an increase again. After ~ 1 ps, the curves begin to decay slowly. The two stages of decay indicate different time scales within the rotational motion, which was also observed for water molecules in the interlayer of clay minerals (Michot et al., 2007). The very fast rotational motion below 1 ps would correspond to a quasi-elastic width of ~ 1 meV, which would appear as a flat background for DCS instrument (refer to the DCS spectra in Fig. 3.2). While for the slower rotational motion after ~ 1 ps, the very slow decay corresponds to a quasi-elastic width of < 10 μeV, which would not be resolved by DCS instrument either. Therefore, only the translational motion contributes to the QENS data

and thus the two Lorentzians used to fit the QENS data represent translational motion of water molecules at two different time scales.

The variation of the rEISF values with Q provides the geometry information of the rotational motion. Thus we plotted the rEISF values vs Q in Fig. 3.12a. For the isotropic rotational function:

$$rEISF = \left[\frac{\sin(r \cdot Q)}{r \cdot Q} \right]^2 \qquad \text{Eqn (3.11)}$$

r is the radius of gyration of the molecule. A good fitting result is shown in Fig. 3.12a. The r value in Eqn 3.11 is determined as 1 Å as the fitting result, the length of a unit vector in the RISF calculation. In Fig. 3.12b, we show the trajectory of one Ow atom in COM frame. It can be seen that this trajectory spans a fully formed sphere. This would happen if the motion is isotropic. A shorter time length is used here to properly demonstrate the isotropic rotation, as motion during a longer time would always lead to the trajectory spanning a complete sphere. This isotropic nature of rotation is to be expected as the orientational distribution function of water molecules shows no preferred orientation, as shown in Fig. B3 in Appendix B.
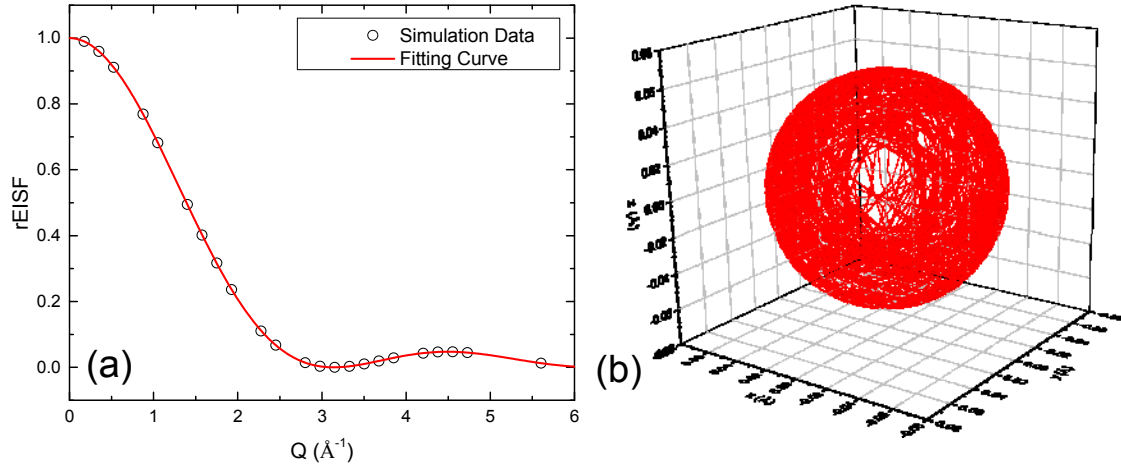
Fig. 3.12. (a) Calculated rEISF curves as a function of Q values, along with a fitting result, (b) trajectories of 100 ps for one Ow atom in COM frame, which represents the rotational motion.

3.4.2.3.3 Motions of flexible H atoms

The hydroxylated Fo(010) surface is decorated with H and OH groups in simulation, and H atoms were kept mobile, thus it is necessary to examine if H atom motions contributes to the QENS spectra. To do this, intermediate scattering functions for hydrogen atoms (ISF_H) were calculated by using the position vector of H atoms with respect to the oxygen atoms to which they are bonded (refer to Eqn 3.3). Fig. 3.13 displays the calculated ISF_H data for all H atoms on the surface for four Q values. Similar to the calculated RISF for water molecules (Fig. 3.11), the calculated ISF_H data for H atoms do not decay to zero, as the H atoms binding with oxygen atoms only exhibit local motions. Similarly, two different time scales can be observed in Fig. 3.13. The initial very fast decay is followed by a rebounce up to ~ 0.3 ps, corresponding to ~ 2 meV which is too large to be detected by DCS instrument. A much slower decay exists beyond ~ 1 ps. We fitted the curves beyond ~1 ps using one exponential function, and the energy

corresponding to this slow decay is in the range of $10^{-2} \sim 10^{-1}$ μeV, which is out of the resolution of DCS instrument. Thus, simulation data suggests that contribution to the DCS spectra from both rotational motion of water and motion of H atoms on the forsterite surface can be excluded. The only contribution to the DCS spectra comes from translational motion of water molecules alone.

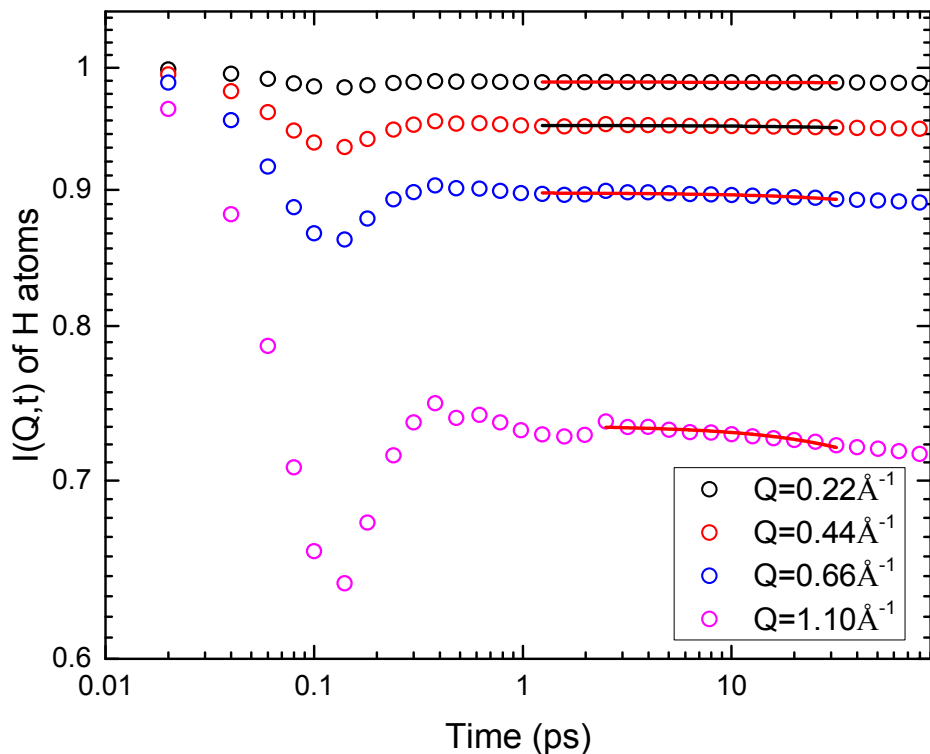Fig. 3.13. Calculated ISF data for H atoms on the hydroxylated Fo(010) surface. The curves are the fitted results using one exponential decay function for the second decay stage.

3.5. Conclusions

This study examined structure and dynamics of water on a hydroxylated forsterite surface at 270 K using MD simulations, which provided a complementary tool for the QENS experiment. The MD work first demonstrated how water resides on the

hydroxylated surface. The density profile of water normal to the Fo(010) surface is composed of a weak first layer that represents water molecules that are trapped in the trough surrounded by the hydroxyl groups and a strong layer on top of the first layer. A contour plot also identifies the preferred adsorption sites on the surface, i.e., the areas near the H and OH groups. Regarding the dynamic properties, the translational and rotational motions were investigated using the coordinates in different frames by calculating the TISF and RISF. The calculated translational motions are qualitatively comparable with the fast and slow components determined by QENS experiment using the NIST DCS instrument. The simulation data show that the rotational motion of water molecules and the motions of the flexible hydrogen atoms on the surface are either too fast or too slow to contribute to the QENS spectra. MD simulations further show that the rotational motion of water molecules is isotropic. The diffusion coefficient determined by the MSD shows that the confining effect by solid surface is much less restricted than slit pores. Above all, simulation tool provides wide and complementary information for the understanding of structure and dynamics of water on forsterite surface, using experimental data as support.

Chapter 4: Vibrational Behavior of Water Adsorbed on Forsterite (Mg_2SiO_4) Surfaces

4.1 Introduction

In addition to the energetics, structure and stochastic dynamics of water adsorption on forsterite that have been measured or simulated, the vibrational properties of the system need further investigation to complement our understanding of the interfacial behavior of water molecules. Inelastic neutron scattering (INS) has been the most ideal tool to characterize the mineral interface with hydrogen-bearing fluids due to the large cross section of incoherent scattering of H atoms. The neutron vibrational signal increases with the amplitude of motion of hydrogen, so that translations and librations (large amplitude motions) usually dominate the neutron vibrational spectrum. Spencer and co-workers have conducted a series of INS experiments to focus on the vibrational behavior of water on the nanoparticles of metal oxides, including rutile (TiO_2) (Spencer et al., 2009), cassiterite (SnO_2) (Spencer et al., 2011), γ-alumina (γ-Al_2O_3) (Spencer, Huang, et al., 2013), PdO (Spencer et al., 2012), CuO, ZnO, and CeO_2 (Spencer, Ross, et al., 2013). They found the vibrational behavior and heat capacities of the surface water (associated or dissociated H_2O) are greatly influenced by the water concentration and solid surface speciation. The combination of INS experiment and MD simulations for surface water vibration was performed on SnO_2 nanoparticles (H.-W. Wang et al., 2014) to consistently describe the different hydration levels on the (110) surface, where H-bonds played a key role modifying the structure and dynamics of the interfacial water.

To fully characterize the vibrational behavior of water on the forsterite surface, we utilized INS technique coupled with MD simulations in this study.

4.2 Experiment

Neutron scattering is an intensity limited technique. Nanoparticles of forsterite were synthesized to provide a large enough surface area so as to adsorb an amount of water providing a strong enough neutron scattering signal. A total 3.527 gram of sample with a specific surface area of 25.0 m^2/g (as measured by nitrogen adsorption at 77 K; BET method) was used in our studies. The sample was synthesized by a sol-gel method as described in Anovitz et al. (2017). Briefly, magnesium ethoxide and tetraethylorthosilicate (TEOS) were dissolved in a hot mixture of toluene and methanol. Sodium hydroxide was added to hydrolyze TEOS and the solution was refluxed for 12 hours. The resulting gel was calcined at 800^oC under nitrogen for 4 hours. The sample was then washed with warm water and dried on the rotary evaporator. This last step is significant for what follows in that the forsterite surface most likely was in its natural hydration state when the neutron scattering measurements were performed. Our characterization tools of the nanoparticle forsterite included XRD, SEM, TEM and surface area analysis (images are provided in Appendix C).

The INS experiment was performed at the Manuel Lujan, Jr. Neutron Scattering Center at Los Alamos National Laboratory. The Filter Difference Spectrometer (FDS) was used for all our measurements. The Lujan Center operates a pulsed neutron source at an average proton beam power of 80 kW. FDS measures the initial energy of neutrons by time of flight, whereas the final energy of the neutrons is fixed at 5.2 meV by a series of

cooled polycrystalline beryllium filters between the sample and the detector banks. It is an indirect geometry instrument (the sample is illuminated by the white beam from the ambient water moderator).

The nanopowdered forsterite sample was dried briefly (1 hour) at 150°C in vacuum oven before being placed in an annular aluminum sample can in a helium atmosphere provided by a dry box. The distribution of the sample was covered by the beam cross section (2 cm × 10 cm). The sample was cooled to 10 K in a top-loading closed-cycle refrigerator over the course of two hours, at which time data collection was started. For water addition, the sample was warmed to room temperature. The desired amount of water vapor was condensed on the sample, which was subsequently returned to FDS for additional measurements. The sequence of measurements is as follows: (S1) Sample as synthesized. Note that the sample after calcination was washed with water and dried on a rotary evaporator. This operation most likely left the surface covered with water. The sample was subsequently dried at 150^oC in vacuum oven. This operation most likely removed loosely bound water but some water remained tightly bound to the forsterite surface (as will be explained below); (S2) Adsorb 25 μL of water on the previous sample. This amount was chosen on an empirical basis of one water molecule occupying 10.6 Å^2 (McClellan and Harnsberger, 1967); (S3) Adsorb another 25 μL of water to add a second monolayer; (S4) Dehydrate the sample in step (S3) at 150°C in vacuum oven for 24 hours. This treatment is expected to remove most of the water tightly bound to the surface after synthesis. Our water concentration for one monolayer is consistent with the previous experimental findings (Thompson et al., 2014).

4.3 MD simulations

Molecular dynamics (MD) simulations were performed using DL_POLY software package (Todorov et al., 2006). Among the common crystal planes of olivine minerals, the (010) surface has a lower surface energy, and is selected in this study for water adsorption.

The simulation box in this study is composed of a forsterite (*Pbnm* space group, *a* = 4.753 Å, *b* = 10.199 Å, *c* = 5.981 Å, based on experimental unit cell determined by Lager et al. (1981)) slab with a unit cell replicated 6 × 1.5 × 6 times, and an additional free space with a length of ~ 85 Å along the **b** axis to allow water molecules to move. The two (010) surface sides are cleaved to be non-dipolar and are terminated with the intact Si-O tetrahedron (both sides have the same atomic arrangements and chemistry). The length of the free space for water molecules (~ 85 Å) were selected to facilitate the observation of surface interfacial effects, rather than both surface and pore confinements that would be observed if a smaller free space between slabs was used in the periodic boundary condition. One Mg atom on Fo(010) surface could accommodate two water molecules as one monolayer (1ML), a definition used in Kerisit et al. (2013). Accordingly, the total number of water molecules on the surface is 144, which satisfies 1ML water adsorption on both sides of the slab. This coverage is equivalent to 7.1 H_2O/nm^2.

Kerisit et al. (2012) examined supercritical CO_2/H_2O on the forsterite bare and hydroxylated (010) surfaces at the condition of 50˚C and 180 atm. Potential parameters of forsterite in the present work follows Kerisit et al. (2013) that used modified CLAYFF

model (Cygan et al., 2004) and Lennard-Jones interactions. The interaction between Mg and water (Ow) is described by Buckingham potentials, which have been used in a number of MgO/water and Fo/water MD studies (de Leeuw and Parker, 1998; de Leeuw et al., 2000; King et al., 2010; Kerisit et al., 2012). The charge in forsterite follows Kerisit et al. (2012) that is modified from CLAYFF model, where Mg=+2.0 e, Si=+2.1 e, O=-1.525 e to keep the system charge neutral. The flexible model for water (Toukan and Rahman, 1985) was used in this study, for the consideration of deriving intramolecular vibrational properties. The model is a modified version of SPC model (Berendsen et al., 1987) using harmonic interactions.

The Mg, Si, and O atoms in the forsterite slab were kept immobile throughout calculations. We created two stages to obtain the vibrational spectra of the water. Simulations were consecutively conducted at 298 K, 250K, 200 K, 150 K, 100 K, 50 K and 10 K, respectively, with NVT ensemble using Nosé-Hoover thermostat as the first stage to obtain the equilibrium state. The Velocity Verlet (VV) algorithm was used to advance the atom positions. Time step was 1 fs for each step of movement. The equilibrium time for each temperature lasts for 4.0 ns which proved to be sufficient by examining the total energy and temperature consistency throughout this time period. Each initial configuration at temperatures lower than 298 K utilized the final equilibrium configuration from the last temperature step. The second stage was to run after the equilibrium state in a shorter time step in order not to exceed its vibration time scale using NVE ensemble. The NVT ensemble is not suitable for vibrational simulations, as the thermostat frequency can interfere with the vibration (de Koker, 2009). Time step was

0.2 fs for each temperature, and 40 ps was used to generate the equilibrium and another subsequent 60 ps was the production time. The results of 150 K will be reported here to compare with INS experiment. Results for the 298, 50, and 10 K can be found in Appendix C. We note here that the thermal de-Broglie wavelength of water at 298, 150, 50 and 10 K are, respectively 0.24, 0.33, 0.58 and 1.3 Å. This means that classical treatment of water dynamics gets progressively inaccurate at lower temperatures. The quantum effects are negligible at 298 K, but are significant below 150 K. At 298 K, however, the vibrational spectrum exhibits considerable broadening due to high contribution from slower stochastic dynamics. Some vibrational features that remain unresolved at 298 K appear at 150 K. Thus 150 K data represents the best resolution of vibrational features with the best accuracy that classical mechanics can provide at lower temperatures. We therefore chose the 150 K simulation data to compare with the experimental data and further analyze the structural and dynamical properties.

4.4 Results and discussion

4.4.1 INS experiment

Given the geometric arrangement of the beryllium filters, the vibrational spectrum is automatically averaged over a momentum transfer range of about 1.5 to 17 Å^{-1}. A spectrum is collected between 50 and 4000 cm^{-1} with a resolution varying between 2 and 5%, depending on the data analysis method used. Our data were processed by straight numerical deconvolution of the instrument resolution function (Sivia et al., 1990).

Multiple crystal planes are exposed for the forsterite nanoparticles. Based on the computational study, (110) and (010) surfaces yield the highest (2.18 J/m^2) and lowest

surface energies (1.22 J/m^2) (Bruno et al., 2014). As a result, the surface of forsterite is most likely partially hydroxylated after exposure to water, and, therefore has some hydrophilic character. It follows that some water tightly bound to hydroxyl groups and to the surface most likely remains as the state described in S1. Temperatures in excess of hundreds of Celsius degree or prolonged heating in vacuum at lower temperatures is necessary to remove this surface water layer (Finnie et al., 2001) which is the operation described in S4.

Spectrum data have been treated in two ways, taking sample either from S1 or from S4 as the solid blank. The following water layer structures can be obtained (Table 4.1). The partial hydration/hydroxylation layer (S1-S4) and one monolayer scenarios (S2-S1) will be addressed here, and the other scenarios are referred to Appendix C.

Table 4.1. Water layer structures obtained in INS experiment.

Data treatment	Water layers
S1 - S4	Partial hydration/hydroxylation
S2 - S4	One monolayer + Partial hydration/hydroxylation
S3 - S4	Two monolayers + Partial hydration/hydroxylation (see in Appendix C)
S2 - S1	One monolayer
S3 - S1	Two monolayers (see in Appendix C)

The existence of the partial hydration/hydroxylation layer is shown in Fig. 4.1. The difference spectrum, S1-S4, removes the contribution from the forsterite lattice. The difference shows very clearly an intense, residual water librational signal in the range from 400 to 1200 cm^{-1}. Remarkably the peaks at 525, 720, and 1005 cm^{-1} are quite sharp. Librations occur at finite frequencies because of the restoring forces provided by the molecular environment, usually hydrogen bonding to other water molecules. If these

forces are spatially diffuse or fluctuate greatly in time, the librational modes broaden considerably. Water hydrogen-bonded to itself thus tends to produce very broad librational modes that overlap and merge into an almost featureless broad band (see Fig. C5 in the Appendix C). Water films on titania (rutile or anatase) show similar broad features (Levchenko et al., 2007; Spencer et al., 2009). The sharpness of the librational modes in our sample most likely reflects a strong interaction of relatively isolated water molecules with well-defined isolated sites on the forsterite surface rather than with each other. Since the water molecules interact essentially with a well-defined site on the surface, the amplitude of motion is large and the neutron signal is strong. However, the interaction sites for partial hydration/hydroxylation on the real sample from the experimental perspective are difficult to assess as they could occur with magnesium cations, oxygen atoms, vacancies, hydroxyl groups, or surface defects.
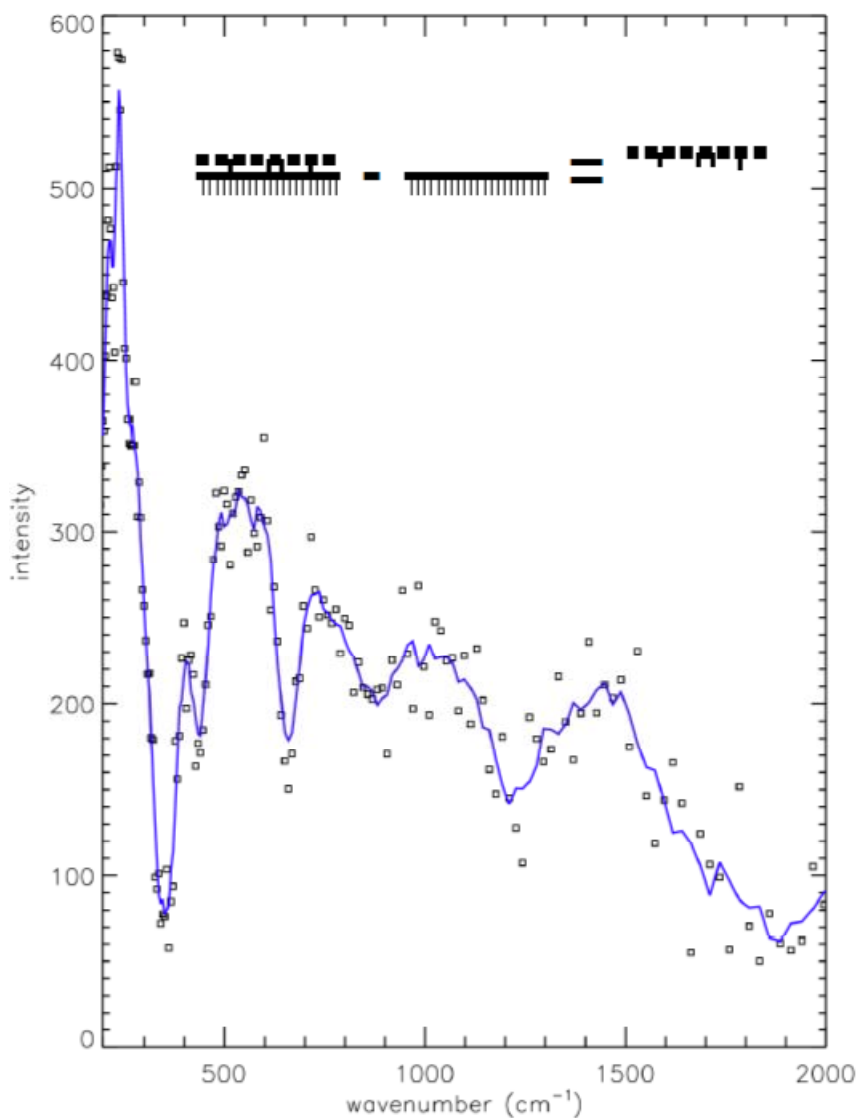
Fig. 4.1. Difference spectrum between S1 and S4. The solid line is a smoothed version of the data (boxcar algorithm, 4 points). The broad band around 1400 cm^{-1} is the water bending mode, and probably includes a contribution from the bending of hydroxyls at the surface. Intensity is in arbitrary units. The symbolic representation are used for producing schematic representations of the various difference spectra.

In the hydration procedure of S2, the water of one monolayer (1ML) was delivered on top of the incomplete water layer in S1. We have the choice to consider the difference S2 - S1 or S2 - S4. The first difference, S2-S1, would remove the signals from bulk forsterite and from the incomplete layer of water discussed in the paragraph above. The second scenario would remove only bulk forsterite, thereby giving a signal which is the sum of the incomplete surface layer and the 1ML of water adsorbed on top of it (see in Table 4.1). The INS spectra of these differences are shown in Fig. 4.2. The top curve is S2 - S1. It shows a relatively featureless librational band as might be expected for water hydrogen-bonded to itself. The first monolayer of water adsorbed on the "natural" hydration layer present in S1 is essentially a continuous, disordered layer similar to liquid water. The bottom curve is S2 - S4. In this case only the contribution from forsterite is removed from the spectrum of S2. We should see a signal which is the superposition of the partial film in S1 and the disordered monolayer just discussed. Indeed the peaks at 535 and 725 cm^{-1} are to be attributed to the peaks at 525 and 720 cm^{-1} mentioned above. The broad librational band of the adsorbed monolayer just adds onto this signal as a featureless background. The frequency shifts are possibly due to the (weak) interaction of the partial layer with the monolayer.
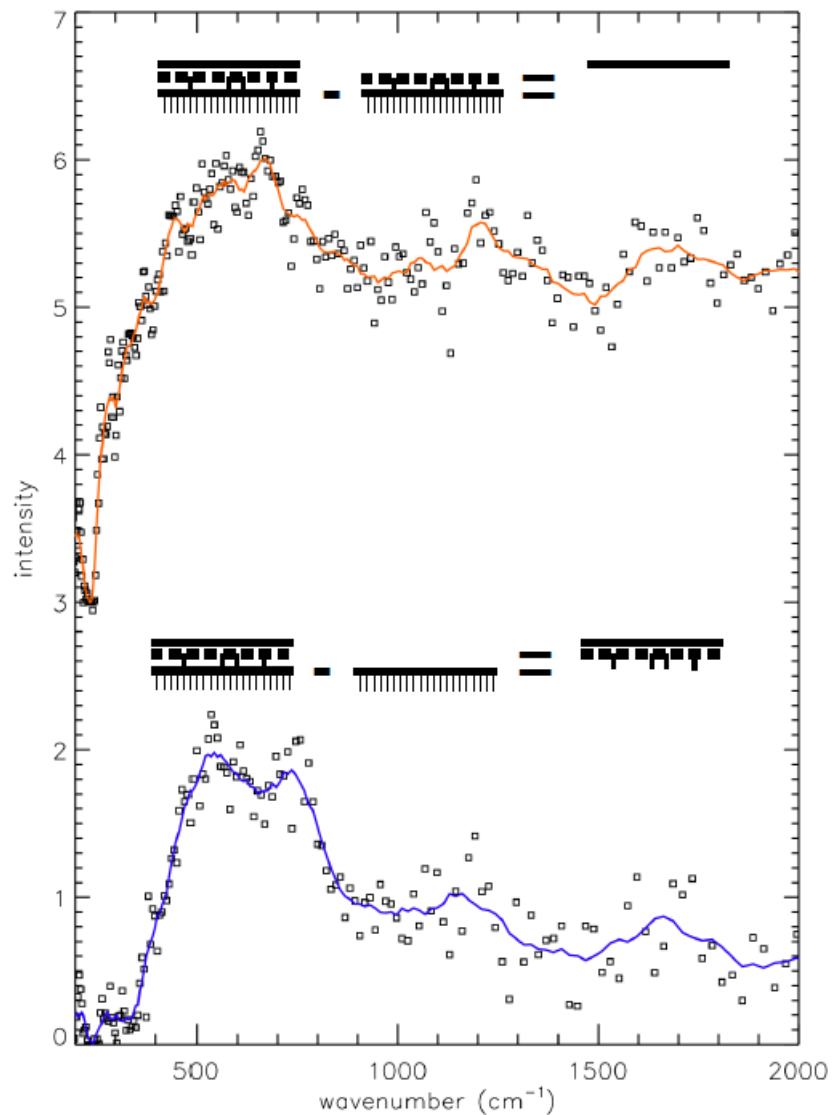
Fig. 4.2. The bottom curve is the difference between S2 (1ML water adsorbed on S1) and S4 (dried sample). The partial layer is still visible in the data. The top curve is the difference spectrum between S2 and S1. This operation removes the partial layer and highlights the water monolayer. The smooth character of the librational band is indicative of a disordered, liquid-like, weakly physisorbed monolayer. The solids lines are a smoothed version of the data.

Furthermore, the two monolayer (2ML) scenario is treated in a similar way to the

1ML above, i.e., the net result of S3 - S4 is the total of 2ML and the partial layer; S3 - S1

is only the spectrum of the 2ML (Table 4.1). The difference spectra can be found in Appendix C.

4.4.2 MD simulations

4.4.2.1 Structure

As mentioned above, the thermal wavelength of water at 10 K is 1.3 Å. Thus it would be inaccurate to use the classical MD to study the vibrational behavior of water at this temperature which involves dynamics with amplitudes smaller than this distance. However, at distances considerably greater than the de-Broglie wavelength of 1.3 Å, the classical description can still be informative. A study of structure at low temperatures is useful as the disorder due to kinetic energy is minimized. Therefore we chose to study the structural properties of water at 10 K while the vibrational studies are focused on 150 K. Further, it has been ascertained that the structural properties presented here are just a more ordered extension of those at 150 K with no new/additional qualitative feature appearing at 10 K. Detailed surface water structures and the interacting sites on the surface are illustrated by MD simulations. Fig. 4.3 shows the snapshots for water adsorbed on forsterite(010) surface at 10 K, with a length of 100 Å along the *b* direction including the thickness of the slab.
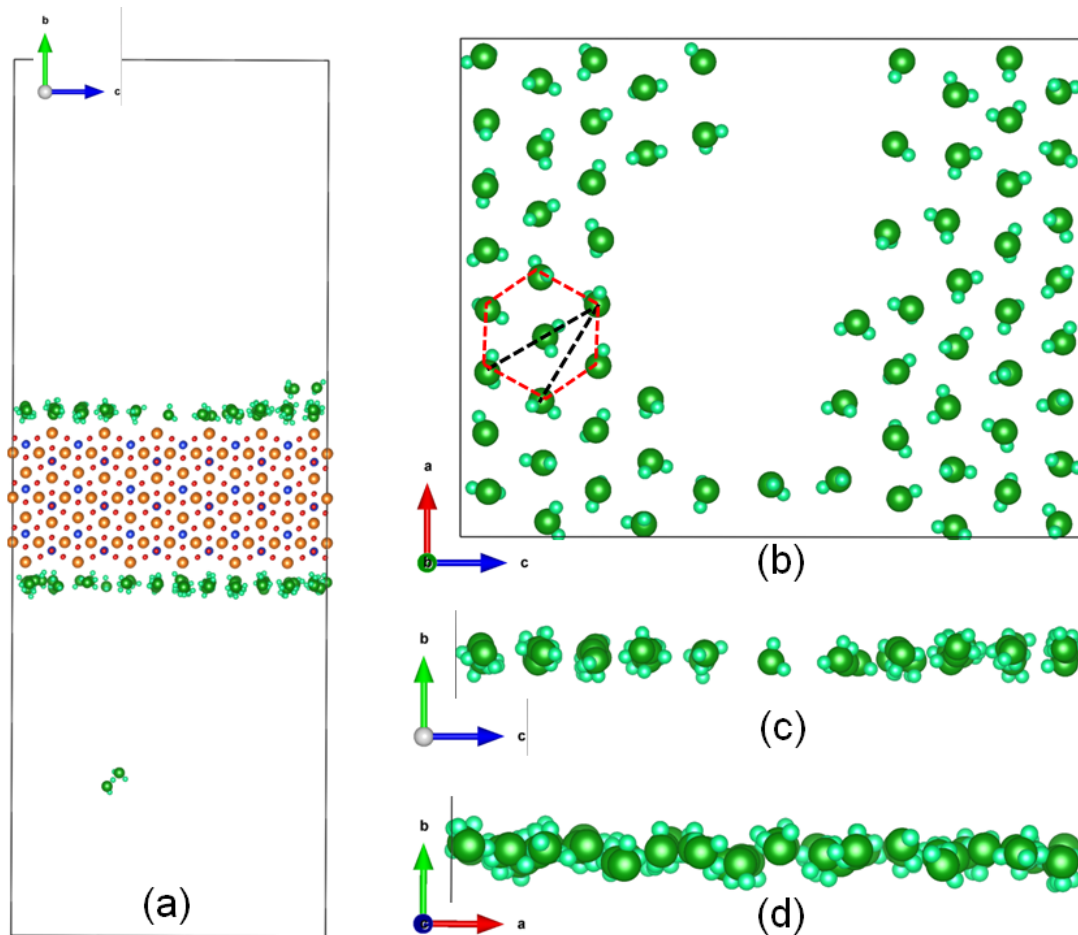
Fig. 4.3. Snapshot of simulation cells after equilibration of water molecules on forsterite(010) surface at 10 K(a). In forsterite, orange=Mg; red=O; blue=Si. For (b) ~ (d), only one side of the surface is presented. The free water molecules above the first monolayer and the solid surface atoms were removed for clarity. (b), (c), and (d) represent different perspectives of the water layer. The dashed hexagonal in (b) outlines the ordered structure within the water layer.

In Fig. 4.3a, the water molecules are closely packed on the surface, with a few in the free space. Fig. 4.3a, c, and d are the different side views of the water layer, while there is a strong layering seen in Fig. 4.3d with the center of mass of the molecules being basically in two different heights. Fig. 4.3b is the top view of one side of the surface water. We can observe the hexagonal ordered structure within the layer, highlighted by the red dashed line. Fig. 4.3b, d illustrate that the surface water structure is similar to that of ice Ih.

Radial distribution function (RDF) could aid in more detailed understanding for the water layer structure. Ow and Hw are used to denote water oxygen and hydrogen atoms throughout the study. Fig. 4.4 below examines the RDFs of the pairs of Ow-Ow, Ow-Hw, Hw-Hw, and Mg-Ow at 10 K. In Fig. 4.4a, the first dominant peak for the distance of Ow-Ow occurs at ~ 3.5 Å, which is larger than the Ow-Ow distance reported in the studies where the confining environment is more restricted, such as slits pores seen in graphene (Hirunsit and Balbuena, 2007). In graphitic structures that have a few angstrom wide slit pores, the Ow-Ow distance in confined water layer is ~ 2.6 - 2.7 Å (Hirunsit and Balbuena, 2007). The neighboring Ow-Ow distance in bulk ice is 2.74 ~ 2.76 Å in temperature range of 90 ~ 270 K (Thiel and Madey, 1987). However, in a single wall environment, i.e., surfaces unlike pores in this study, which is less restricted, the water molecules tend to reorient and redistribute, creating their own structures on the surface. In terms of the Ow-Hw and Hw-Hw distances in Fig. 4.4b, c, excluding the intramolecular distances that are shown in the insets, we observe the dominant peak positions are at ~ 3.4 Å and ~ 3.3 Å, respectively. One can notice that there are periodic

distances in Fig. 4.3a, b, and c. They are supposed to be contributed by the ordered structures of the surface water molecules. As mentioned above, ordered hexagonal structures can be observed within the first monolayer in Fig. 4.3b. It turned out that the distances indicated by the dashed lines in Fig. 4.3b correspond to the first three peaks in Fig. 4.4a. Thus, it is confirmed that the periodicity of distances shown for 10 K (Fig. 4.4a, b, and c) is due to the ice-like ordered structure of the water layer.

The first peak shown in Fig. 4.4d indicates the nearest distance between Ow and the uppermost Mg atom of forsterite(010) surface, suggesting a value of ~ 2.78 Å. Compared to the Mg-Ow distance of 2.19 Å in Kerisit et al. (2012), the temperature and pressure of their simulated forsterite/water system is at 50°C and 180 atm. The classical ionic bonding of Mg-O in the MgO crystal structure is 2.11 Å; therefore, our Mg-Ow bond distance determined in our system, other than an ionic bonding, is a reasonable result.
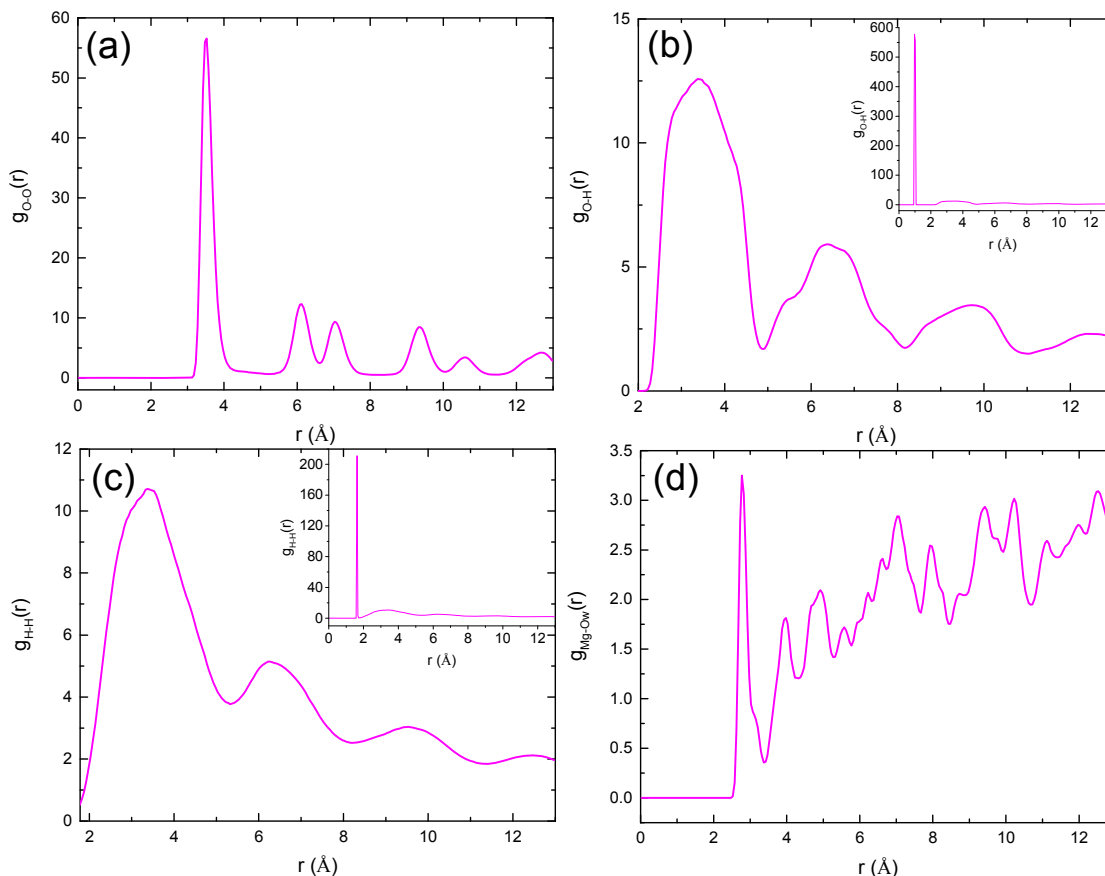
Fig. 4.4. Radial distribution function of (a) Ow-Ow, (b) Hw-Ow, (c) Hw-Hw, and (d) Mg-Ow. The dominant peaks in the insets of (b) and (c) show the intramolecular bond distances of Hw-Ow and Hw-Hw.

Because we see a strong layering within the water layer at 10 K in Fig. 4.3d, it is necessary to investigate the orientations of the molecules on the surface. Fig. 4.5 displays the orientation distributions along three directions. We used the angle between the position vector of Hw in the COM frame and the three Cartesian directions. The y-axis is normal to the surface as defined, so the distribution along the *y*-axis is of greater interest. For reference, we have added the isotropic orientational distribution curve (in black) in Fig. 4.5, where no orientational ordering is expected. In Fig. 4.5, we can see the preferential orientation with the *y* axis occurs at the angles of 25° and 155° for the water

molecules at 10 K. The angle of 25° corresponds to the molecules with one Hw dipping into the surface while the other Hw pointing up in their tilted configuration, and Ow interacting with the surface Mg atom. The angle of 155° corresponds to the molecules with one Hw dipping into the surface and Ow not interacting with the surface but the molecule forms hydrogen bond with another molecule. A simplified illustration of these two dominant configurations is presented in Fig. 4.6a. There is a less preference at 120° with the *y*-axis, as it corresponds to one Hw-Ow bond being parallel with the surface or the plane of the molecule is normal to the surface, which is rarely seen at 10 K in the ice-like structure. A density profile of the surface water is plotted to better illustrate the layering phenomenon, as shown in Fig. 4.6b. The splitting of the density profile in Fig. 4.6b corresponds to the preferential orientations of the molecules as we show in Fig. 4.6a. With the *x* and *z* axes in Fig. 4.5, we can see a 90° angle preference.
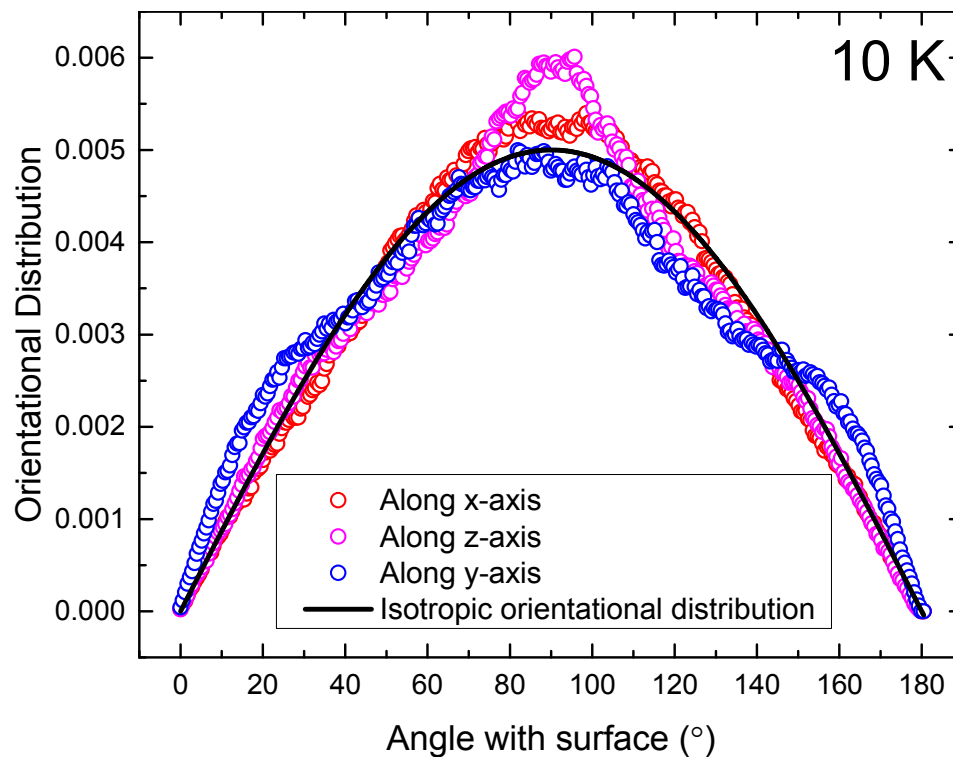
Fig. 4.5. Orientational distribution function using one Hw in the COM frame to observe its angle with three Cartesian directions. The black line is the isotropic orientational distribution which is used to weigh against the preferential orientational distribution of the molecules. *Y* axis is the direction normal to the surface.
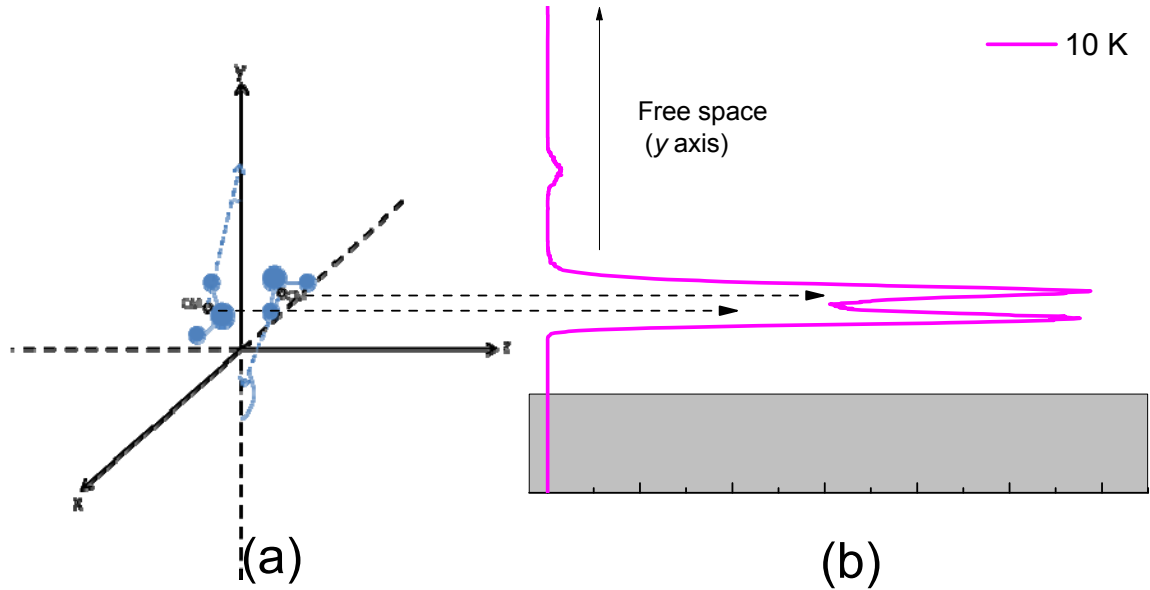
Fig. 4.6. An illustration of the 25° and 155° angle preferences at 10 K (a). The CM represents center of mass. The different heights of the CM is due to the Ih-like ice structure. Density profile in (b) with splitting peaks corresponds to the height difference proposed in (a), which are connected by the dotted arrow lines. The shaded area is part of the solid substrate.

4.4.2.2 Vibrational spectra - S(Q,ω)

The experiments were carried out on normal water (formula: H_2O) on nanopowdered forsterite surfaces. Because of the high incoherent scattering cross section of hydrogen, the major component of scattering signal in this experiment was incoherent scattering from water. Thus it can be assumed that the experimental signal was proportional to $S_{inc}(Q,\omega)$. To make a comparison with the experiment, we therefore calculated $S_{inc}(Q,\omega)$ by taking the Fourier Transform (FT) of self intermediate scattering function (ISF, I(Q,t)) of hydrogen atoms from the simulation. The ISF was calculated using the expression

$$I(Q,t) = \frac{1}{N}\sum_i \overline{\langle e^{iQ\cdot(r_i(t)-r_i(0))}\rangle} \qquad \text{Eqn (4.1)}$$

where Q is the momentum transfer, a quantity determined by the scattering angle that has the dimension of inversed length. The r is the position vector of Hw in the COM frame in the simulation. The angular brackets denote an ensemble average and the bar on top indicates averaging over Q vectors from all directions. The FT is applied through

$$S_{inc}(Q,\omega) = \frac{1}{2\pi} \int_{-\infty}^{\infty} [I(Q,t)]\exp(-i\omega t)dt \qquad \text{Eqn (4.2)}$$

In the calculation of $S_{inc}(Q,\omega)$ obtained from ISF, we have removed the contribution from translational motion by considering the positions of Hw in COM frame. Thus these $S_{inc}(Q,\omega)$ represent both rotational (librational) and vibrational (bending, stretching) contributions, which will be denoted as $S(Q,\omega)$ thereafter. Fig. 4.7 below used the average results of three Q values (1.5 Å^{-1}, 10.0 Å^{-1}, and 15.0 Å^{-1}), as comparable to the INS data which is the averaged results of 1.5 ~ 17.0 Å^{-1}. Fig. 4.7b, c, and d are the representations of Fig. 4.7a zoomed in for different regions, which might represent the librational, bending and stretching modes, respectively. The calculated vibrational spectra for the other temperatures can be found in Appendix C, as a comparison with 150 K.

The librational mode in Fig. 4.7b is indicated by a broad feature. There are some sharp features in the low frequency region that are contributed by the librational mode, e.g., ~ 60 cm^{-1} for 150 K in Fig. 4.7b (refer to Fig. C9 in Appendix C for the other temperatures). This is consistent with the INS experimental observations that sharp features appear with librational mode, indicative of finite adsorption sites. The bending mode shown in Fig. 4.7c is manifested for 150 K at ~ 1476 cm^{-1}. For the stretching mode

shown in Fig. 4.7d, the frequencies occur at ~ 3694 cm^{-1} and ~ 3765 cm^{-1}, which, as reported below, can be attributed to the symmetrical and asymmetrical stretching modes of the Hw-Ow bonds. .
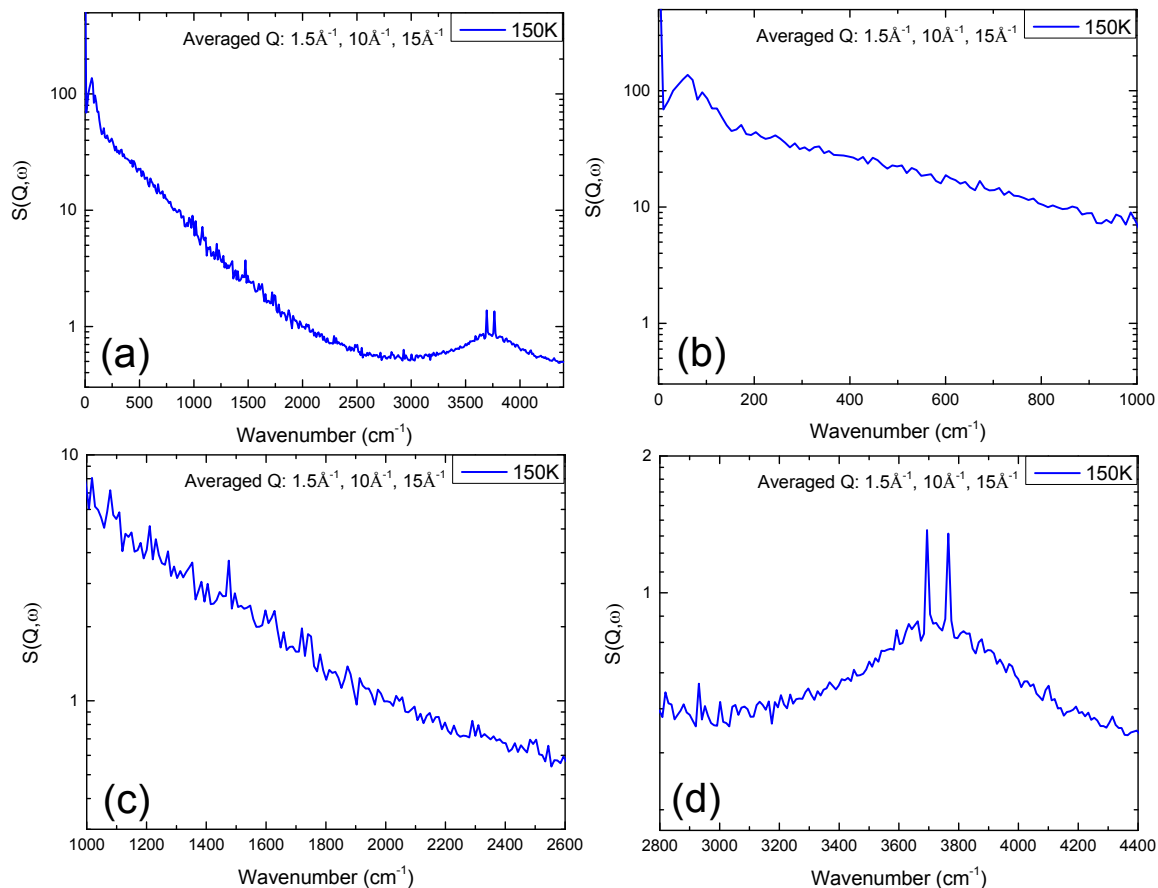
Fig. 4.7. Vibrational spectra shown by S(Q,ω) for water molecules on the Fo(010) surface at 150 K, an average result of three Q values. (a) full frequency range; (b), (c) and (d) are in different frequency ranges that represent the calculated librational, bending and stretching modes, respectively.

Suppressing the contribution from vibrations is possible by considering the time evolution of a unit vector along the position vector of Hw in COM frame. Using this unit vector in the expression for ISF, one can obtain ISF that would be dominated by rotational motion. We calculated the rotational ISF (RISF) and obtained parameters for

rotational motion as shown below. Fig. 4.8 shows the RISF curves for eight Q values at 150 K. We can see the rotational ISF curves do not decay to zero, as in the COM frame, one atom could not move to distance larger than its molecule size. The constant values at longer times are equal to the elastic incoherent structure factor (EISF), a quantity that can be measured in QENS experiments. The values were determined in the 20 ~ 30 ps range as they approached near constant values. The fluctuations at the end in each curve are due to the data noise because less accuracy is expected at the later time stage, due to time averaging. The EISF values determined at different Q values at the four temperature are shown in Fig. C11 in Appendix C.
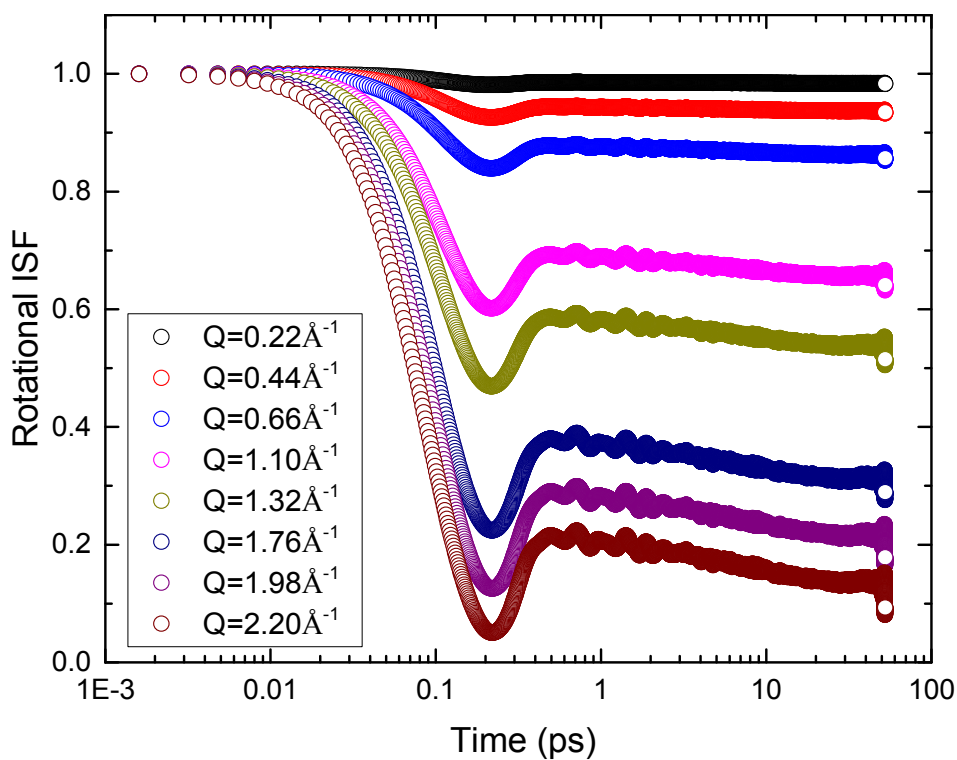

Fig. 4.8. Rotational ISF curves for eight Q values at 150 K.

4.4.2.3 Vibrational mode identification

In Fig. 4.9, we show a comparison between the S(Q,ω) obtained from the rotational ISF using a unit vector along the position vector of Hw atom in COM frame ($\hat{\boldsymbol{u}}_H$, illustrated in Fig. 4.9a) and a unit vector along the position vector of Ow atom in COM frame ($\hat{\boldsymbol{u}}_O$, illustrated in Fig. 4.9b). While the former can be expected to have contributions from librational and bending motions, the latter can have contributions from librational and stretching motions. The results were based on temperature of 150 K and $\boldsymbol{Q}$ = 15.0 Å^{-1}. In Fig. 4.9a, the major feature is the rotational oscillatory motion (libration), which extends up to ~ 800 cm^{-1}. It can also be seen that the stretching peak is completely removed for the $\hat{\boldsymbol{u}}_H$, but only bending mode as shown in the inset. In Fig. 4.9b, the major feature is also the rotational oscillatory motion (libration), which extends up to ~ 800 cm^{-1}. As shown in the inset, the bending peak is completely removed for the $\hat{\boldsymbol{u}}_O$, but only stretching mode, which should be attributed to the asymmetric stretching motion as it changes the direction of the unit vector. Thus we can conclude that the initial strong contribution in S(Q,ω) at low energies up to ~ 800 cm^{-1} is mainly due to librations.
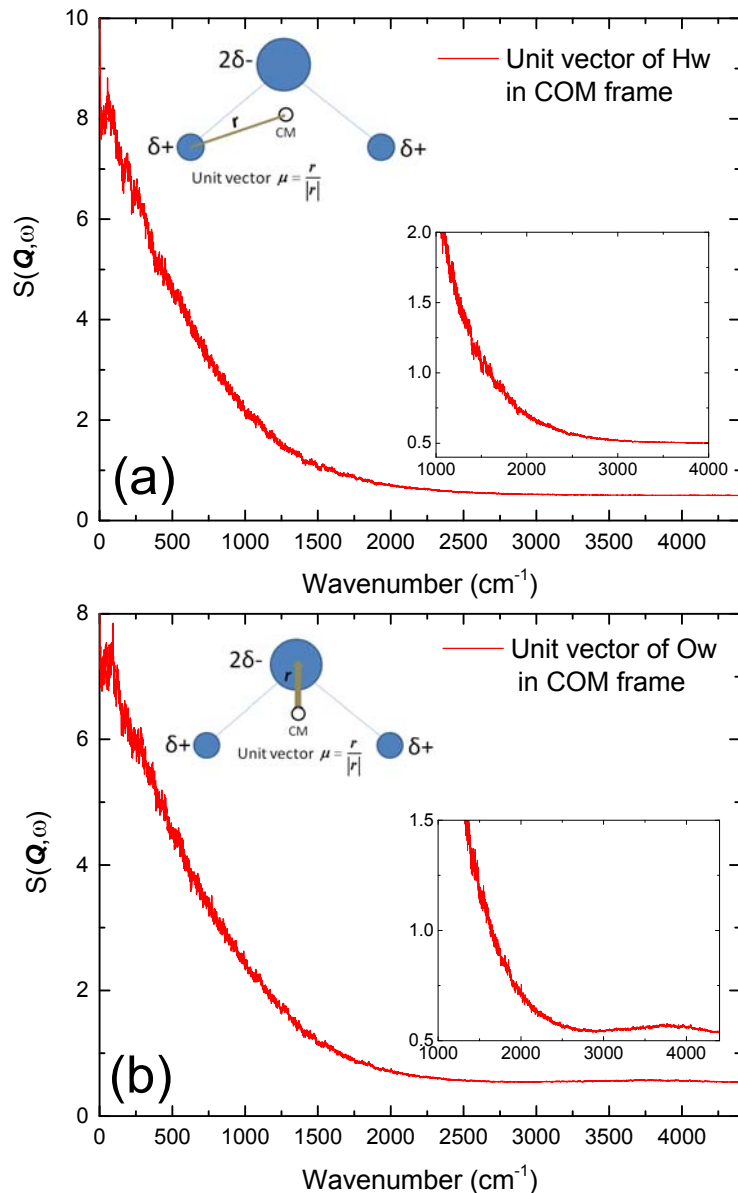
Fig. 4.9. $S(Q,\omega)$ of the unit vector along the position vectors of (a) Hw and (b) Ow in COM frame, using the data of 150 K at Q value of 15Å^{-1}. Both insets are used to manifest the peaks in the energy ranges of bending (a) and stretching (b) modes.

4.4.2.4 Surface water vs free water

Some of the molecules in the system adsorb on the Fo(010) surface at equilibrium at 150 K; however, some of them move into the free space of the simulation cell (Fig. C6b in Appendix C). The following discussion will focus on the different vibrational

behavior (frequency, magnitude) of the two types of molecules to illustrate the effect by the surface. One surface H_2O molecule and one free H_2O molecule were selected, respectively. Their two Hw-Ow bonds were investigated to observe the stretching mode. Fig. 4.10 plots the two Hw-Ow bond distances at each time step over 1 ps. We set the same time range to observe each Hw-Ow bond. For each plot in Fig. 4.10, we can see the bond distances change periodically. In Fig. 4.10a, b, we can see a 0.02 Å difference in their amplitude of variation, where the surface H_2O molecule has smaller amplitude of bond length variation. A similar observation is made with the second Hw-Ow bond (Fig. 4.10c, d).

If we compare the two Hw-Ow bonds within one H_2O molecule (Fig. 4.10a and c, b and d), we can see that their magnitudes are different and their variation is out of phase as in asymmetrical stretching.
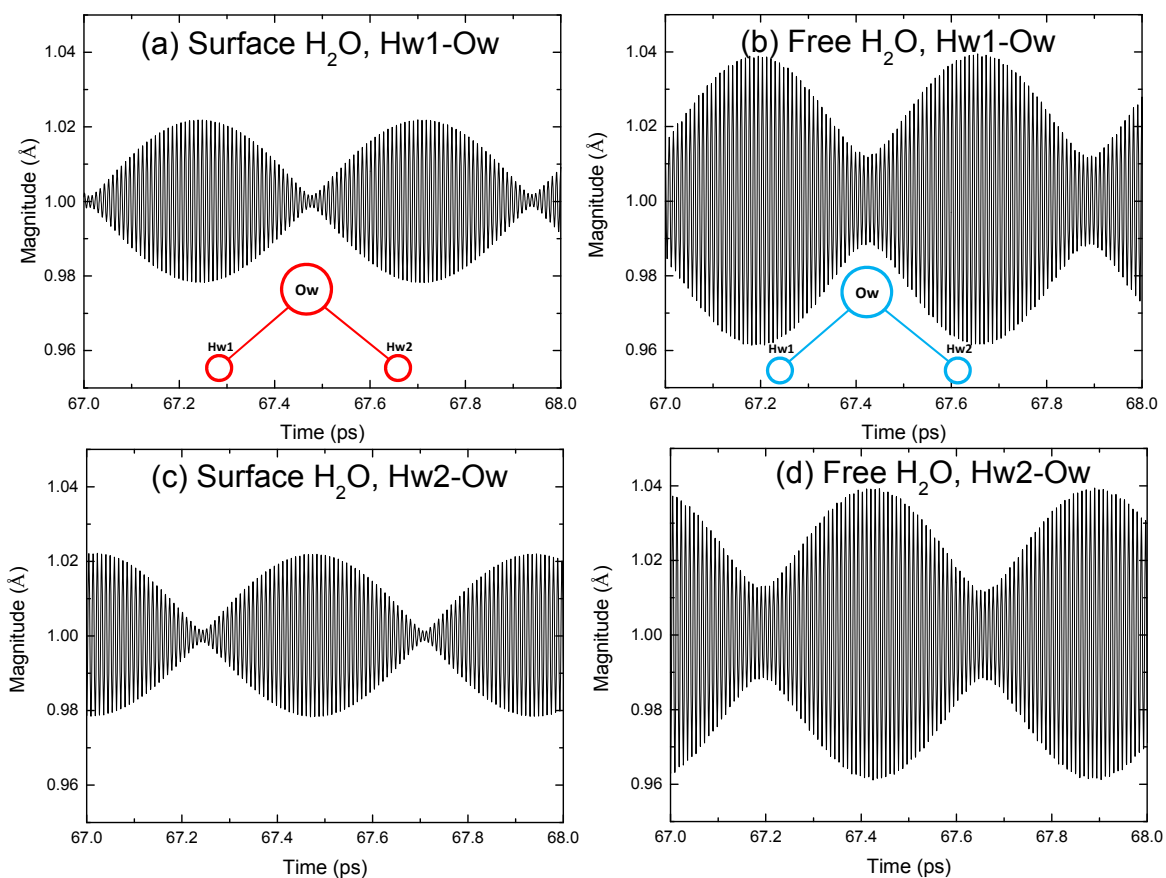
Fig. 4.10. Vibrational magnitude comparison for surface water molecule and free water molecule. Observations are made for Hw-Ow bonds at each time step within 1 ps. Stretching characteristics can be observed. (a) Hw1-Ow bond in one surface water molecule, (b) Hw1-Ow bond in one free water molecule, (c) Hw2-Ow bond in the same surface water molecule, and (d) Hw2-Ow bond in the same free water molecule.

Fig. 4.11 captures a finer time scale for the result of Fig. 4.10. Again, we can see the amplitude of bond length variation of surface H_2O is smaller than that of free H_2O by ~ 0.02 Å in both Hw-Ow bonds. The bond distances within one molecule are also different at most of the time steps, thus asymmetrical stretching can be claimed. By measuring the periodic time interval, we can identify the average periodicities in each plot are 0.00888 ps (3756 cm^{-1}), 0.00888 ps (3756 cm^{-1}), 0.00892 ps (3740 cm^{-1}), and

0.00888 ps (3756 cm^{-1}), respectively. Therefore, we can conclude that for the same bond, free H$_2$O molecule has a higher energy (3756 cm^{-1} vs 3740 cm^{-1}) than the surface H$_2$O molecule, as the surface H$_2$O is constrained by the surface.
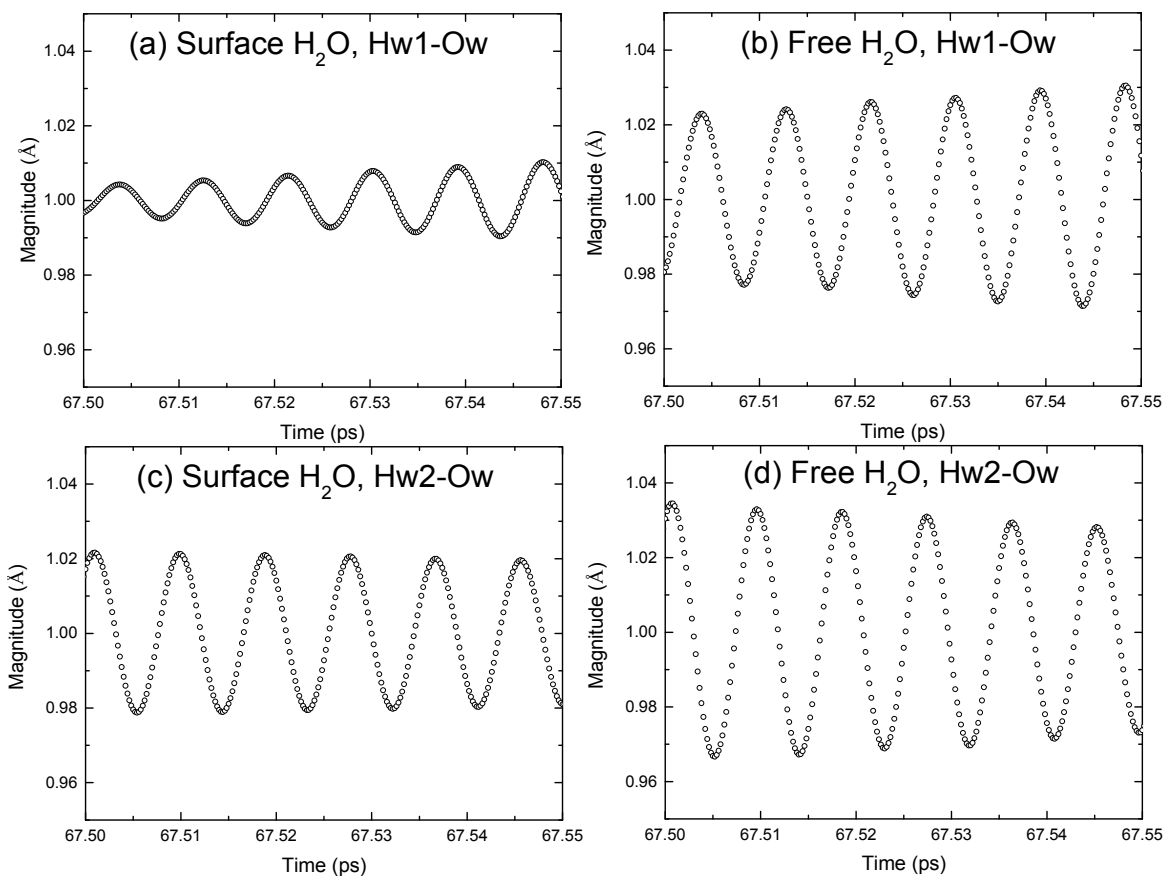
Fig. 4.11. Finer time scale result of vibrational magnitude of Hw-Ow bonds in surface H$_2$O (a, c) and free H$_2$O (b, d) molecules, in order to derive and verify the frequency of the stretching mode.

The bending mode can be observed by examining the Hw1-Hw2 distance magnitude within a molecule. Fig. 4.12 shows the vibrational magnitude variations over a certain period of time between two Hw atoms of surface H$_2$O (Fig. 4.12a) and free H$_2$O (Fig. 4.12b) molecules. Apparently, surface H$_2$O molecule has a smaller variation in

101

Hw1-Hw2 distance than the free H_2O molecule as expected according to its shorter Hw-Ow bond. In Fig. 4.12c, d, we determine the average periodicity for surface H_2O and free H_2O are 0.0181 ps and 0.0175 ps, corresponding to 1843 cm^{-1} and 1906 cm^{-1}, respectively. Once again, it shows free water has higher energy than the surface water.
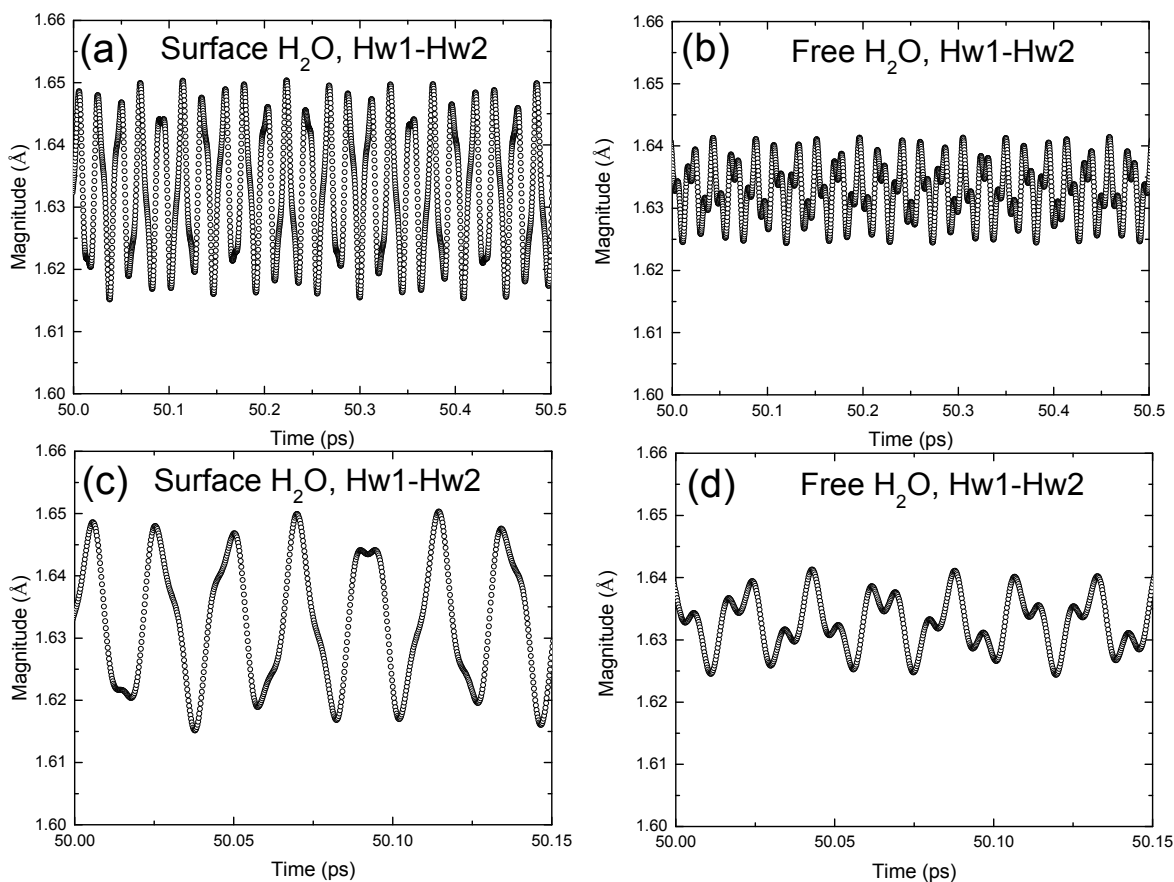
Fig. 4.12. Hw1-Hw2 vibrational magnitude along the time at 150 K, in order to derive and verify the bending mode frequency. (a) and (b) capture one surface H_2O and one free H_2O molecules, respectively. (c) and (d) are the zooming-in results of (a) and (b), for the purpose of identifying the periodicity.

4.5 Discussion and conclusions

Based on the analysis above, the vibrational behavior of 1ML water approached by MD simulations qualitatively agrees with the partial hydration/hydroxylation situation

in the INS experiment, instead of the independent 1ML in the experiment. The 1ML in INS experiment shows bulk-like behavior, as it does not interact with the forsterite surface directly. The difference for the water structure between the two techniques is that water molecules in the simulation on forsterite(010) surface are in the form of molecular water; while the water molecules on multiple surfaces in experiment may possess both molecular and dissociated water.

Both techniques illustrate a broad libration band with sharp features. However, the specific interaction sites and the structures of the adsorption layer are inaccessible in INS experiment; MD simulations aid in detailed understanding of the interface structure between water layer and forsterite(010) surface. At 10 K, Ow interacts with the surface Mg atom, and water molecules form an ordered Ih-like ice structure by the network of hydrogen bonding. MD simulations also identify the layering feature of the 1ML and the preferred orientations of the molecules by examining the density profile and orientational distribution function.

Spectra from INS experiment identify the librational and bending modes; while MD simulations at 150 K confirm the broad libration mode feature and reach agreement with experiment that sharp features exist with libration. In addition, MD simulations capture the symmetric and asymmetric stretching modes of water molecule by elucidating the bond distance variations of the two Hw-Ow bonds. The confining effect was also observed, investigated by comparing the amplitudes of vibration of the surface and free water molecules. Water layer structure and vibrational properties were also investigated for other temperatures (298, 50, and 10 K) in this study.

This complementary study using two robust tools establishes the basis for further water/mineral reactive systems. For future work, synthetic single crystals of olivine are preferred to use for further investigation of the fluid interfacial behavior on the dominant crystal planes. However, specific spectroscopic techniques are required to satisfy this path forward.

References

Allegretti F., O'Brien S., Polcik M., Sayago D. I. and Woodruff D. P. (2005) Adsorption Bond Length for H_2O on $TiO_2(110)$: A Key Parameter for Theoretical Understanding. *Phys. Rev. Lett.* **95**, 226104.

Alt J. C. and Shanks III W. C. (1998) Sulfur in serpentinized oceanic peridotites: Serpentinization processes and microbial sulfate reduction. *J. Geophys. Res.* **103**, 9917–9929.

Anovitz L. M., Rondinone A. J., Sochalski-Kolbus L., Rosenqvist J. and Cheshire M. C. (2017) Nano-scale synthesis of the complex silicate minerals forsterite and enstatite. *J. Colloid Interface Sci.* **495**, 94–101.

Asaduzzaman A., Laref S., Deymier P. A., Runge K., Cheng H.-P., Muralidharan K. and Drake M. J. (2013) A first-principles characterization of water adsorption on forsterite grains. *Philos. Trans. R. Soc. A* **371**, 20110582.

Ataca C., Aktürk E. and Ciraci S. (2009) Hydrogen storage of calcium atoms adsorbed on graphene : First-principles plane wave calculations. *Phys. Rev. B* **79**, 41406.

Bader R. F. W. (1990) *Atoms in Molecules: A Quantum Theory.*, Oxford, England.

Beard J. S. and Hopkinson L. (2000) A fossil, serpentinzation-related hydrothermal vent, Ocean Drilling Program Leg 173, Site 1068 (Iberia Abyssal Plain): Some aspects of mineral and fluid chemistry. *J. Geophys. Res.* **105**, 16527–16539.

Bengtsson L. (1999) Dipole correction for surface supercell calculations. *Phys. Rev. B* **59**, 12301–12304.

Berendsen H. J. C., Grigera J. R. and Straatsma T. P. (1987) The Missing Term in Effective Pair Potentialst. *J. Phys. Chem.* **91**, 6269–6271.

Blöchl P. E. (1994) Projector augmented-wave method. *Phys. Rev. B* **50**, 17953–17979.

Brownlee D. E., Tomandl D., Blanchard M. B., Ferry G. V and Kyte F. (1976) *An Atlas of extraterrestrial particles collected with NASA U-2 aircraft, 1974-1976.*,

Bruno M., Massaro F. R., Prencipe M., Demichelis R., Pierre M. D. La and Nestola F. (2014) Ab Initio Calculations of the Main Crystal Surfaces of Forsterite (Mg2SiO4): A Preliminary Study to Understand the Nature of Geochemical Processes at the Olivine Interface. *J. Phys. Chem. C* **118**, 2498–2506.

Bučko T., Hafner J., Lebègue S. and Ángyán J. G. (2010) Improved Description of the Structure of Molecular and Layered Crystals: Ab Initio DFT Calculations with van der Waals Corrections. *J. Phys. Chem. A* **114**, 11814–11824.

Capponi S., Arbe A., Alvarez F., Colmenero J., Frick B. and Embs J. P. (2009) Atomic motions in poly(vinyl methyl ether): A combined study by quasielastic neutron scattering and molecular dynamics simulations in the light of the mode coupling theory. *J. Chem. Phys.* **131**, 204901.

Carrasco J., Michaelides A. and Scheffler M. (2009) Insight from first principle into the nature of the bonding between water molecules and 4d metal surfaces. *J. Chem. Phys.* **130**, 184707.

Catti M., Gazzoni G. and Ivaldi G. (1983) Structures of Twinned β-Sr2SiO4 and of α'-Sr1.9Ba0.1SiO4. *Acta Crystallogr. Sect. C Cryst. Struct. Commun.* **39**, 29–34.

Catti M., Gazzoni G., Ivaldi G. and Zanini G. (1983) The beta<-> alpha' phase transition of Sr2SiO4. I. Order–disorder in the structure of the alpha' form at 383 K. *Acta Crystallogr. Sect. B Struct. Sci.* **39**, 674–679.

Charlou J. L., Bougault H., Appriou P., Nelsen T. and Rona P. (1991) Different TDM/CH4 hydrothermal plume signatures: TAG site at 26°N and serpentinized ultrabasic diapir at 15°05'N on the Mid-Atlantic Ridge. *Geochim. Cosmochim. Acta* **55**, 3209–3222.

Charlou J. L., Dmitriev L., Bougault H. and Needham H. D. (1988) Hydrothermal CH4 between 12°N and 15°N over the Mid-Atlantic Ridge. *Deep. Res.* **35**, 121–131.

Charlou J. L. and Donval J.-P. (1993) Hydrothermal Methane Venting between 12°N and 26°N Along the Mid-Atlantic Ridge. *J. Geophys. Res. Earth* **98**, 9625–9642.

Charlou J. L., Donval J. P., Jean-Baptiste P., Dapoigny A. and Rona P. A. (1996) Gases and helium isotopes in high temperature solutions sampled before and after ODP Leg 158 drilling at TAG hydrothermal field (26°N, MAR). *Geophys. Res. Lett.* **23**, 3491–3494.

Charlou J. L., Donval J. P., Konn C., Ondreas H., Fouquet Y., Jean-Baptiste P. and Fourre E. (2010) High Production and Fluxes of H2 and CH4 and Evidence of Abiotic Hydrocarbon Synthesis by Serpentinization in Ultramafic-Hosted Hydrothermal Systems on the Mid-Atlantic Ridge. *Geophys. Monogr. Ser. 188 - Divers. Hydrothermal Syst. Slow Spreading Ocean Ridges*, 265–296.

Charlou J. L., Fouquet Y., Bougault H., Donval J. P., Etoubleau J., Jean-Baptiste P., Dapoigny A., Appriou P. and Rona P. A. (1998) Intense CH4 plumes generated by serpentinization of ultramafic rocks at the intersection of the 15°20'N fracture zone and the Mid-Atlantic Ridge. *Geochim. Cosmochim. Acta* **62**, 2323–2333.

Chen S. and Navrotsky A. (2009) Calorimetric study of the surface energy of forsterite. *Am. Mineral.* **95**, 112–117.

Copley J. R. D. and Cook J. C. (2003) The Disk Chopper Spectrometer at NIST: a new instrument for quasielastic neutron scattering studies. *Chem. Phys.* **292**, 477–485.

Costa D., Sharkas K., Islam M. M. and Marcus P. (2009) Ab initio study of the chemical states of water on Cr2O3(0001): From the isolated molecule to saturation coverage. *Surf. Sci.* **603**, 2484–2493.

Cygan R. T., Liang J. and Kalinichev A. G. (2004) Molecular Models of Hydroxide , Oxyhydroxide , and Clay Phases and the Development of a General Force Field. *J. Phys. Chem. B* **108**, 1255–1266.

Deer W. A., Howie R. A. and Zussman J. (1982) *Rock-forming Minerals. Volume 1 A Orthosilicates.*, Longman Group, London.

Deringer V. L., Tchougréeff A. L. and Dronskowski R. (2011) Crystal Orbital Hamilton Population (COHP) Analysis As Projected from Plane-Wave Basis Sets. *J. Phys. Chem. A* **115**, 5461–5466.

Dick H. J. B. and Gillete H. (1976) Josephinite: Specimens from the earth's core? - A discussion. *Earth Planet. Sci. Lett.* **31**, 308–311.

Dronskowski R. and Bloechl P. E. (1993) Crystal orbital Hamilton populations (COHP): energy-resolved visualization of chemical bonding in solids based on density-functional calculations. *J. Phys. Chem.* **97**, 8617–8624.

Egelstaff P. (1967) *An introduction to the liquid state.*, Academic Press, London.

Finnie K. S., Cassidy D. J., Bartlett J. R. and Woolfrey J. L. (2001) IR Spectroscopy of Surface Water and Hydroxyl Species on Nanocrystalline TiO2 Films. *Langmuir*, 816–820.

Foley S. F., Prelevic D., Rehfeldt T. and Jacob D. E. (2013) Minor and trace elements in olivines as probes into early igneous and mantle melting processes. *Earth Planet. Sci. Lett.* **363**, 181–191.

Foustoukos D. I. and Seyfried Jr. W. E. (2004) Hydrocarbons in Hydrothermal Vent Fluids: The Role of Chromium-Bearing Catalysts. *Science* **304**, 1002–1005.

Frost B. R. (1985) On the stability of sulfides, oxides, and native metals in serpentinite. *J.*

Petrol. **26**, 31–63.

Fujino K., Sasaki S., Takéuchi Y. and Sadanaga R. (1981) X-ray determination of electron distributions in forsterite, fayalite and tephroite. *Acta Crystallogr. Sect. B Struct. Crystallogr. Cryst. Chem.* **37**, 513–518.

Gautam S. (2017) Use of quasielastic neutron scattering and molecular dynamics similation to study molecular dynamics under confinement. In *Horizons in World Physics* (ed. A. Reimer). Nova publisher, New York. pp. 25–44.

Gautam S., Alvarez F., Arbe A., Tyagi M., Frick B. and Colmenero J. (2011) Dynamical properties of plasticizer in polyvinyl acetate. In *AIP Conference Proceedings* pp. 583–584.

Gautam S., Mitra S., Mukhopadhyay R. and Chaplot S. L. (2006) Diffusion of acetylene inside Na-Y zeolite: Molecular dynamics simulation studies. *Phys. Rev. E* **74**, 41202.

Giacovazzo C., Monaco H. L., Viterbo D., Scordari F., Gilli G., Zanotti G. and Catti M. (1992) *Fundamentals of Crystallography*. ed. C. Giacovazzo, IUCr-Oxford University Press, New York.

Goldberg D. S., Takahashi T. and Slagle A. L. (2008) Carbon dioxide sequestration in deep-sea basalt. *Proc. Natl. Acad. Sci. U. S. A.* **105**, 9920–9925.

Greathouse J. A., Hart D. B., Bowers G. M., Kirkpatrick R. J. and Cygan R. T. (2015) Molecular Simulation of Structure and Diffusion at Smectite−Water Interfaces: Using Expanded Clay Interlayers as Model Nanopores. *J. Phys. Chem. C* **119**, 17126–17136.

Grimme S. (2011) Density functional theory with London dispersion corrections. *Wiley Interdiscip. Rev. Comput. Mol. Sci.* **1**, 211–228.

Grimme S., Antony J., Ehrlich S. and Krieg H. (2010) A consistent and accurate ab initio parametrization of density functional dispersion correction (DFT-D) for the 94 elements H-Pu. *J. Chem. Phys.* **132**, 154104.

Grimme S., Ehrlich S. and Goerigk L. (2011) Effect of the damping function in dispersion corrected density functional theory. *J. Comput. Chem.* **32**, 1456–1465.

Grimme S., Huenerbein R. and Ehrlich S. (2011) On the importance of the dispersion energy for the thermodynamic stability of molecules. *ChemPhysChem* **12**, 1258–61.

Grimme S., Hujo W. and Kirchner B. (2012) Performance of dispersion-corrected density functional theory for the interactions in ionic liquids. *Phys. Chem. Chem. Phys.* **14**, 4875–83.

Gysi A. P. and Stefánsson A. (2008) Numerical modelling of CO2-water-basalt interaction. *Mineral. Mag.* **72**, 55–59.

Hamilton V. E. and Christensen P. R. (2005) Evidence for extensive, olivine-rich bedrock on Mars. *Geology* **33**, 433–436.

Hammer B., Wendt S. and Besenbacher F. (2010) Water Adsorption on TiO2. *Top. Catal.* **53**, 423–430.

Henderson M. A. (2002) The interaction of water with solid surfaces : fundamental aspects revisited. *Surf. Sci. Rep.* **46**, 1–308.

Henkelman G., Arnaldsson A. and Jónsson H. (2006) A fast and robust algorithm for Bader decomposition of charge density. *Comput. Mater. Sci.* **36**, 354–360.

Hervig R. L., Smith J. V. and Dawson J. B. (1986) Lherzolite xenoliths in kimberlites and basalts: petrogenetic and crystallochemical significance of some minor and trace elements in olivine, pyroxenes, garnet and spinel. *Trans. Roy., Soc. Edin Ear Sci* **77**, 181–201.

Hinojosa B. B., Van Cleve T. and Asthagiri A. (2010) A first-principles study of H_2O adsorption and dissociation on the $SrTiO_3(100)$ surface. *Mol. Simul.* **36**, 604–617.

Hirunsit P. and Balbuena P. B. (2007) Effects of Confinement on Water Structure and Dynamics: A Molecular Simulation Study. *J. Phys. Chem. C* **111**, 1709–1715.

Hodgson A. and Haq S. (2009) Water adsorption and the wetting of metal surfaces. *Surf. Sci. Rep.* **64**, 381–451.

Hoefen T. M., Clark R. N., Bandfield J. L., Smith M. D., Pearl J. C. and Christensen P. R. (2003) Discovery of Olivine in the Nili Fossae Region of Mars. *Science* **302**, 627–630.

Holm N. G. and Charlou J. L. (2001) Initial indications of abiotic formation of hydrocarbons in the Rainbow ultramafic hydrothermal system, Mid-Atlantic Ridge. *Earth Planet. Sci. Lett.* **191**, 1–8.

Horita J. and Berndt M. E. (1999) Abiogenic Methane Formation and Isotopic Fractionation Under Hydrothermal Conditions. *Science* **285**, 1055–1057.

Hu X. L., Carrasco J., Klimes J. and Michaelides A. (2011) Trends in water monomer adsorption and dissociation on flat insulating surfaces. *Phys. Chem. Chem. Phys.* **13**, 12447–12453.

Hujo W. and Grimme S. (2012) Performance of Non-Local and Atom-Pairwise Dispersion Corrections to DFT for Structural Parameters of Molecules with Noncovalent Interactions. *J. Chem. Theory Comput.* **9**, 308–315.

Isaacson P. J., Pieters C. M., Besse S., Clark R. N., Head J. W., Klima R. L., Mustard J. F., Petro N. E., Staid M. I., Sunshine J. M., Taylor L. A., Thaisen K. G. and Tompkins S. (2011) Remote compositional analysis of lunar olivine-rich lithologies with Moon Mineralogy Mapper (M3) spectra. *J. Geophys. Res. E Planets* **116**, E00G11.

Kerisit S., Bylaska E. J. and Felmy A. R. (2013) Water and carbon dioxide adsorption at olivine surfaces. *Chem. Geol.* **359**, 81–89.

Kerisit S., Weare J. H. and Felmy A. R. (2012) Structure and dynamics of forsterite–scCO$_2$/H$_2$O interfaces as a function of water content. *Geochim. Cosmochim. Acta* **84**, 137–151.

King H. E., Stimpfl M., Deymier P., Drake M. J., Catlow C. R. A., Putnis A. and de Leeuw N. H. (2010) Computer simulations of water interactions with low-coordinated forsterite surface sites: Implications for the origin of water in the inner solar system. *Earth Planet. Sci. Lett.* **300**, 11–18.

Klein F. and Bach W. (2009) Fe-Ni-Co-O-S phase relations in peridotite-seawater interactions. *J. Petrol.* **50**, 37–59.

Koeberl C., Hagen E. H. and Faure G. (1989) Extraterrestrial Spherules from Glacial Sediment in Antarctica: Internal Structure, Mineralogy, and Chemical Composition. In *Lunar and Planetary Science Conference* pp. 528–529.

Koeppen W. C. and Hamilton V. E. (2008) Global distribution, composition, and abundance of olivine on the surface of Mars from thermal infrared data. *J. Geophys. Res.* **113**, E05001.

de Koker N. (2009) Thermal Conductivity of MgO Periclase from Equilibrium First Principles Molecular Dynamics. *Phys. Rev. Lett.* **103**, 125902.

Kresse G. and Furthmüller J. (1996) Efficient iterative schemes for ab initio total-energy calculations using a plane-wave basis set. *Phys. Rev. B* **54**, 11169–11186.

Kresse G. and Hafner J. (1994a) Ab initio molecular-dynamics simulation of the liquid-metal-amorphous-semiconductor transition in germanium. *Phys. Rev. B* **49**, 14251–14269.

Kresse G. and Hafner J. (1993) Ab initio molecular dynamics for liquid metals. *Phys. Rev. B* **47**, 558–561.

Kresse G. and Hafner J. (1994b) Norm-conserving and ultrasoft pseudopotentials for first-row and transition elements. *J. Phys Condens. Matter* **6**, 8245–8257.

Kresse G. and Joubert D. (1999) From ultrasoft pseudopotentials to the projector

augmented-wave method. *Phys. Rev. B* **59**, 1758–1775.

Krot A. N., Petaev M. I., Russell S. S., Itoh S., Fagan T. J., Yurimoto H., Chizmadia L., Weisberg M. K., Komatsu M., Ulyanov A. A. and Keil K. (2004) Amoeboid olivine aggregates and related objects in carbonaceous chondrites: Records of nebular and asteroid processes. *Chemie der Erde - Geochemistry* **64**, 185–239.

Krynicki K., Green C. D. and Sawyer D. W. (1978) Pressure and temperature dependence of self-diffusion in water. *Faraday Discuss. Chem. Soc.* **66**, 199–208.

Lager G. A., Ross F. K., Rotella F. J. and Jorgensen J. D. (1981) Neutron powder diffraction of forsterite, Mg2SiO4: a comparison with single-crystal investigation. *J. Appl. Cryst.* **14**, 137–139.

Lee K., Kelkkanen A. K., Berland K., Andersson S., Langreth D. C., Schröder E., Lundqvist B. I. and Hyldgaard P. (2011) Evaluation of a density functional with account of van der Waals forces using experimental data of H2 physisorption on Cu(111). *Phys. Rev. B* **84**, 193408.

Lee S. H. and Rossky P. J. (1994) A comparison of the structure and dynamics of liquid water at hydrophobic and hydrophilic surfaces—a molecular dynamics simulation study. *J. Chem. Phys.* **100**, 3334–3345.

de Leeuw N. H. (2001) Density Functional Theory Calculations of Hydrogen-Containing Defects in Forsterite, Periclase, and alpha-Quartz. *J. Phys. Chem. B* **105**, 9747–9754.

de Leeuw N. H. and Parker S. C. (1998) Molecular-dynamics simulation of MgO surfaces in liquid water using a shell-model potential for water. *Phys. Rev. B* **58**, 13901–13908.

de Leeuw N. H., Parker S. C., Catlow C. R. a. and Price G. D. (2000) Modelling the effect of water on the surface structure and stability of forsterite. *Phys. Chem. Miner.* **27**, 332–341.

Levchenko A. A., Kolesnikov A. I., Ross N. L., Boerio-goates J., Woodfield B. F., Li G. and Navrotsky A. (2007) Dynamics of Water Confined on a TiO2 (Anatase) Surface. *J. Phys. Chem. A* **111**, 12584–12588.

Li J. (1996) Inelastic neutron scattering studies of hydrogen bonding in ices. *J. Chem. Phys.* **105**, 6733–6755.

Liechtenstein A. I., Anisimov V. I. and Zaanen J. (1995) Density-functional theory and strong interactions: Orbital ordering in Mott-Hubbard insulators. *Phys. Rev. B* **52**, R5467–R5470.

Loring J. S., Thompson C. J., Wang Z., Joly A. G., Sklarew D. S., Schaef H. T., Ilton E. S., Rosso K. M. and Felmy A. R. (2011) In situ infrared spectroscopic study of forsterite carbonation in wet supercritical CO2. *Environ. Sci. Technol.* **45**, 6204–10.

Lucey P. G. (2004) Mineral maps of the Moon. *Geophys. Res. Lett.* **31**, L08701.

Maintz S., Deringer V. L., Tchougreeff A. L. and Dronskowski R. (2016) LOBSTER: A tool to extract chemical bonding from plane-wave based DFT. *J. Comput. Chem.* **37**, 1030–1035.

Maintz S., Deringer V. L., Tchougréeff A. L. and Dronskowski R. (2013) Analytic projection from plane-wave and PAW wavefunctions and application to chemical-bonding analysis in solids. *J. Comput. Chem.* **34**, 2557–2567.

Mamontov E., Vlcek L., Wesolowski D. J., Cummings P. T., Wang W., Anovitz L. M., Rosenqvist J., Brown C. M. and Sakai V. G. (2007) Dynamics and Structure of Hydration Water on Rutile and Cassiterite Nanopowders Studied by Quasielastic Neutron Scattering and Molecular Dynamics Simulations. *J. Phys. Chem. C* **111**, 4328–4341.

Mamontov E., Wesolowski D. J., Vlcek L., Cummings P. T., Rosenqvist J., Wang W. and Cole D. R. (2008) Dynamics of Hydration Water on Rutile Studied by Backscattering Neutron Spectroscopy and Molecular Dynamics Simulation. *J. Phys. Chem. C* **112**, 12334–12341.

Manz T. A. and Sholl D. S. (2010) Chemically meaningful atomic charges that reproduce the electrostatic potential in periodic and nonperiodic materials. *J. Chem. Theory Comput.* **6**, 2455–2468.

Manz T. A. and Sholl D. S. (2012) Improved Atoms-in-Molecule Charge Partitioning Functional for Simultaneously Reproducing the Electrostatic Potential and Chemical States in Periodic and Nonperiodic Materials. *J. Chem. Theory Comput.* **8**, 2844–2867.

Mason B. (1967) Extraterrestrial mineralogy. *Am. Mineral.* **52**, 307–325.

Matter J. M., Broecker W. S., Stute M., Gislason S. R., Oelkers E. H., Stefánsson A., Wolff-Boenisch D., Gunnlaugsson E., Axelsson G. and Bjorsson G. (2009) Permanent Carbon Dioxide Storage into Basalt : The CarbFix Pilot Project, Iceland. *Energy Procedia* **1**, 3641–3646.

Matter J. M., Takahashi T. and Goldberg D. (2007) Experimental evaluation of in situ CO2-water-rock reactions during CO2 injection in basaltic rocks: Implications for geological CO2 sequestration. *Geochemistry, Geophys. Geosystems* **8**, 1–19.

McClellan A. L. and Harnsberger H. F. (1967) Cross-sectional areas of molecules

adsorbed on solid surfaces. *J. Colloid Interface Sci.* **23**, 577–599.

McCollom T. M. (2013) Laboratory Simulations of Abiotic Hydrocarbon Formation in Earth's Deep Subsurface. *Rev. Mineral. Geochemistry* **75**, 467–494.

McCollom T. M., Lollar B. S., Lacrampe-Couloume G. and Seewald J. S. (2010) The influence of carbon source on abiotic organic synthesis and carbon isotope fractionation under hydrothermal conditions. *Geochim. Cosmochim. Acta* **74**, 2717–2740.

Mccollom T. M. and Seewald J. S. (2007) Abiotic Synthesis of Organic Compounds in Deep-Sea Hydrothermal Environments on Abiotic Synthesis. *Chem. Rev.* **107**, 382–401.

McCollom T. M. and Seewald J. S. (2001) A reassessment of the potential for reduction of dissolved CO2 to hydrocarbons during serpentinization of olivine. *Geochim. Cosmochim. Acta* **65**, 3769–3778.

McCollom T. M. and Seewald J. S. (2007) Abiotic Synthesis of Organic Compounds in Deep-Sea Hydrothermal Environments. *Chem. Rev.* **107**, 382–401.

McCollom T. M. and Seewald J. S. (2013) Serpentinites, Hydrogen, and Life. *Elements* **9**, 129–134.

McGrail B. P., Schaef H. T., Ho A. M., Chien Y.-J., Dooley J. J. and Davidson C. L. (2006) Potential for carbon dioxide sequestration in flood basalts. *J. Geophys. Res.* **111**, B12201.

McSween H. Y., Wyatt M. B., Gellert R., Bell III J. F., Morris R. V., Herkenhoff K. E., Crumpler L. S., Milam K. A., Stockstill K. R., Tornabene L. L., Arvidson R. E., Bartlett P., Blaney D., Cabrol N. A., Christensen P. R., Clark B. C., Crisp J. A., Des Marais D. J., Economou T., Farmer J. D., Farrand W., Ghosh A., Golombek M., Gorevan S., Greeley R., Hamilton V. E., Johnson J. R., Joliff B. L., Klingelhofer G., Knudson A. T., McLennan S., Ming D., Moersch J. E., Rieder R., Ruff S. W., Schroder C., de Souza Jr P. A., Squyres S. W., Wanke H., Wang A., Yen A. and Zipfel J. (2006) Characterization and petrologic interpretation of olivine-rich basalts at Gusev Crater, Mars. *J. Geophys. Res. E Planets* **111**, E02S10.

Meng S., Wang E. G. and Gao S. (2004) Water adsorption on metal surfaces : A general picture from density functional theory studies. *Phys. Rev. B* **69**, 195404.

Michaelides A., Ranea V. A., Andres P. L. De and King D. A. (2003) General Model for Water Monomer Adsorption on Close-Packed Transition and Noble Metal Surfaces. *Phys. Rev. Lett.* **90**, 216102.

Michot L. J., Delville A., Humbert B., Plazanet M. and Levitz P. (2007) Diffusion of

Water in a Synthetic Clay with Tetrahedral Charges by Combined Neutron Time-of-Flight Measurements and Molecular Dynamics Simulations. *J. Phys. Chem. CPhys* **111**, 9818–9831.

Monkhorst H. J. and Pack J. D. (1976) Special points for Brillouin-zone integrations. *Phys. Chem. Chem. Phys.* **13**, 5188–5192.

Moroz L., Schade U. and Wasch R. (2000) Reflectance Spectra of Olivine–Orthopyroxene-Bearing Assemblages at Decreased Temperatures: Implications for Remote Sensing of Asteroids. *Icarus* **147**, 79–93.

Morris R. V., Klingelhöfer G., Schröder C., Rodionov D. S., Yen A., Ming D. W., de Souza Jr P. A., Fleischer I., Wdowiak T., Gellert R., Bernhardt B., Evlanov E. N., Zubkov B., Foh J., Bonnes U., Kankeleit E., Gütlich P., Renz F., Squyres S. W. and Arvidson R. E. (2006) Mossbauer mineralogy of rock, soil, and dust at Gusev crater, Mars: Spirit's journey through weakly altered olivine basalt on the plains and pervasively altered basalt in the Columbia Hills. *J. Geophys. Res. E Planets* **111**, E02S13.

Mu R., Zhao Z., Dohnálek Z. and Gong J. (2017) Structural motifs of water on metal oxide surfaces. *Chem. Soc. Rev.* **46**, 1785–1806.

Mustard J. F., Poulet F., Gendrin A., Bibring J.-P., Langevin Y., Gondet B., Mangold N., Bellucci G. and Altieri F. (2005) Olivine and Pyroxene Diversity in the Crust of Mars. *Science* **307**, 1594–1597.

Noguera C. (2000) Polar oxide surfaces. *J. Phys. Condens. Matter* **12**, R367–R410.

Oelkers E. H., Gislason S. R. and Matter J. (2008) Mineral Carbonation of CO2. *Elements* **4**, 333–337.

Perdew J., Burke K. and Ernzerhof M. (1996) Generalized Gradient Approximation Made Simple. *Phys. Rev. Lett.* **77**, 3865–3868.

Power I. M., Wilson S. A. and Dipple G. M. (2013) Serpentinite carbonation for CO2 sequestration. *Elements* **9**, 115–122.

Preuss M., Schmidt W. G. and Bechstedt F. (2005) Coulombic amino group-metal bonding: Adsorption of adenine on Cu(110). *Phys. Rev. Lett.* **94**, 236102.

Prigiobbe V., Suarez Negreira A. and Wilcox J. (2013) Interaction between Olivine and Water Based on Density Functional Theory Calculations. *J. Phys. Chem. C* **117**, 21203–21216.

Proskurowski G., Lilley M. D., Seewald J. S., Früh-green G. L., Olson E. J., Lupton J. E., Sylva S. P. and Kelley D. S. (2008) Abiogenic Hydrocarbon Production at Lost City

Hydrothermal Field. *Science* **319**, 604–607.

Reckien W., Janetzko F., Peintinger M. F. and Bredow T. (2012) Implementation of empirical dispersion corrections to density functional theory for periodic systems. *J. Comput. Chem.* **33**, 2023–31.

Riplinger C. and Carter E. A. (2015) Cooperative Effects in Water Binding to Cuprous Oxide Surfaces. *J. Phys. Chem. C* **119**, 9311–9323.

Rohrbach A., Hafner J. and Kresse G. (2004) Ab initio study of the (0001) surfaces of hematite and chromia: Influence of strong electronic correlations. *Phys. Rev. B* **70**, 125426.

Sanville E., Kenny S. D., Smith R. and Henkelman G. (2007) Improved grid-based algorithm for Bader charge allocation. *J. Comput. Chem.* **28**, 899–908.

Shannon R. D. (1976) Revised Effective Ionic Radii and Systematic Studies of Interatomic Distances in Halides and Chaleogenides. *Acta Crystallogr. Sect. A* **32**, 751–767.

Shannon R. D. and Prewitt C. T. (1969) Effective ionic radii in oxides and fluorides. *Acta Crystallogr. Sect. B Struct. Crystallogr. Cryst. Chem.* **25**, 925–946.

Sheppard D., Terrell R. and Henkelman G. (2008) Optimization methods for finding minimum energy paths. *J. Chem. Phys.* **128**, 134106.

Sivia D. S., Vorderwisch P. and Silver R. N. (1990) Deconvolution of data from the filter difference spectrometer: from hardware to maximum entropy. *Nucl. Instruments Methods Phys. Res. Sect. A Accel. Spectrometers, Detect. Assoc. Equip.* **290**, 492–498.

Smyth J. R. (1975) High temperature crystal chemistry of fayalite. *Am. Mineral.* **60**, 1092–1097.

Spencer E. C., Huang B., Parker S. F., Kolesnikov A. I., Ross N. L. and Woodfield B. F. (2013) The thermodynamic properties of hydrated γ-Al2O3 nanoparticles. *J. Chem. Phys.* **139**, 244705.

Spencer E. C., Levchenko A. a, Ross N. L., Kolesnikov A. I., Boerio-Goates J., Woodfield B. F., Navrotsky A. and Li G. (2009) Inelastic neutron scattering study of confined surface water on rutile nanoparticles. *J. Phys. Chem. A* **113**, 2796–800.

Spencer E. C., Parker S. F. and Ross N. L. (2012) Thermodynamic properties of water confined on the surface of PdO nanoparticles. *J. Chem. Thermodyn.* **51**, 103–106.

Spencer E. C., Ross N. L., Parker S. F., Kolesnikov A. I., Wood B. F., Wood K., Rytting M., Boerio-goates J. and Navrotksy A. (2011) Influence of Particle Size and Water

Coverage on the Thermodynamic Properties of Water Confined on the Surface of SnO 2 Cassiterite Nanoparticles. *J. Phys. Chem. C* **115**, 21105–21112.

Spencer E. C., Ross N. L., Parker S. F., Olsen R. E. and Woodfield B. F. (2013) Inelastic neutron scattering studies of hydrated CuO, ZnO and CeO2 nanoparticles. *Chem. Phys.* **427**, 66–70.

Stack A. G., Borreguero J. M., Prisk T. R., Mamontov E., Wang H.-W., Vlcek L. and Wesolowski D. J. (2016) Precise determination of water exchange on a mineral surface. *Phys. Chem. Chem. Phys.* **18**, 28819–28828.

Stimpfl M., Walker A. M., Drake M. J., de Leeuw N. H. and Deymier P. (2006) An ångström-sized window on the origin of water in the inner solar system: Atomistic simulation of adsorption of water on olivine. *J. Cryst. Growth* **294**, 83–95.

Sunshine J. M., Bus S. J., Corrigan C. M., McCoy T. J. and Burbine T. H. (2007) Olivine-dominated asteroids and meteorites: Distinguishing nebular and igneous histories. *Meteorit. Planet. Sci. Arch.* **42**, 155–170.

Szabova L., Tateyama Y., Matolin V. and Fabris S. (2015) Water Adsorption and Dissociation at Metal-Supported Ceria Thin Films: Thickness and Interface-Proximity Effects Studied with DFT+U Calculations. *J. Phys. Chem. C* **119**, 2537–2544.

Szurgot M., Polanski K. and Krystek M. (2008) Electron and optical microscopy studies of extraterrestrial minerals in NWA4047 meteorite. *Cryst. Res. Technol.* **43**, 656–665.

Tafto J. and Spence J. C. H. (1982) Crystal Site Location of Iron and Trace Elements in a Magnesium-Iron Olivine by a New Crystallographic Technique. *Science* **218**, 49–51.

Tamada, O., Fujino, K., Sasaki S. (1983) Structures and Electron Distributions of alpha-Co2SiO4 and alpha-Ni2SiO4 (Olivine Structure). *Acta Crystallogr. Sect. B Struct. Crystallogr. Cryst. Chem.* **B39**, 692–697.

Tang W., Sanville E. and Henkelman G. (2009) A grid-based Bader analysis algorithm without lattice bias. *J. Phys. Condens. Matter* **21**, 84204.

Thiel P. A. and Madey T. E. (1987) The interaction of water with solid surfaces: Fundamental aspects. *Surf. Sci. Rep.* **7**, 211–385.

Thompson C. J., Martin P. F., Chen J., Benezeth P., Schaef H. T., Rosso K. M., Felmy A. R. and Loring J. S. (2014) Automated high-pressure titration system with in situ infrared spectroscopic detection. *Rev. Sci. Instrum.* **85**, 44102.

Todorov I. T., Smith W., Trachenko K. and Dove M. T. (2006) DL_POLY_3: new

dimensions in molecular dynamics simulations via massive parallelism. *J. Mater. Chem.* **16**, 1911–1918.

Toukan K. and Rahman A. (1985) Molecular-dynamics study of atomic motions in water. *Phys. Rev. B* **31**, 2643–2648.

Udagawa S., Urabe K., Natsume M. and Yano T. (1980) Refinement of the crystal structure of γ-Ca2SiO4. *Cem. Concr. Res.* **10**, 139–144.

Wang H.-W., DelloStritto M. J., Kumar N., Kolesnikov A. I., Kent P. R. C., Kubicki J. D., Wesolowski D. J. and Sofo J. O. (2014) Vibrational Density of States of Strongly H-Bonded Interfacial Water: Insights from Inelastic Neutron Scattering and Theory. *J. Phys. Chem. C* **118**, 10805–10813.

Wang J., Kalinichev A. G. and Kirkpatrick R. J. (2006) Effects of substrate structure and composition on the structure, dynamics, and energetics of water at mineral surfaces: A molecular dynamics modeling study. *Geochim. Cosmochim. Acta* **70**, 562–582.

Wang J., Kalinichev A. G., Kirkpatrick R. J. and Cygan R. T. (2005) Structure, Energetics, and Dynamics of Water Adsorbed on the Muscovite (001) Surface: A Molecular Dynamics Simulation. *J. Phys. Chem. B* **109**, 15893–15905.

Wang P., Wang H. and Yang W. (2014) Anomalous high adsorption energy of H_2O on fluorinated graphenes: a first principles study. *Phys. Chem. Chem. Phys.* **16**, 20464–20470.

Appendix A: Water Adsorption on Olivine(010) Surfaces: Effect of Alkali and Transition

Metal Cation Doping

Section I. Bulk structure of olivine and the (010) surface

(1) Bulk Olivine Structure

Olivine (M_2SiO_4) has an orthorombic crystal structure in the *Pbnm* space group. 'M' in the molecular formula can represent a suite of alkaline earth and transition metal cations. The metal cations form irregular octahedra with six oxygen atoms that have two elongated M-O bonds. Common olivine mineral is a solid solution with Mg and Fe, and there are two metal, one silicon and three oxygen occupancies in one unit cell. Fig. A1a, b below shows two views of the crystal structure of olivine with the (100) and (001) lattice vectors normal to the page, respectively.
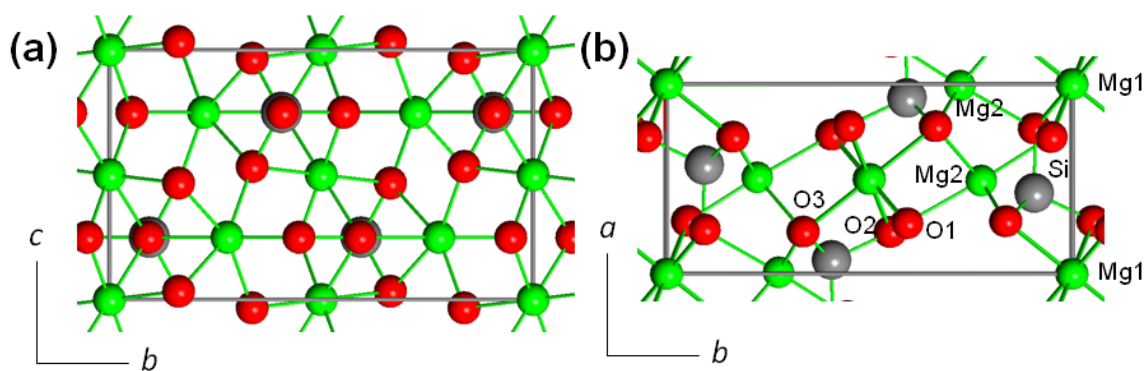

Fig. A1. Bulk structure illustrations of olivine. (a) and (b) are the views looking down the *a* and *c* axes, respectively. Metal atom occupies two sites, and coordinates with six oxogen atoms to form an octahedron. Si occupies one site, and is the center of a tetrehedron. Metal=green spheres, Si=grey spheres, O=red spheres, produced by XTALDRAW®.

(2) Forsterite(010) surface termination

Fig. A2 shows the side view of forsterite(010) with both the dipolar (dashed line (1)) and the non-dipolar (dashed line (2)) indicated. As discussed in Chapter 2, all DFT calculations of H_2O adsorption are done using the more stable non-dipolar termination that preserves the SiO_4 tetrahedra.
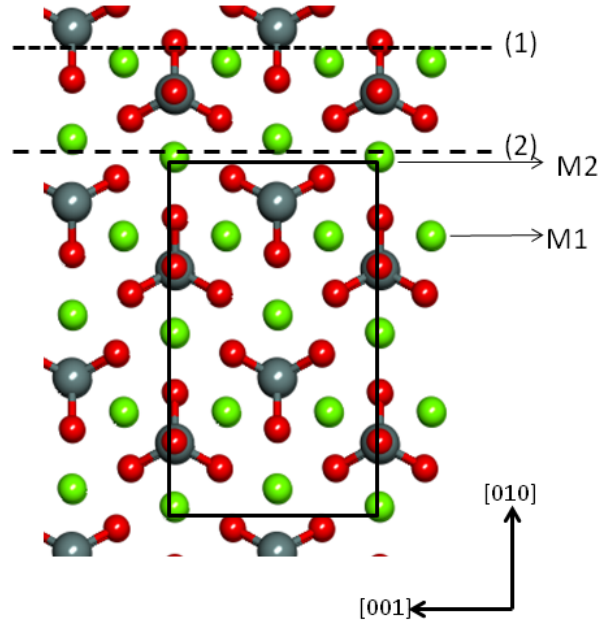

Fig. A2. Side view of forsterite(010). Black frame indicates the size of 1 × 1 unit cell along the [100] direction. Separation at dashed line (2) produces a non-dipolar surface, while line (1) would break Si-O bond. M1 and M2 are two Mg atom sites in forsterite. Mg=green spheres, Si=grey spheres, and O=red spheres.

(3) Effect of $+U$ corrections on bulk lattice parameters

To determine the effect of $+U$ corrections,, we have also calculated the lattice constants for the end members containing transition metals (TM) using just PBE-D3 (no $+U$). Table A1 lists the lattice constants for our PBE-D3 ($U = 0$) (in bold) for three TM-containing end members, as well as experimental values and calculated values from Kerisit et al. (2013). Comparing the lattice parameters in Table A1 with those reported in

Table 2.1 of Chapter 2, we find that with (without) $+U$ we obtain slightly larger (smaller) lattice constants versus experiment values. Comparison with Kerisit et al. (2013) indicates the larger difference in lattice parameters is due to D2 versus D3 treatment of dispersion with the D3 version giving smaller lattice constants due to stronger dispersion interactions.

Table A1. Calculated lattice constants of TM-containing end members in this study without U parameter (U=0).

	Experiment			Calculated, PBE-D3, U=0				Kerisit et al.*, Calculated, PBE-D2, U=0		
	a (Å)	b (Å)	c (Å)	a (Å)	b (Å)	c (Å)	Vol. diff(%)	a (Å)	b (Å)	c (Å)
Mn_2SiO_4	4.902	10.596	6.257†	**4.907**	**10.516**	**6.245**	-0.84	4.947	10.632	6.360
Fe_2SiO_4	4.818	10.471	6.086‡	**4.967**	**10.200**	**5.899**	-2.66	4.745	10.489	6.151
Co_2SiO_4	4.780	10.298	5.999§	**4.849**	**10.148**	**5.891**	-1.83	4.843	10.321	6.041

*(Kerisit et al., 2013), †(Fujino et al., 1981), ‡(Smyth, 1975), §(Tamada, O., Fujino, K., Sasaki, 1983)

(4) Slab thickness testing

The appropriate slab thickness was confirmed by surface energy calculations shown in Table A2. The upper half of the slab is relaxed while the lower half of the slab is fixed. The slab thickness is increased from one unit cell to two unit cells, and the surface energy (σ) did not deviate to a larger extent. Therefore, one unit cell thickness is secured for subsequent calculations.

Table A2. Surface energy of forsterite(010) for different slab thickness.

Dimension	Slab thickness(Å)	move/fix atoms	E_{slab} (eV)	A (surface area, $Å^2$)	σ (eV/$Å^2$)	(J/m^2)
2×2	10.197	half/half	-774.06	28.58	0.39	6.30
2×2	20.394	half/half	-1571.42	28.58	0.38	6.07

Note: $\sigma = (E_{slab} - nE_{bulk})/2A$, including two sides of the surface.

Section II. Structure of adsorbed water on olivine(010) surface

Table A3 summarizes structural information for the adsorbed water along with bond lengths between H_2O and the relevant surface atoms for all five end-members of olivine examined in this study. Kerisit et al. (2013) did not report the water structure details and therefore those values cannot be compared, but the values for Me-Ow and Hw-Ox from their study are reported in Table A3 for comparison. For most of the surfaces, our values are similar to those reported by Kerisit and co-workers (within 0.05 Å). The one exception is the 'pointing-down' H_2O configuration on the Ca-olivine surface. For this configuration, we find a binding energy that is 19.3 kJ/mol weaker than that reported by Kerisit et al. (2013). Reflecting this difference in binding energy, they have a shorter Ca-Ow distance of 2.48 Å versus our value of 2.57 Å in this study. For the 'flat-lying' configuration, we have good agreement with their study regarding the bond lengths of both Ca-Ow and Hw-Ox.

Table A3. Structural data for the two local minima H_2O configurations on the five end-member olivine(010) surfaces examined in this study. Available data from the study of Kerisit et al. (2013) is also shown.

	This study†, 0.125 ML				Kerisit et al. (2013), 0.5 ML	
	Pointing-down molecular H_2O on olivine(010) surface, Fig. 2.2a, b					
(010) surfaces	H-O bond distance	H-O-H angel	Me-Ow bond distance	Hw-Ox bond distance*	Me-Ow bond distance	Hw-Ox bond distance*
forsterite	0.97 Å, 1.02 Å	103.3°	2.11 Å	1.71 Å	2.09 Å	1.70 Å
Ca-olivine	0.97 Å, 1.10 Å	104.3°	2.57 Å	1.41 Å	2.48 Å	1.60 Å
Tephroite	0.97 Å, 1.01 Å	103.8°	2.25 Å	1.76 Å	2.29 Å	1.78 Å
fayalite	0.97 Å, 1.00 Å	105.2°	2.17 Å	1.78 Å	2.18 Å	1.76 Å
Co-olivine	0.97 Å, 1.01 Å	104.5°	2.11 Å	1.79 Å	2.12 Å	1.73 Å
	Flat-lying molecular H_2O on olivine(010) surface, Fig. 2.2c, d					
forsterite	1.00 Å	103.7°	2.10 Å	1.99 Å	2.06 Å	1.94 Å
Ca-olivine	1.00 Å	109.4°	2.50 Å	1.86 Å, 1.89 Å	2.46 Å	1.84 Å, 1.85 Å
Tephroite	0.99 Å	105.7°	2.23 Å	2.14 Å, 2.16 Å	2.24 Å	2.12 Å, 2.13 Å
fayalite	0.99 Å	105.1°	2.20 Å	2.18 Å	2.17 Å	1.99 Å, 2.01 Å
Co-olivine	0.99 Å	104.0°	2.11 Å	2.03 Å, 2.19 Å	2.10 Å	1.97 Å, 1.99 Å

*The closest Ox to the Hw.
†U=5, J=1 results.

Similar information to Table A3 is presented in Table A4 for water on the doped forsterite(010) surface.

Table A4. Structural data for the two local minima of molecular water on the doped forsterite(010) surfaces examined in this study.

Dopant		H-O bond distance	H-O-H angel	Me-Ow bond distance	Hw-Ox bond distance*
Pointing-down, Fig. 2.2a, b					
AE	Ca-	0.97 Å, 1.03 Å	102.8°	2.44 Å	1.59 Å
	Sr-	0.97 Å, 1.03 Å	104.6°	2.61 Å	1.56 Å
	Ba-	0.97 Å, 1.02 Å	103.0°	2.86 Å	1.60 Å
TM	Cr-	0.98 Å, 1.01 Å	103.0°	2.13 Å	1.61 Å
	Mn-	0.97 Å, 1.02 Å	103.3°	2.22 Å	1.66 Å
	Fe-	0.97 Å, 1.01 Å	104.1°	2.19 Å	1.73 Å
	Co-	0.97 Å, 1.01 Å	103.9°	2.13 Å	1.74 Å
	Ni-	0.98 Å, 1.01 Å	103.6°	2.11 Å	1.73 Å
Flat-lying, Fig. 2.2c, d					
AE	Ca-	1.00 Å	104.8°	2.41 Å	1.80 Å
	Sr-	1.01 Å	105.5°	2.58 Å	1.76 Å
	Ba-	1.01 Å	106.7°	2.85 Å	1.73 Å
TM	Cr-	0.99 Å	104.8°	2.33 Å	1.94 Å
	Mn-	1.00 Å	104.2°	2.21 Å	1.90 Å
	Fe-	0.99 Å	103.8°	2.22 Å	1.99 Å
	Co-	1.00 Å	103.8°	2.13 Å	2.01 Å
	Ni-	0.99 Å	104.1°	2.09 Å	2.03 Å

*The closest Ox to the Hw.

In addition to the surface unit cell size of 2×2 that is discussed in the main text, we have also investigated one water molecule adsorption on a 2×3 surface unit cell to test if the local dopant-water interactions are effect by surface cell size (i.e. is 2×2 cell size sufficient to ensure isolated dopant-water interactions). We doped Ca and Fe atoms on the 2×3 surface by replacing one out of six Mg atoms on the top layer of the 2×3 surface. Fig. A3 shows the pointing-down configuration of water molecule on the 2×3 pure forsterite, Ca-, and Fe-doped (010) surfaces, respectively. Table A5 summarizes the adsorption energy and relevant structural data of adsorbed water molecule on both surface unit cells. The adsorption energy difference is negligible (~ 0.03 eV/molecule) and confirms that the 2×2 surface is sufficient to model local dopant-water interactions.
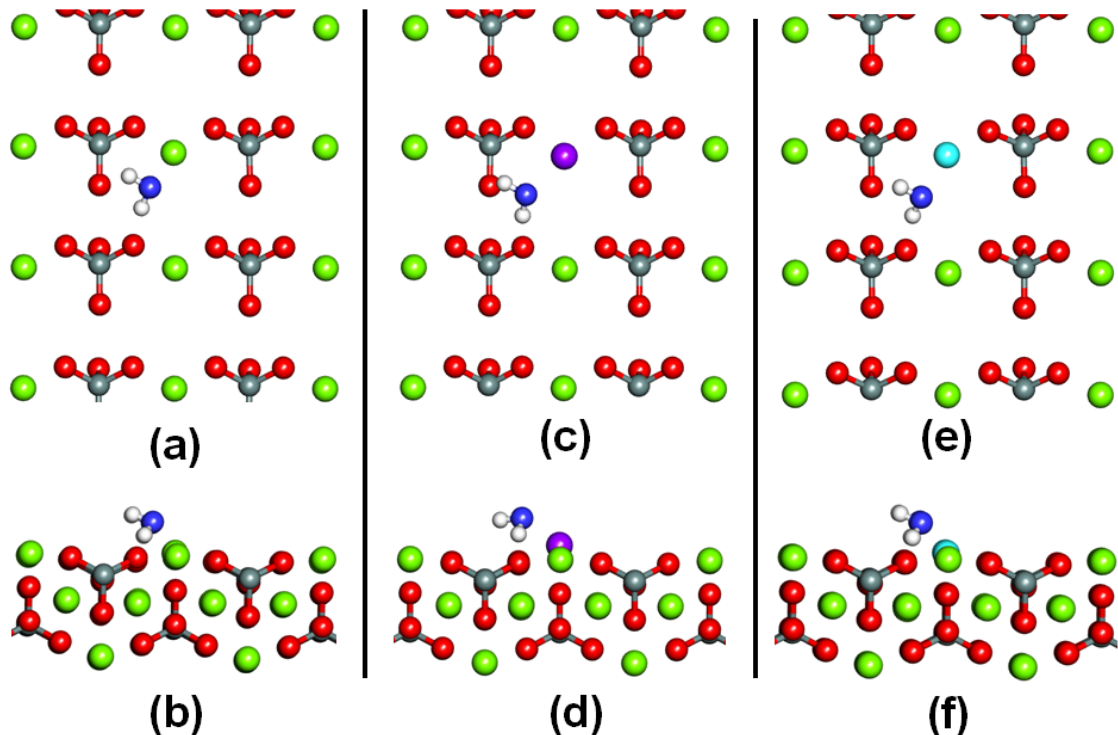
Fig. A3.Top (a, c, e) and side (b, d, f) views for molecular water on 2×3 pure (a, b), Ca-doped (c, d), and Fe-doped forsterite(010) surface (e, f). Purple=Ca, light blue=Fe.

Table A5. Bond information and E_{ads} comparion on 2×2 and 2×3(010) surfaces.

		E_{ads} (kJ/mol)	Me-Ow (Å)	Hw-Ox (Å)	H-O-H (°)
Pure forsterite	2×2	-138.1	2.11	1.71	103.3
	2×3	-138.0	2.11	1.73	102.8
Ca-doped	2×2	-125.3	2.44	1.59	102.8
	2×3	-125.2	2.45	1.62	101.0
Fe-doped	2×2	-100.8	2.19	1.73	104.1
	2×3	-101.1	2.20	1.72	103.4

Section III. Charge of cations versus E_{ads}

Fig. A4 plots water adsorption energy versus DDEC charge of the metal cations that interact with the molecular water. Fig. A4 can be compared with the similar figure with Bader charges in Chapter 2 (Fig. 2.3). There is no evident trend that could group all metal atoms/end members together; however, we can see a boundary that segregates the

AE and TM elements. Alkaline earth metals on the right halfside (in shadow) have higher charge than the TM dopants. Results of DDEC charge is slightly different from that of Bader charge, but they both suggest the AE cations have higher charge than TM cations, but cation charge is not sufficient to capture the trend in water adosrption energy on different olivine surfaces.
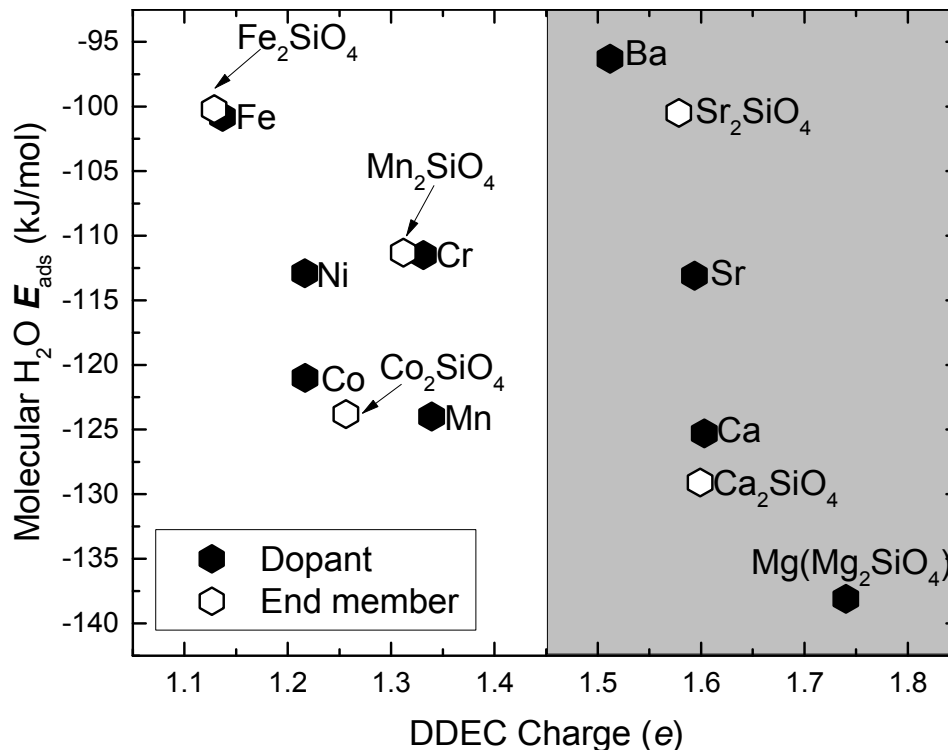
Fig. A4. Molecular water adsorption energy on various olivine(010) and doped forsterite(010) surfaces versus the DDEC charge of the metal cation on the bare surface. No single trend can be derived for all the dopants and end members, but a clear separation can be seen between AE and TM regarding their charge.

Section IV. DOS and COHP

(1) Pointing-down H_2O configuration on doped forsterite(010) surfaces

Figs. A5 and A6 present the Ox-Hw hydrogen bonding and Me-Ow bond, respectively, regarding their density of states (DOS) and Crystal Orbital Hamilton Population (COHP) plots for the bonds. The two figures include all the doped surfaces in this study. For the corresponding end members, their COHP/DOS plots are similar to the scenarios on the doped surfaces; thus their plots are not presented for clarity. For the hydrogen bonding (Ox-Hw, Fig. A5), the $3a_1$ and $1b_2$ are the major responsible orbitals. For the Me-Ow bond in Fig. A6, TM-Ow shows stronger charge transfer than AE-Ow bond, and $3a_1$ is the major contributor for the bonding formation. There is antibonding feature with each Me-Ow bond, as the lone pair $1b_1$ accepts electrons from the surface and Pauli repulsion occurs.
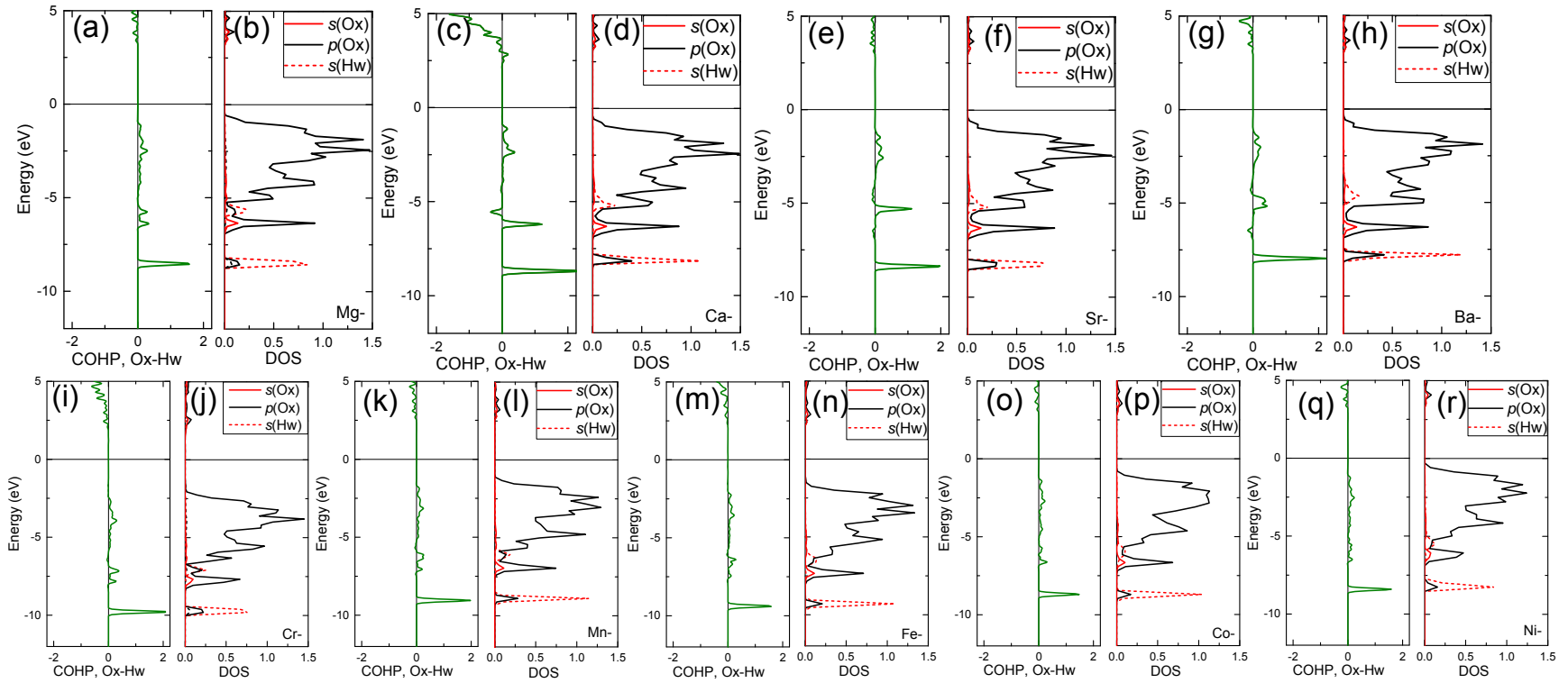
Fig. A5. COHP and DOS plots for Ox-Hw bond on the (010) surfaces of forsterite (a, b), Ca-doped (c, d), Sr-doped (e, f), Ba-doped (g, h), Cr-doped (i, j), Mn-doped(k, l), Fe-doped (m, n), Co-doped (o, p), and Ni-doped (q, r).
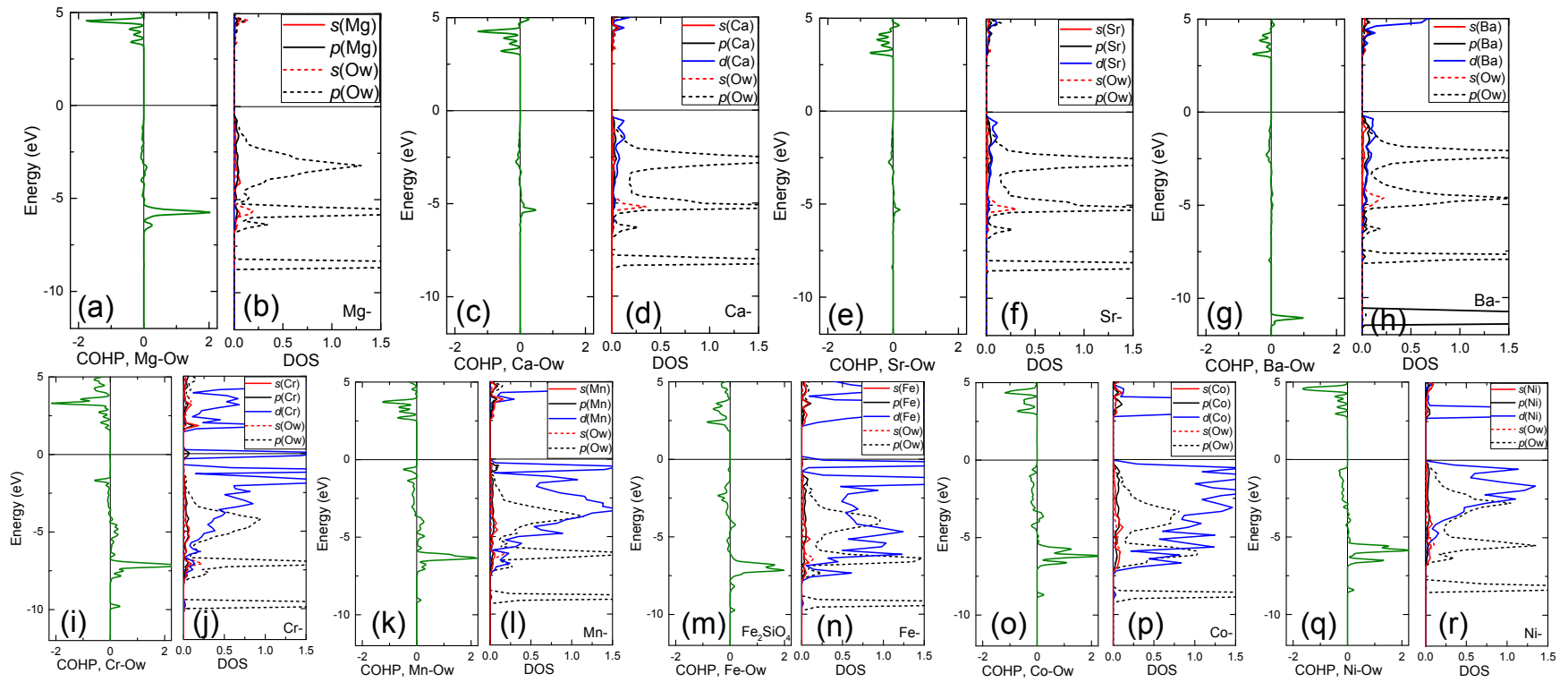
Fig. A6. COHP and DOS plots for Me-Ow bond on the (010) surfaces of forsterite (a, b), Ca-doped (c, d), Sr-doped (e, f), Ba-doped (g,h), Cr-doped (i, j), Mn-doped(k, l), Fe-doped (m, n), Co-doped (o, p), and Ni-doped (q, r).

(2) Flat-lying configuration on forsterite(010) surface

We take the flat-lying configuration of water molecule on pure forsterite(010) surface as an example. Fig. A7 shows the COHP and DOS information for Mg-Ow and two Ox-Hw bonds. Similar to the Mg-Ow bond in pointing-down configuration, the major responsible MO for bonding is also $3a_1$, generating an iCOHP value of +0.89, close to the +0.90 for pointing-down configuration. The two hydrogen bonding show similar bonding information as expected, and used the same MO ($3a_1$ and $1b_2$) as in pointing-down configuration. The iCOHP value is +0.58 (flat-lying) vervus + 1.13 (pointing-down). The total iCOHP of the two hydrogen bonds in flat-lying configuration is equivalent to the iCOHP of one hydrogen bond in pointing-down configuration.
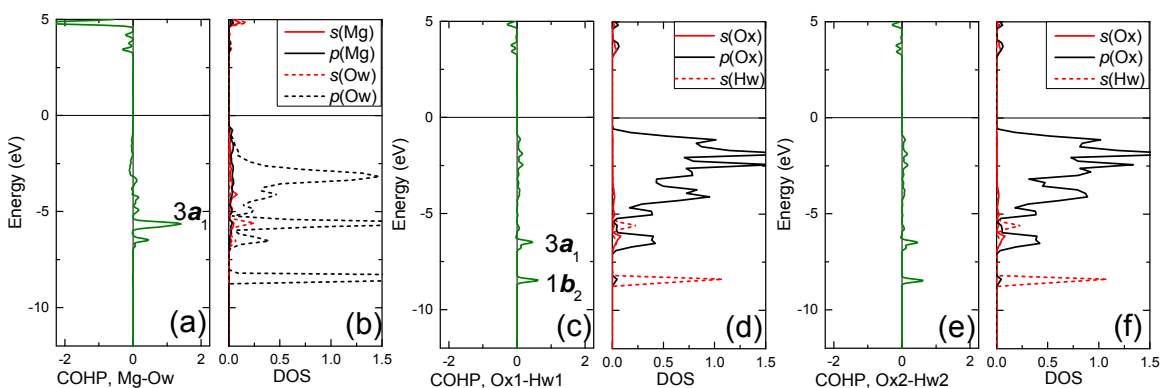
Fig. A7. COHP and DOS plots for Me-Ow bond (a, b) and Hw-Ox bonds (c ~ f) in its flat-lying configuration on forsterite(010) surface.

(3) Water molecule on Pt(111) surface

We calculated water molecule adsorbed on Pt(111) surface using PBE-D3. The two configurations, flat and upright, are shown in Fig. A8, along with the corresponding COHP/DOS information. The E_{ads} for the two configurations are -0.46 eV (-0.35 eV by Michaelides et al. 2003, PW91 method) and -0.13 eV, respectively; thus the flat

configuration is more favorable. In the flat configuration, we can see the $3a_1$ and $1b_1$ are both responsible for the bonding in Fig. A8a, b, with antibonding occurring in the $1b_1$ orbital. Michaelides et al. (2003) claimed that $1b_1$ orbital is responsible for the flat configuration. In the upright configuration, we can see the $3a_1$ orbital is the major component for the covalent bonding, also with antibonding in the $1b_1$ orbital, consistent with what Michalides et al. (2003) claimed for upright configuration. We have identified the same charge transfer direction as Michaelides et al. (2003) indicated, i.e., water molecule loses electron to the surface.
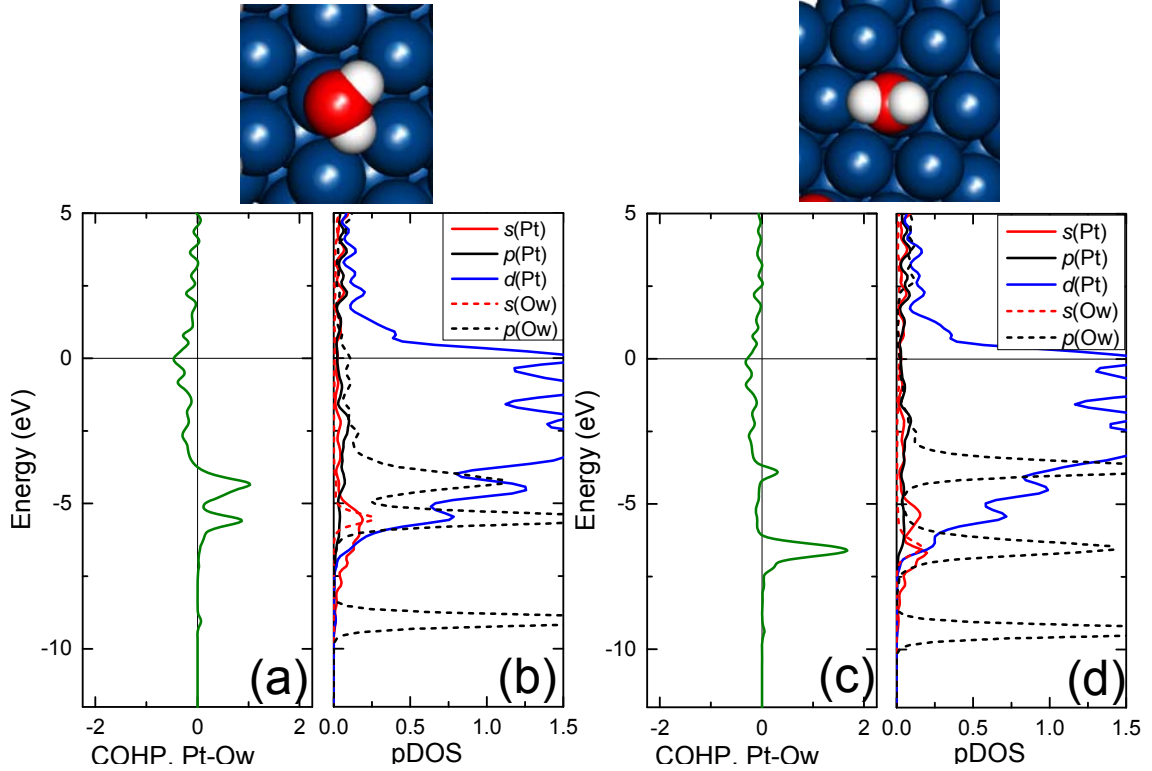
Fig. A8. COHP/DOS information for flat (a, b) and upright (c, d) water molecule on Pt(111) surface.

(4) COHP and DOS information for Ow-Hw bond: Effect of adsorption on forsterite(010) surface

As noted in the text, water undergoes substantial charge polarization when adsorbed on AE olivine surfaces. In this section, we present information on the Ow-Hw bond that illustrates the effect of this charge polarization on water MOs. The two Ow-Hw bonds were examined before (Fig. A9a ~ d) and after (Fig. A9e ~ h) the adsorption on a 2 × 2 forsterite(010) surface. In the pointing-down configuration, Fig. A9e, f are for the bond that points to the surface. The MO $1b_1$ is composed of the lone pair, thus was not involved in bonding. The iCOHP values for the two Ow-Hw bonds before the adsorption are +8.04 and +7.99. After the adsorption, we can see the antibonding feature (Fig. A9e)

occurring in the lone pair, which is similar to the Ox-Hw bond we have analyzed in the main text, due to the electron donation from surface to the water molecule. This effect thus weakens and lengthens the Ow-Hw bond that points to the surface. The two iCOHP values for Ow-Hw bonds after adsorption are +7.13 and +7.87. The bond strength of Ow-Hw1 is decreased as expected as it was lengthened and Hw1 interacts with Ox.
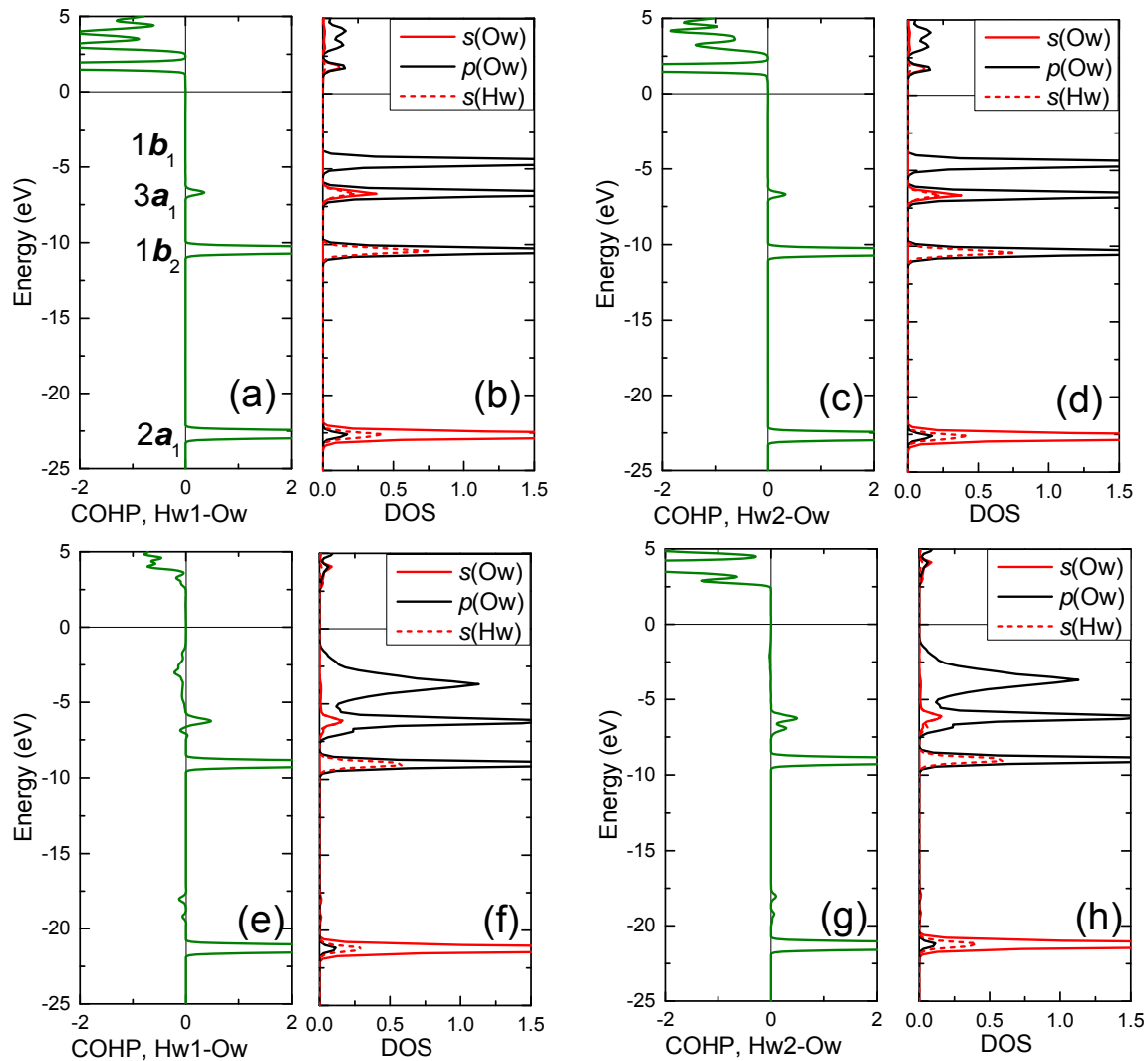
Fig. A9. COHP and DOS analysis for the Ow-Hw bonds in the water molecule. (a), (b) and (e), (f) represent Ow-Hw1 bond (pointing down towards Ox surface atom upon adsorption) before and after adsorption, respectively. (c), (d) and (g), (h) represent Ow-Hw2 bond (pointing away from the surface upon adsorption) before and after adsorption, respectively.

(5) Water on Ca-doped forsterite restricted to geometry of water on forsterite(010) surface

As noted in Chapter 2, of the AE olivine surfaces forsterite(010) shows the strongest covalent bonding consisting of bonding involving the $3a_1$ H_2O MO and some

minor antibonding involving the $1b_1$ MO. To understand the source of the large drop in covalent bonding between Mg and the other AE cations, we calculated the COHP/DOS for H_2O adsorbed on Ca-doped forsterite(010) but in the same configuration as on undoped forsterite(010). This system is setup by just taking the finale relaxed H_2O/forstertite(010) system and replacing the surface Mg atom with Ca and performing a single-point DFT calculation. The resulting COHP/DOS plots are shown in Fig. A10. Unlike for forsterite(010) (see Fig. 2.6a,b in Chapter 2), we observe no substantial bonding feature associated with the $3a_1$ orbital, but a large antibonding feature is present with the $1b_1$ orbital. From the DOS we can also see that the antibonding feature is associated with Ca-s, p, d states in the -5 to 0 eV range that are not present for Mg (see Fig. 2.6a,b in Chapter 2). We associate this large antibonding feature with Pauli repulsion due to short Ca-Ow distance in this configuration, which when the system is allowed to relax pushes the H_2O molecule away and results in the weak covalent bond for Ca-doped forsterite and other AE olivine surfaces.
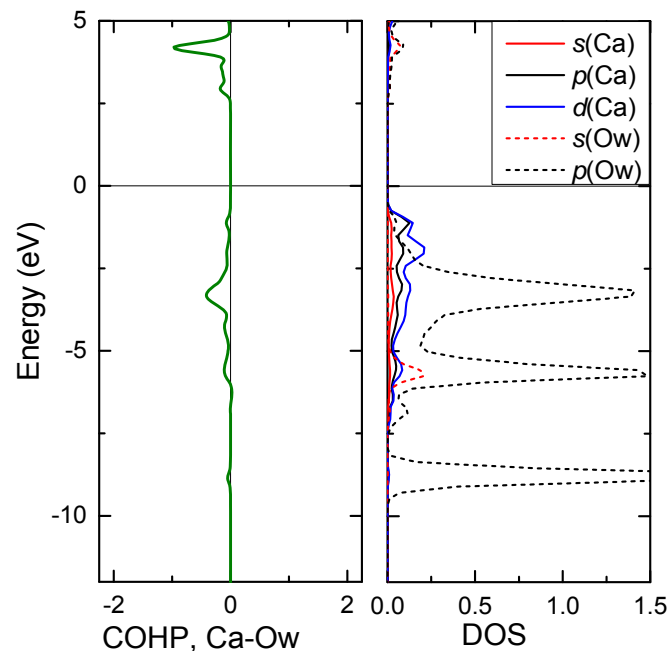
Fig. A10. COHP/DOS information for an artificial Ca-Ow bond in a relaxed H_2O/forsterite(010) structure. Significant antibonding feature is caused by the shorter Ca-Ow bond distance.

Appendix B: Structure and Dynamics of Water on Forsterite Surface

1. Water molecules in the adsorbed layer and first layer

To study the behavior of water molecules residing at different distances from the forsterite surface, ten representative molecules from the adsorbed layer and ten from the first layer were selected, based on the criteria that they spend considerable time within the layer at a stretch. We identified the maximum time of residence in corresponding layers that could be achieved for the two layers was 15 ps. Fig. B1 plots the trajectories of the two layers of the selected water molecules, in addition to the free water molecules to better illustrate where they reside on the surface and how they are restricted by different confinements.
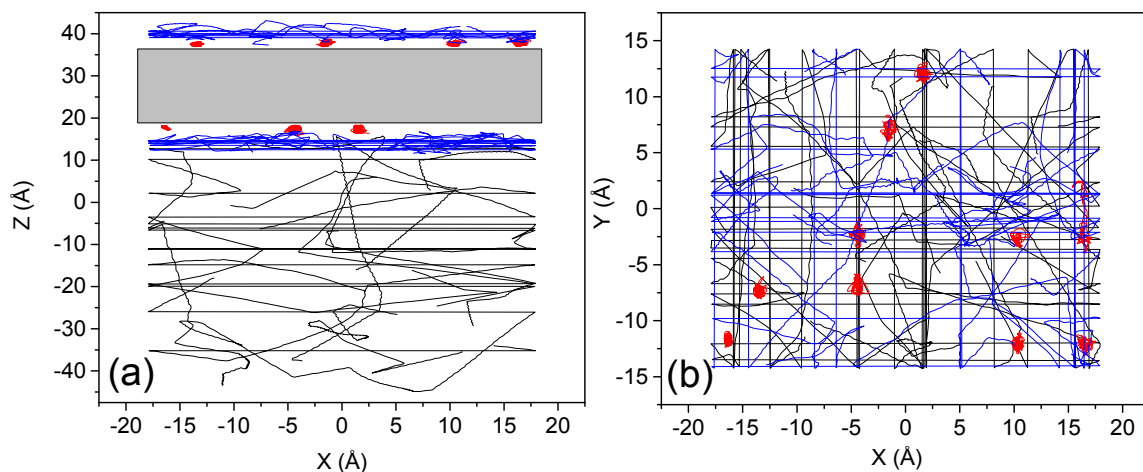
Fig. B1. Trajectories of representative molecules from the adsorbed layer (red), first layer (blue) and free water (black) for a duration of 15 ps. Molecules in the adsorbed layer can be seen to be severely restricted in X-Y plane, shown by (b). The forsterite slab is shown as a grey rectangle in (a).

Properties of molecules from different layers can be calculated from their 15 ps trajectories. Mean squared displacements (MSD) were calculated from the short trajectories for different layers. In the planar MSD (Fig. 3.9 in the main text), it was found that the ballistic regime extends up to 20 ps. Therefore, we plotted the relationship between MSD and t^2 instead, and extracted the proportionality constants between different layers and compared them. Fig. B2 show the overall MSD (a) for different layers as well as the planar MSD (b), i.e., to remove the effect from the direction normal to the surface as the two near-surface layers are restricted to the surface plane. The time range indicated in Fig. B2 (15 ~ 20 ps^2) is used to calculate the slope ratios.
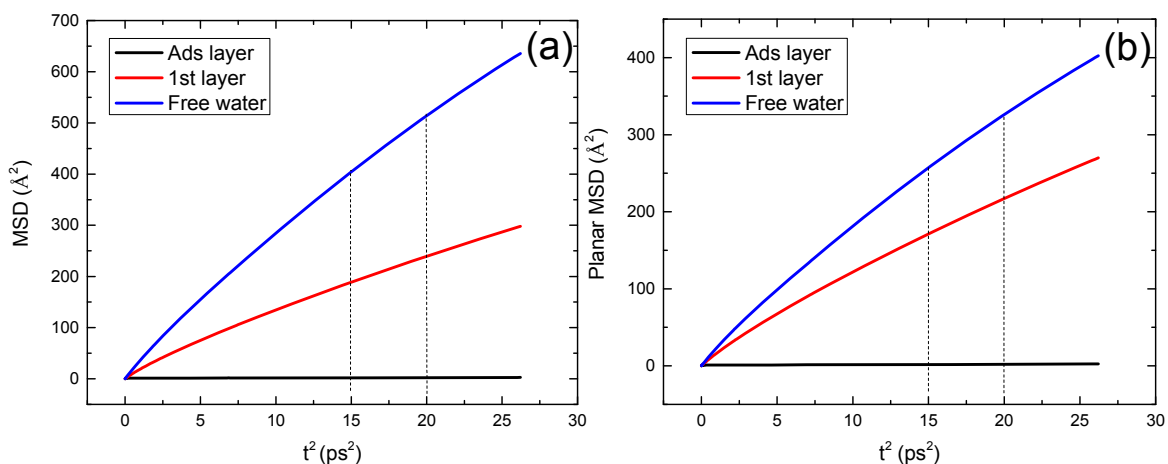
Fig. B2. Relationship of MSD vs t^2 using the trajectories of ten molecules from different layers for a duration of 15 ps, as molecules in such a short duration show ballistic behavior, instead of diffusion behavior.

The ratios of the slopes of MSD vs t^2 curves for molecules in different regions are tabulated in Table B1. It can be seen that the adsorbed layer water molecules are severely restricted as compared to the free water, while the water in the first layer is restricted but exhibits the same order of magnitude displacements as the free water. The adsorbed water

is bound to the forsterite surface and experiences strong binding forces. These water molecules seem to screen the water molecules in the first layer from the strong adsorption forces of the forsterite surface, thus making the first layer water molecules relatively free.

Table B1. Slope ratios derived from MSD vs t^2 relation plots for different layers of water molecules.

	MSD vs t^2, slope ratio	Planar MSD vs t^2, slope ratio
Free water : First layer	2.2	1.5
Free water : adsorbed layer	327.5	231.6
First layer : adsorbed layer	150.7	155.3

2. Kinetic energy

As stated above, the approach of comparing the slopes of MSD vs t^2 plots has a limitation. We also have calculated the kinetic energies (KE) of the selected molecules during 15 ps. The ratio of KE in different regions overcomes the limitation in the other approach by avoiding space dependent variables. Kinetic energy ratio used the averaged value from each layer, shown in Table B2.

Table B2. Kinetic energy ratios between different layers of water molecules for a duration of 15 ps.

	Kinetic energy ratio
Free water : First layer	1.2
Free water : adsorbed layer	2.2
First layer : adsorbed layer	1.9

3. Orientational Distribution Function

Fig. B3 displays the orientation distributions of the surface molecules (in the adsorbed layer and first layer region) along three directions. We used the angle between the position vector of Ow in the COM frame and the three Cartesian directions. For reference, we have added the isotropic orientational distribution curve that is the expected distribution in an ideal situation with no preferred orientation (in black) in the figure. In Fig. B3a, b, and c, there is no orientational preference at any angle. Therefore, we can infer that water molecules undergo an isotropic rotational motion on the hydroxylated Fo(010) surface.
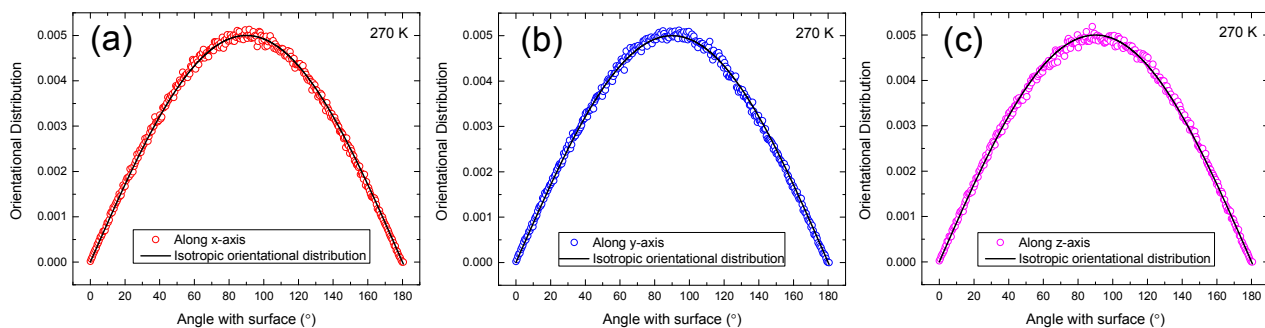
Fig. B3. Orientational distribution function using Ow in the center of mass frame to observe its angle with the Cartesian coordinates. (a) angle distribution with x-axis, (b) with y-axis, and (c) with z-axis. The black line in each figure is the isotropic orientational distribution which is used to weigh against the preferential orientation of the molecules. Z-axis is the direction normal to the surface in this study.

138

Appendix C: Vibrational Behavior of Water Adsorbed on Forsterite (Mg$_2$SiO$_4$) Surfaces

1. Synthetic forsterite nanoparticle characterization

The sample provided by Oak Ridge National Laboratory (Anovitz et al., 2017) has been characterized by a series of techniques, including X-ray diffraction (XRD), scanning electron microscopy (SEM), transmission electron microscopy (TEM), N$_2$ adsorption for surface area. Our characterization work yielded consistent result as shown in Anovitz et al. (2017).

1.1 X-ray diffraction (XRD)

X-ray diffraction was performed on a PANalytical X'Pert PRO diffractometer. The instrument uses Cu Kα radiation and a scintillation detector. Powders were prepared in slurry and dispersed onto a zero-background silicon plate till being dried. XRD data were collected in the range of 5~70°2θ with a step size of 0.02° at the speed of 10s/step. Applied voltage for measurement is 45 kV and the current is 40 mA. Slit specifications used are 0.04 rad Soller slits, 10 mm beam mask, ¼″ divergence slit, and ½″ anti-scatter slit, sequentially on the incident beam side; whereas the diffracted beam side possesses nickel filter, 5.5″ anti-scatter slit and 0.04 rad soller slit. Fig. C1 shows the XRD pattern for the synthetic forsterite sample. Expect the mineral phase of forsterite, there is no other phase identified.
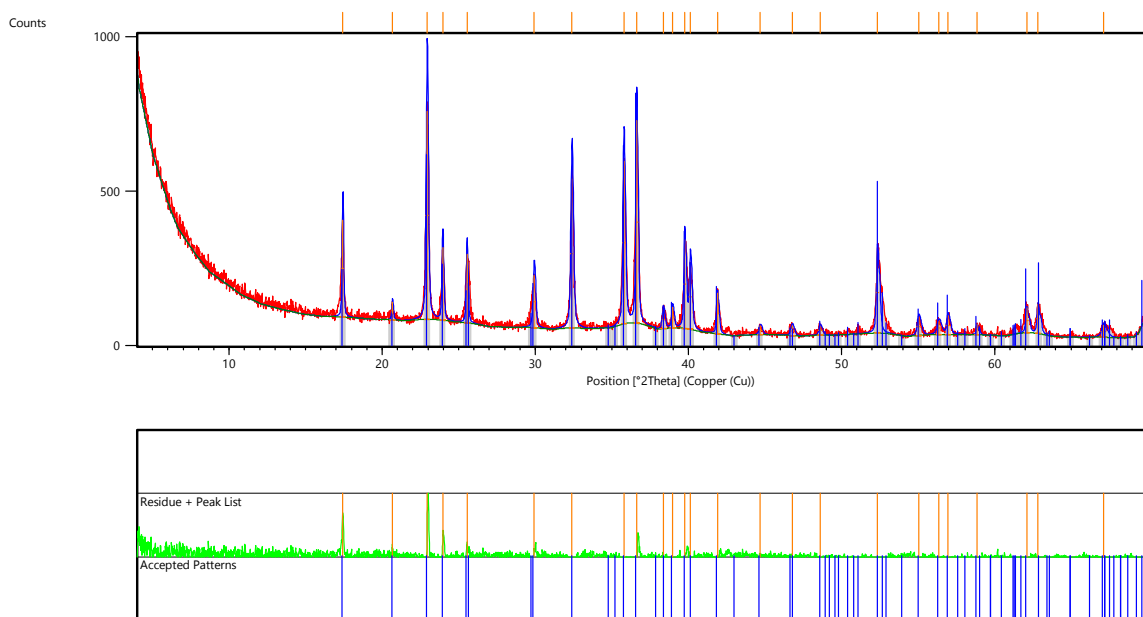
Fig. C1. XRD pattern of synthetic forsterite nanoparticle sample.

1.2 Scanning electron microscopy (SEM)

To prepare the sample mount for SEM, a small amount of powder is taken to mix with deionized water. The suspension is stirred in ultrasonic device for 30 minutes. Cu grids are used for suspension deposition. The Cu grid type with formvar film is used here. We used a glass slide with a stripe of double-side sticky carbon tape to stabilize the grids. The deposition is left for overnight for drying. Carbon coating is employed for subsequent imaging. SEM images were obtained using an FEI Quanta 250 Field Emission Gun (FEG) SEM. Images were acquired at 15 kV, spot sizes of 4.0 and 3.5, and working distances of 13.1 and 10 mm. Fig. C2 shows the SEM images of synthetic forsterite nanoparticle sample. The nanoparticles uniformly show flaky morphology in the SEM images. Particle sizes range from 100 ~ 1000 nm by scale bar.
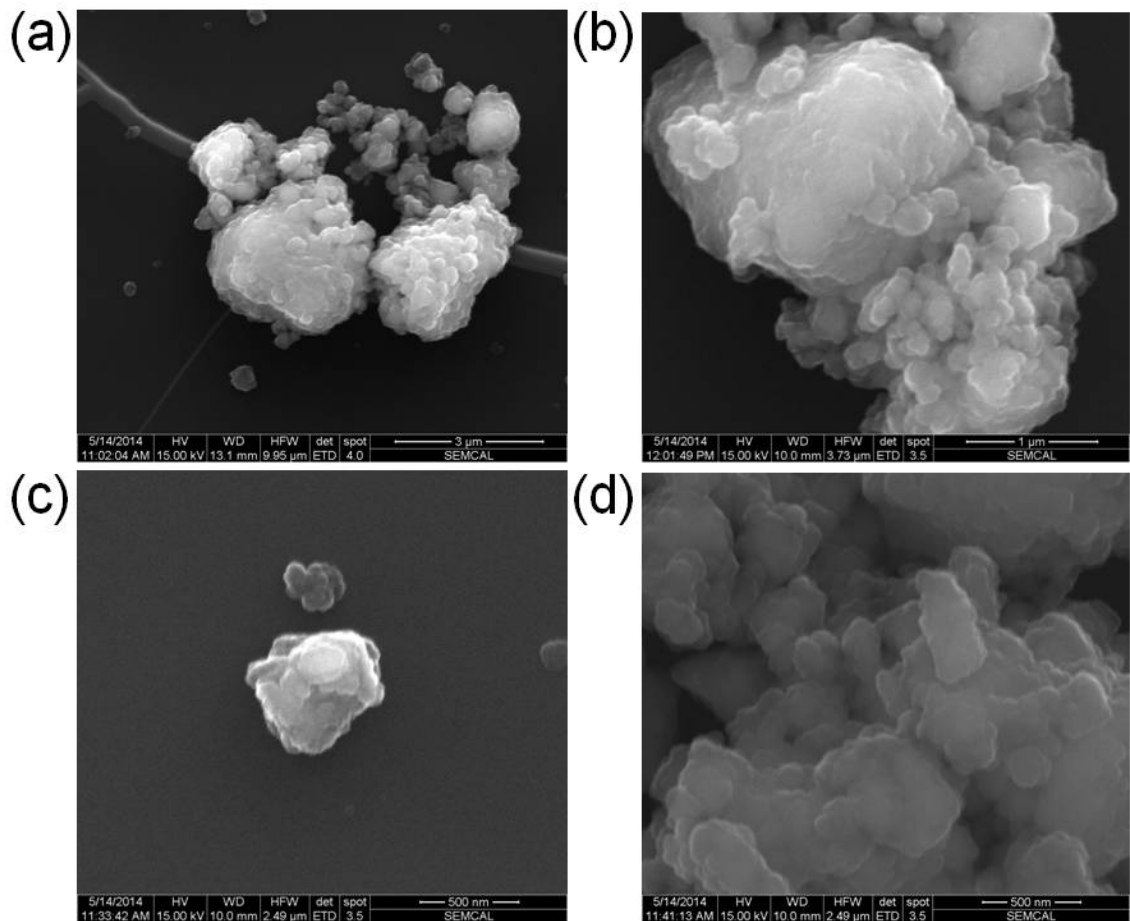
Fig. C2. SEM images of synthetic forsterite nanoparticles.

1.3 Transmission electron microscopy (TEM)

TEM imaging was performed using a FEI/Philips CM-200T. Deionized water was used to disperse the particles in centrifuge for 30 minutes. The suspension was deposited onto the copper grid for overnight drying, and was then carbon coated for subsequent imaging. Fig. C3 shows the TEM images of synthetic forsterite nanoparticle sample. We can identify the particles are formed in layers and the particle sizes vary from 100 nm to a few hundred nm. We also endeavored to identify the major crystal plane(s) of the forsterite nanoparticles by TEM, but it was not successful.

141
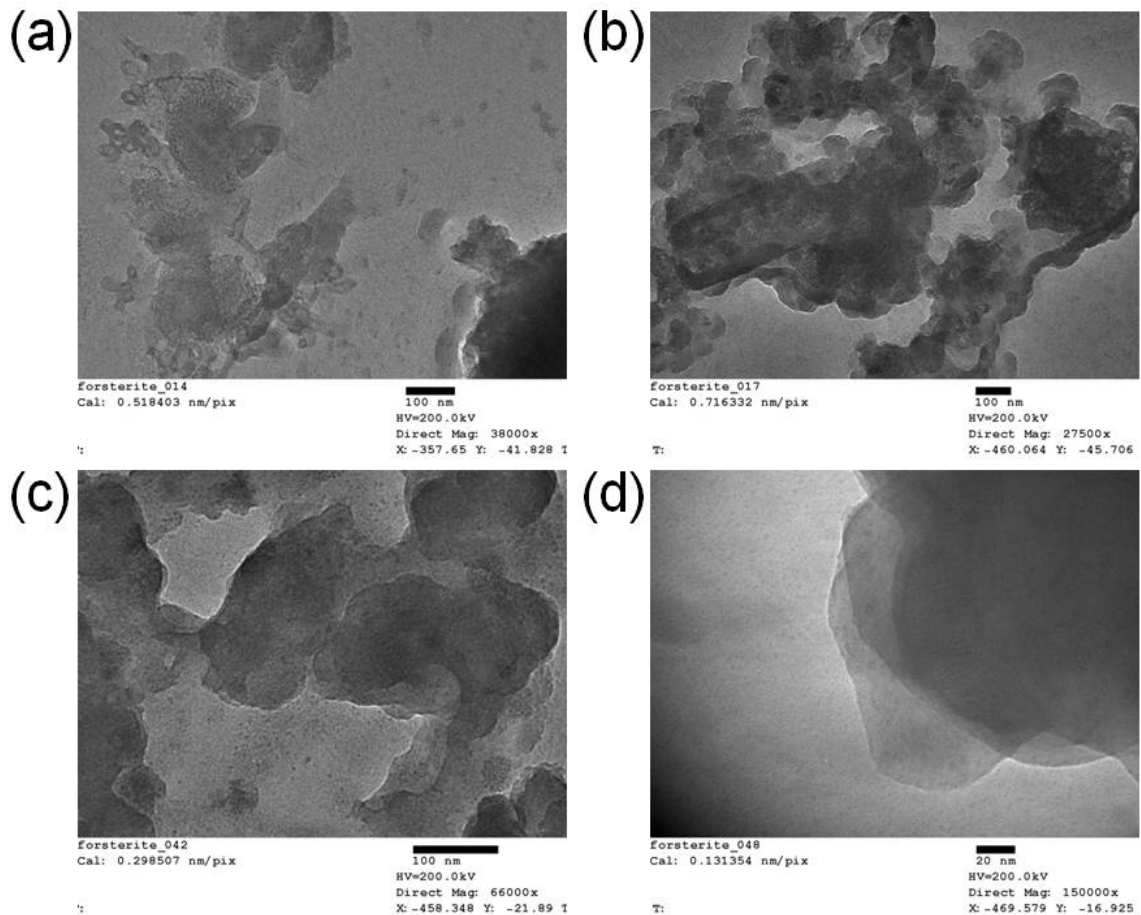
Fig. C3. TEM images of synthetic forsterite nanoparticles.

1.4 BET surface area

Surface area of the forsterite nanoparticles were determnined using an ASAP Micromeritics® 2020. Materials were degassed at 150°C for 10 hours to remove the impurities and gas inside the pores. Adsorption isotherm was carried out to the partial pressure of $P/P_0 = 0.3$ using nitrogen as the adsorbate. Surface area was obtained using the Brunauer-Emmett-Teller (BET) method. The BET surface area is determined as 25.1 $\pm$ 0.2 m^2/g.

2. INS experiment

Adding another monolayer of water onto S2 creates two monolayer on the partial hydroxylated surface (S3). The water film grows further. Again we can consider the differences S3 - S1 or S3 - S4 (Fig. C4). The latter (bottom of Fig. C4) still shows the discrete peaks around 525 and 720 cm^{-1} from the partial layer on the forsterite surface. The former is the same relatively featureless librational band already discussed in the case of the 1ML adsorbed water. There is little evidence that the water past the partial surface hydration interacts much with the surface. It appears to behave as bulk water held in place by weak physisorption on the hydroxylated (and hydrophilic) forsterite surface.
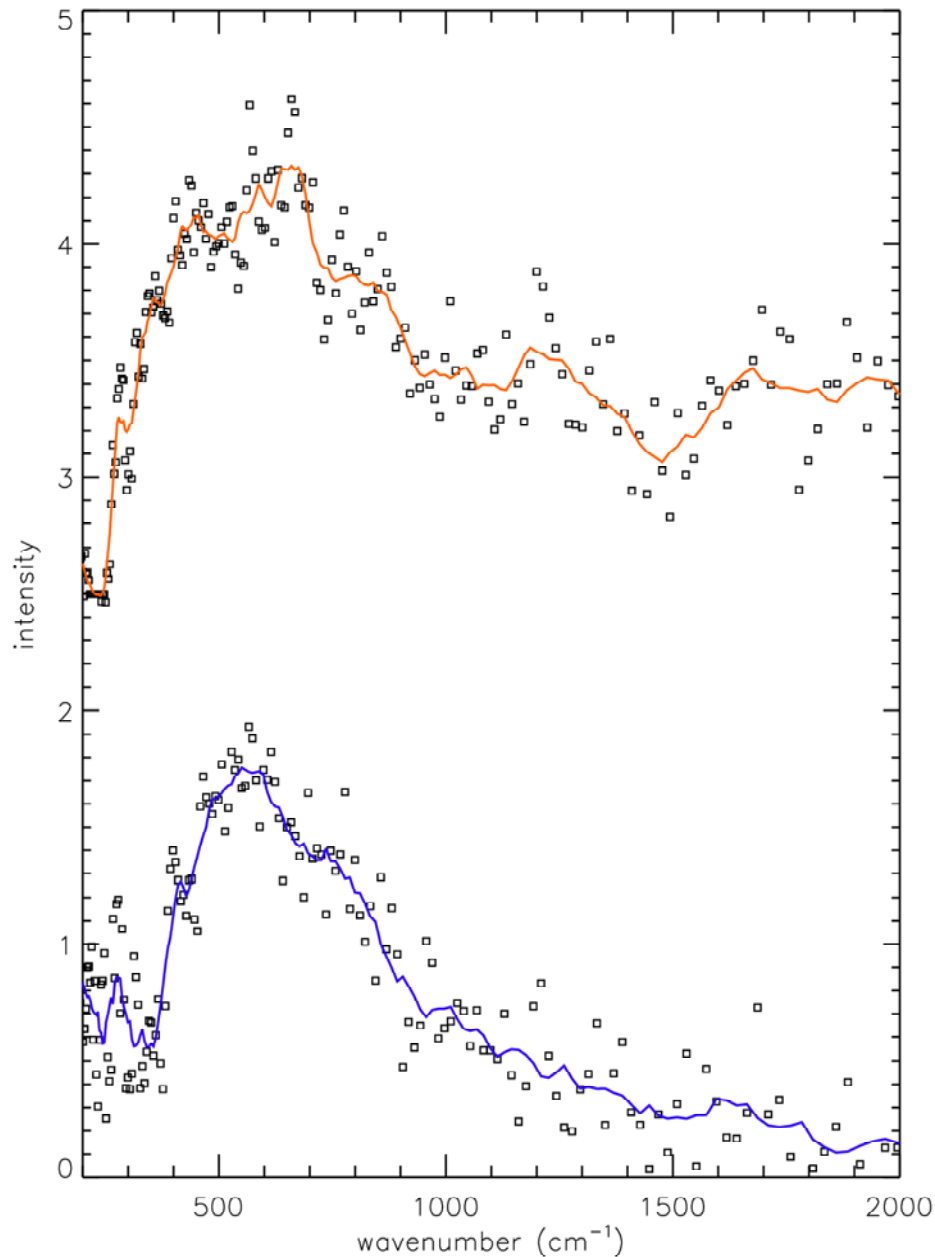
Fig. C4. The bottom curve is the difference between S3 (2ML of water adsorbed on S1) and S4 (dried sample). The partial layer is still visible in the data, but is more washed out compared to the similar curve in Fig. 4.2 in Chapter 4. This is not surprising considering that the signal from "free" water is larger with 2ML. The top curve is the difference spectrum between S3 and S1. This operation removes the partial layer and highlights the 2ML. The smooth character of the librational band is indicative of a disordered, liquid-like, weakly physisorbed monolayer. The solids lines are a smoothed version of the data.

The INS spectra for ice Ih and water are shown in Fig. C5. Data source is from the literature (Li, 1996).
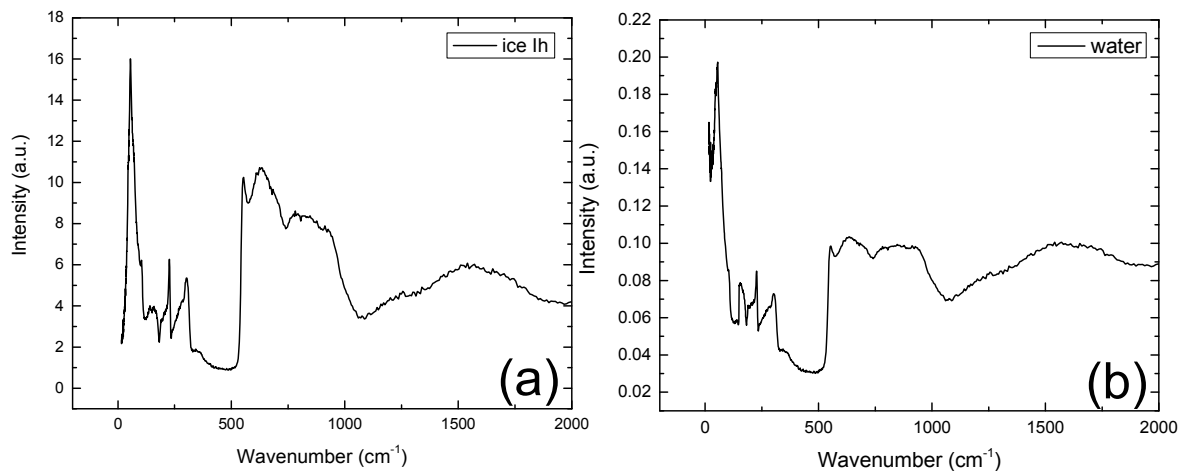
Fig. C5. INS spectra for ice Ih (a) and water (b).

3. MD simulations

3.1 Interface structure

Snapshots for water adsorbed on Fo(010) surface at four temperatures (298, 150, 50, and 10 K) are presented in Fig. C6, with a length of 100 Å along the *b* direction including the thickness of the slab.
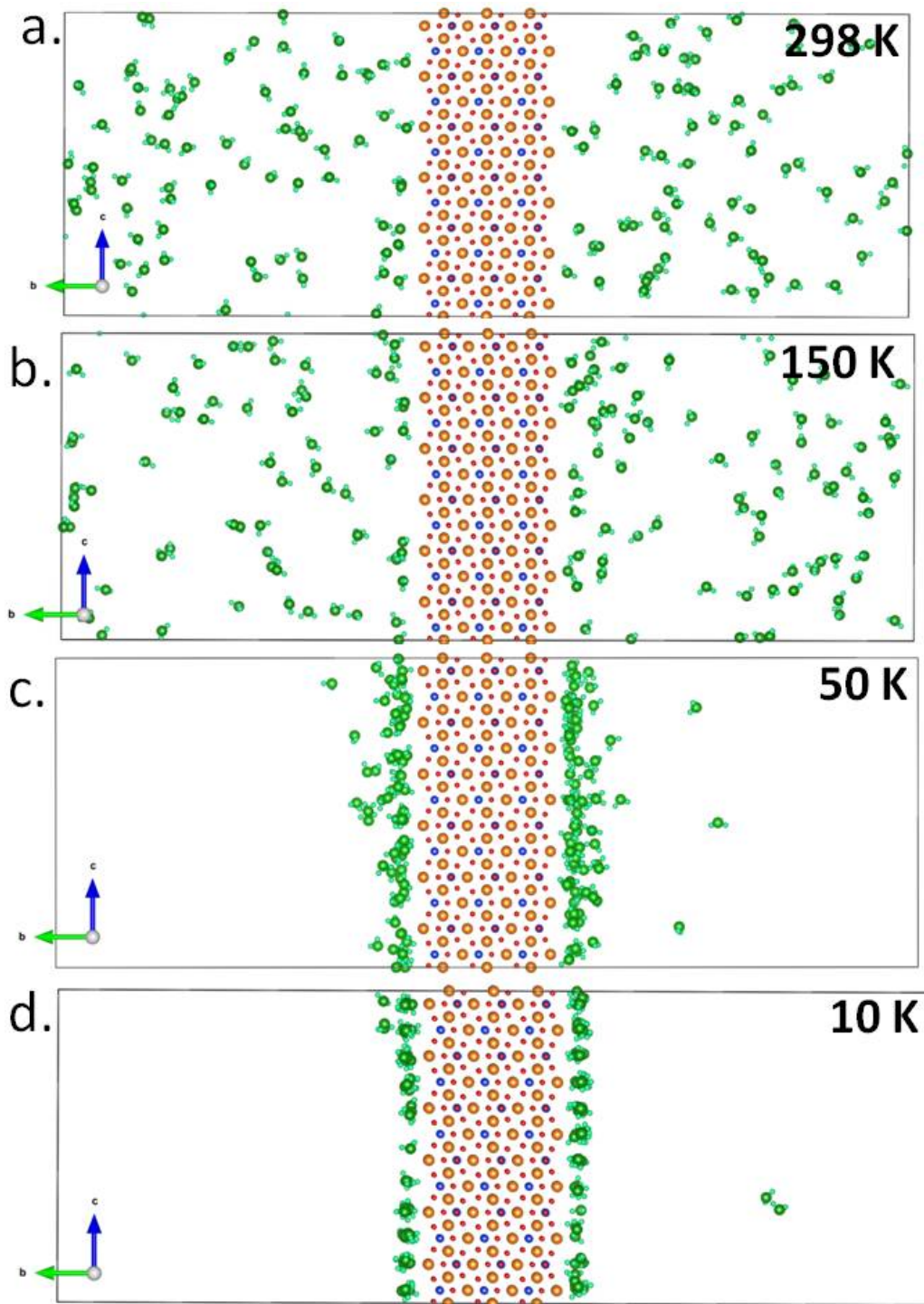
Fig. C6. Snapshots of simulation cells after equilibration of water molecules on Fo(010) surface at (a) 298 K, (b) 150 K, (c) 50 K, and (d) 10 K. In forsterite, orange=Mg; red=O; blue=Si.

Fig. C7 below shows the density profile of water molecules at the interface at four different temperatures using center of mass (COM) of the molecules. We can observe a significant effect of temperature that leads to the structural changes. In the near surface region (the solid surface is indicated by the gray area in Fig. C7), the density profiles exhibit sharper peaks for lower temperatures (10 K and 50 K) than for higher temperatures (150 K and 298 K). At 50, 150 and 298 K, the peaks near the solid surface are broader and span a distance of ~ 2.5 Å, which is the typical thickness of one monolayer. For 10 K and 50 K, there is a slight second layer feature, but not closely attaches with the first monolayer, which is deemed as the free water molecules for the two lower temperatures. At 10 K, we can observe the dominant sharp peaks take a distance of ~ 1.6 Å. Therefore, we can claim that the water molecules exhibit more ordered structures at lower temperatures as expected.
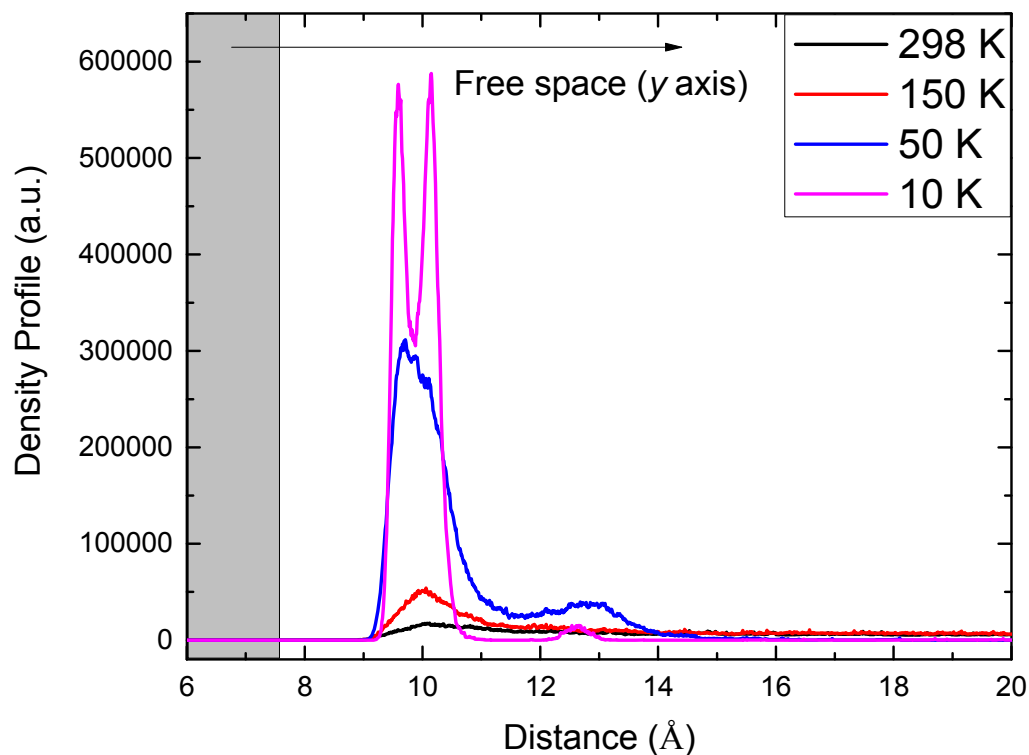
Fig. C7. Density profile of water molecules (using their center of mass) at four different temperatures. The shaded area indicate part of the solid slab. The center of the slab starts from zero on the *x* axis.

3.2 Mean square displacement

Mean square displacement (MSD) represents the average squared distance of the molecules over a period of time. Fig. C8 shows the MSD of Hw atoms at four temperatures over ~ 13.1 ps. We can observe the water molecules at lower temperatures (10 K and 50 K) have lower magnitude of MSD than at higher temperatures (150 K and 298 K) seen in the inset. And there is a steady decrease of the MSD with temperature decreasing. The curves show ballistic motion up to ~ 0.2 ps. While in the range of ~ 0.2 - ~ 0.3 ps, the cage motion can be observed.
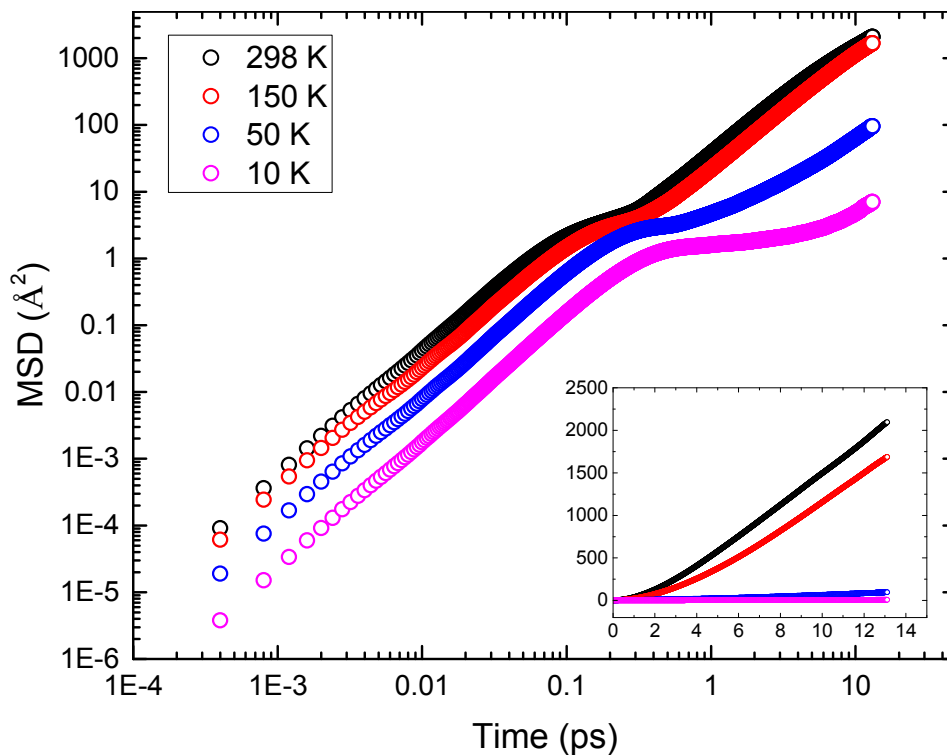
148

Fig. C8. MSD of Hw atoms at four temperatures on Fo(010) surface within ~ 13.1 ps. The inset shows the linear scales of the MSD and time.

3.3 S(Q,ω) spectra

Fig. C9 compares the S(Q,ω) of the four temperatures using the average results. Fig. C9a - d present the full range, librational mode, bending mode, and stretching mode, respectively. This allows us to observe the effects of temperature on the vibrational spectra. In Fig. C9b, we can observe the librational band is broad up to ~ 800 cm^{-1}, and the main feature is at ~ 100 cm^{-1}, and the features are left shifted with temperature decreasing. The specific peaks in the librational region indicate a well-defined adsorption sites.

149

The bending mode shown in Fig. C9c is only manifested for 10 K and 50 K at ~ 1526 cm^{-1}, but not for 150 K and 298 K. Thus, the bending feature might cover a wider range at higher temperatures as shown in Fig. C9c, unlike 10 K and 50 K. For the stretching mode shown in Fig. C9d, the frequencies are quite consistent with four temperatures, at ~ 3694 cm^{-1} and ~ 3765 cm^{-1}, attributed to the symmetrical and asymmetrical stretching modes of the Hw-Ow bonds.
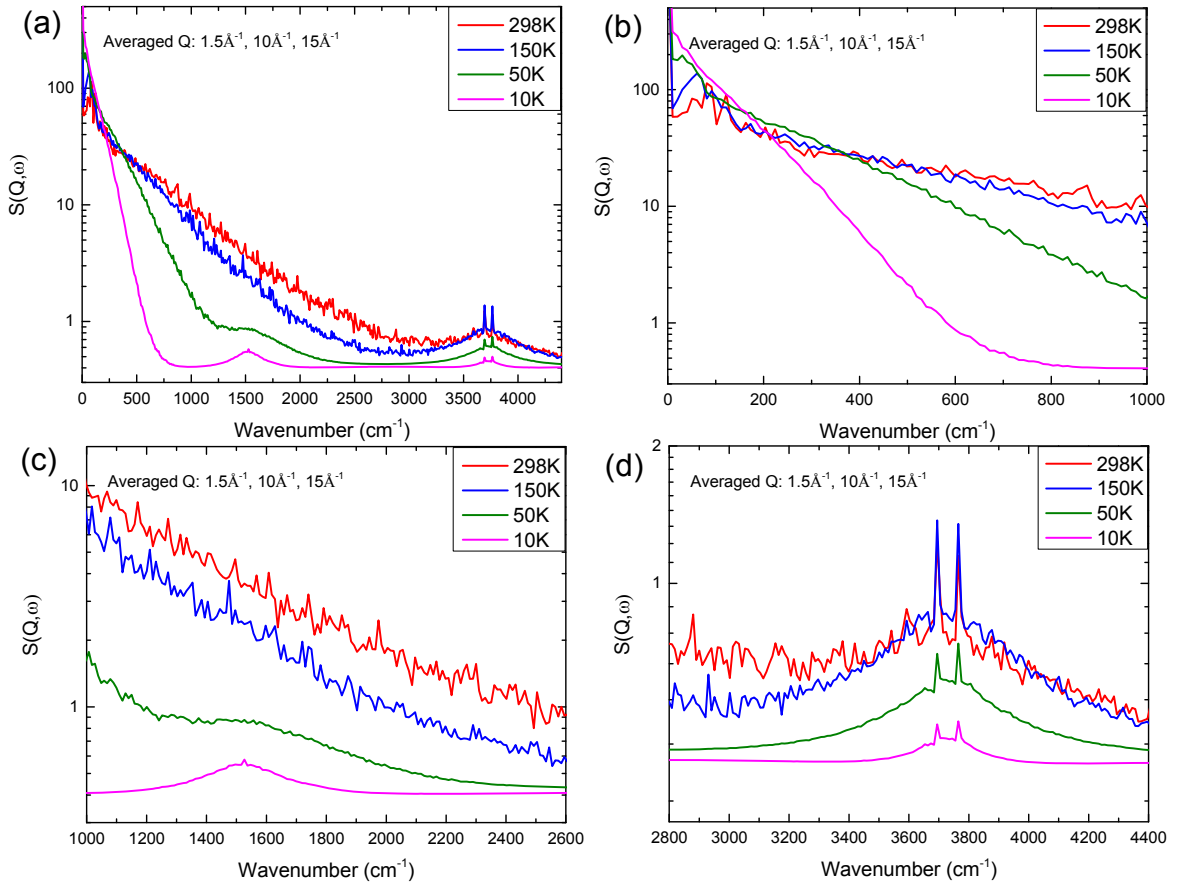

Fig. C9. Vibrational spectra shown by S(Q,ω) for water molecules on the Fo(010) surface at four different temperatures, an average result of three Q values. (a) full frequency range; (b), (c) and (d) are in different frequency ranges that represent different vibrational modes.

3.4 Power spectra

Power spectra was subsequently examined as support information for the spectra expressed using S(Q,ω). We examined the velocity autocorrelation functions (VACF) of the hydrogen atoms using the following equation,

$$C(t) = \frac{1}{N}\sum_{j=1}^{N}\left[v_j(0)\cdot v_j(t)\right]$$
Eqn (C1)

where the $v_j(t)$ and $v_j(0)$ are the final and initial velocities of one atom within one time step (0.2 fs in our study). Power spectra can be obtained by taking Fourier Transform (FT) onto the VACF using the following equation,

$$G(\omega) = \int_{-\infty}^{\infty} VACF\exp(-i\omega t)dt$$
Eqn (C2)

The obtained vibrational density of states (VDOS) plots using Hw atoms are displayed in Fig. C10.
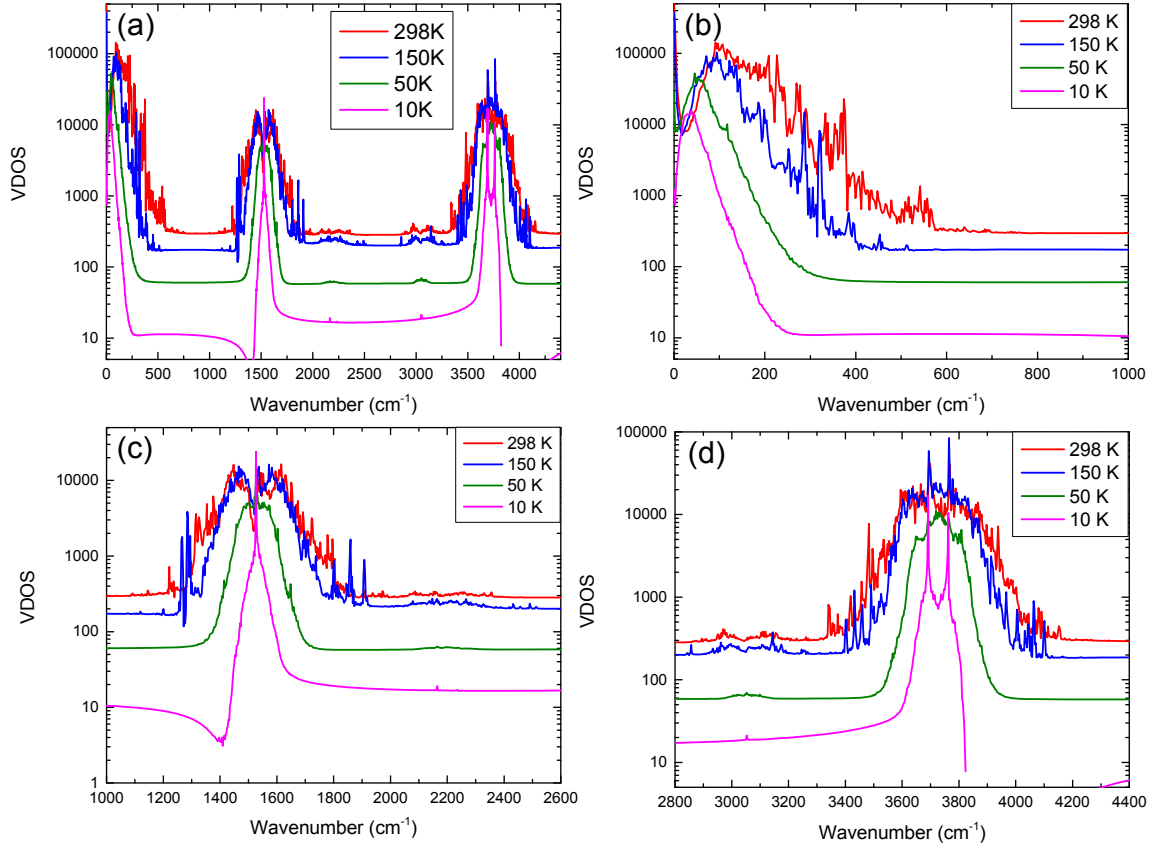
Fig. C10. Power spectra of water molecules on the Fo(010) surface at four different temperatures. (a) full spectra, (b), (c) and (d) are in different frequency ranges that represent different vibrational modes.

3.4.1 Librational mode

In Fig. C10b, there is a broad peak up to ~ 600 cm^{-1}; however, with temperature decreasing, there is a red shift for 50 K and 10 K with the sharp feature at ~ 100 cm^{-1}, the same as shown by S($\boldsymbol{Q}$,ω).

3.4.2 Bending mode

In Fig. C10c, we can observe the peaks become sharper with temperature decreasing. The center of the peaks is at ~ 1526 cm^{-1}, which is attributed to the bending

mode of the H-O-H bond. With temperature decreasing, the more ordered structure creates similar environment, thus the molecules show a more uniform bending mode. At higher temperatures (150 K and 298 K), we can observe a bi-mode feature. The bending mode frequency determined by power spectra is consistent with the result from $S(Q,\omega)$ (Fig. C9).

3.4.3 Stretching mode

In Fig. C10d, the splitting feature for stretching mode is consistent with that determined by $S(Q,\omega)$. The two splitting bands are at ~ 3691 cm^{-1} and ~ 3760 cm^{-1}, attributed to the asymmetrical and symmetrical stretching mode of the two Hw-Ow bonds. The molecules at lower temperature show sharper bands due to the similar bonding environment in an ordered structure.

3.5 EISF

The variation of the EISF values with Q provides the geometry information of the rotational motion, which is derived from the calculated rotational ISF (RISF). We plotted the EISF values vs Q in Fig. C11 for the four temperatures. For the isotropic rotational diffusion:

$$EISF = \left[\frac{\sin(r \cdot Q)}{r \cdot Q} \right]^2 \qquad \text{Eqn (C3)}$$

r is the radius of gyration of the molecule. The red curves are the fitted results using Eqn C3, all with $r = 1$ Å, which represents an ideal isotropic rotation situation. We can see at

50, 150, and 298 K, the ideal curve matches with the EISF data well, but there is deviation between the two sets of data at 10 K.
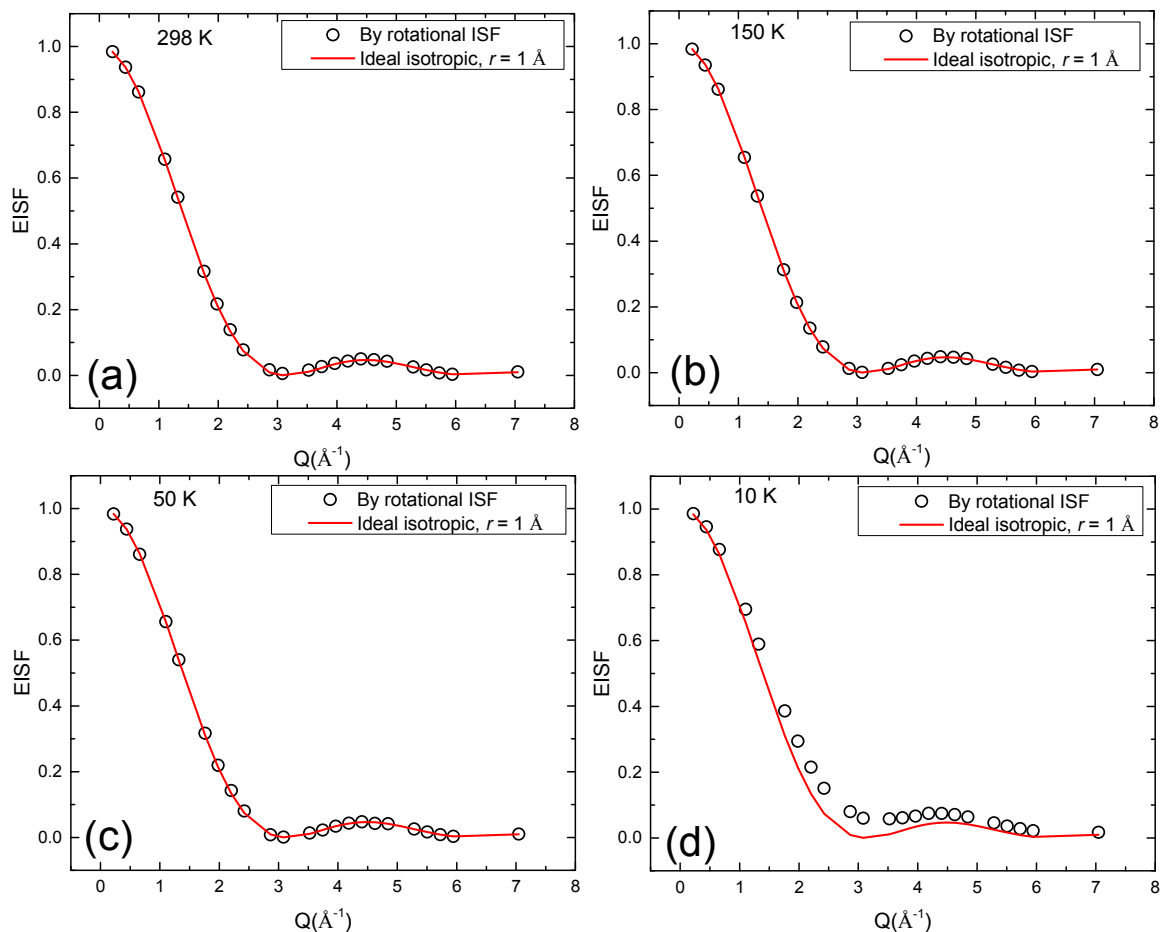

Fig. C11. EISF derived from rotational ISF as a function of Q values for (a) 298 K, (b) 150 K, (c) 50 K, and (d) 10 K, along with the ideal isotropic rotation curves (in red) with gyration radius r of 1 Å.

3.6 Residence Autocorrelation Function

The residence autocorrelation function is used to quantify the average time for which a typical water molecule remains close to the surface. This function calculates the average time of a molecule residing in certain regions, whose expression in a normalized form is

$$R_i(t) = \frac{\langle \theta_i(0) \cdot \theta_i(t) \rangle}{\langle \theta_i^2(0) \rangle}$$

Eqn (C4)

where θ_i is a Heaviside step function that takes the value of 1 if the molecules are in that region (i) at time t and all previous times; otherwise 0 if the molecules are outside the region. The $R_i(t)$ curves for four temperatures are shown in Fig. C11. The region of interest we define takes ~ 3 Å above the surface (distance of 9 ~ 12 Å shown in Fig. C6). We can see that the functions for 150 K and 298 K decay in a fast manner for up to ~ 40 ps and ~ 10 ps, respectively. However, the functions for 10 K and 50 K almost does not decay within ~ 52 ps. This suggests the stability of water close to the surface at different temperatures vary, i.e., higher temperature results in a faster mobility of water molecules.
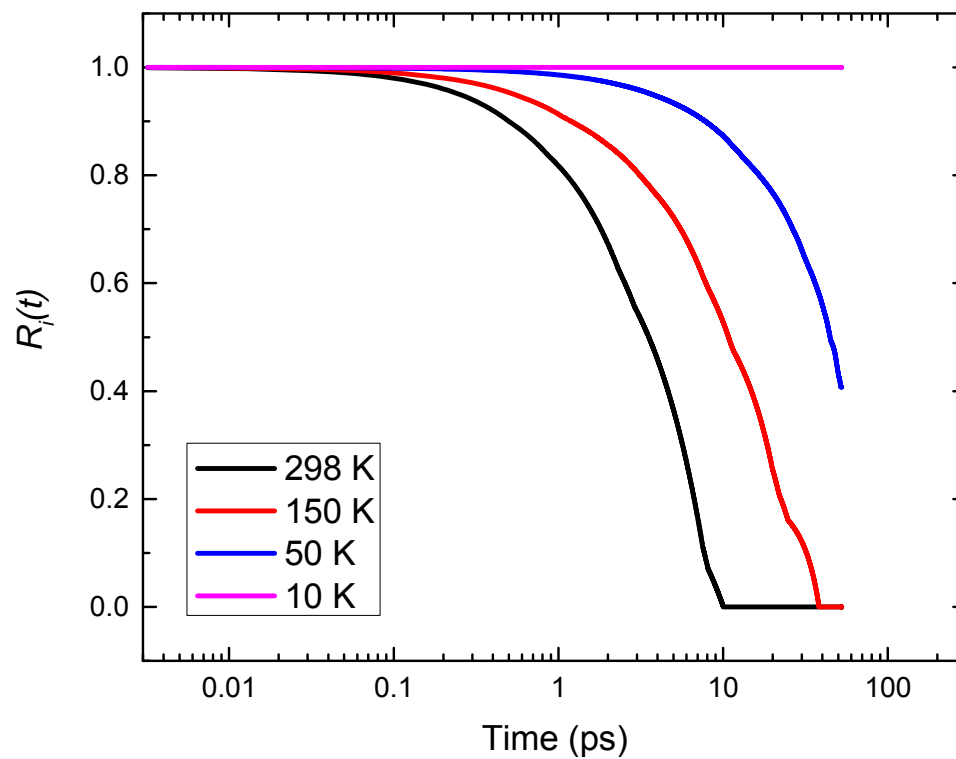
Fig. C12. Normalized residence autocorrelation function of water molecules on Fo(010) surface, and the trajectories of Ow atoms are used for analysis.